

Advanced Modelling of Free-Electron Lasers: Unaveraged  
Simulations, Sub-Wavelength Effects, and Superradiant

Pulses Saturation

PhD Thesis

Pornthep Pongchalee

Department of Physics

University of Strathclyde, Glasgow

January 14, 2025

This thesis is the result of the author's original research. It has been composed by the author and has not been previously submitted for examination which has led to the award of a degree.

The copyright of this thesis belongs to the author under the terms of the United Kingdom Copyright Acts as qualified by University of Strathclyde Regulation 3.50. Due acknowledgement must always be made of the use of any material contained in, or derived from, this thesis.

# Abstract

This thesis presents the development and application of advanced computer simulation techniques for the study of cavity-based Free-Electron Lasers (FELs). The research integrates the unaveraged 3D FEL simulation code Puffin with the Optical Propagation Code (OPC) to enable the modelling of broadband, high temporal-resolution cavity FELs. This novel approach allows for the translation of radiation field formats between Puffin and OPC, facilitating the simulation of a Regenerative Amplifier FEL operating in the VUV range.

Traditional simulation models for cavity-based FELs have averaged the optical field over an integer number of radiation wavelengths. This thesis, however, employs un-averaged simulation codes to model cavity-based FELs at the sub-wavelength scale. This enables the examination of effects such as Coherent Spontaneous Emission (CSE) from the electron beam and sub-wavelength cavity length detuning. The simulations reveal that for small sub-wavelength detunings, the FEL can preferentially lase at the third harmonic of the fundamental wavelength, suggesting new operational modes and potential applications for cavity-based FELs.

Additionally, a detailed study is conducted on the saturation mechanism of a single superradiant spike of radiation in an FEL. Using a one-dimensional model developed with Puffin, the thesis demonstrates the sub-wavelength evolution of spike radiation and electron dynamics, leading to a highly non-linear saturation process. The study provides insights into the broad spectrum and high power of the saturated spike, with a proposed saturation mechanism validated by numerical results and simplified analysis of the 1D FEL equations.

The combined use of Puffin and OPC codes represents a significant advancement

## Chapter 0. Abstract

in FEL simulation, enabling the exploration of unaveraged FEL and optical effects for the first time. This research not only enhances the understanding of fundamental FEL processes but also opens new avenues for further exploration and technological development in the field of Free-Electron Lasers.

# Acknowledgements

First of all, I would like to thank my supervisor, Brian McNeil, for his kindness and patience. Thanks for choosing me as your PhD student and introducing me to the world of Free-Electron Lasers. Your support in computational physics, coding, and simulation has been invaluable and made the experience truly exciting.

A big thank you to the Royal Thai Government for providing the funding that supported my PhD journey over the past four years.

To all my friends those I have met in Glasgow, thank you for turning the rainy and cloudy city into a place full of warmth and good times.

A special thanks to my parents and siblings for their unwavering support throughout this journey. And to Eve, thank you for always being by my side since we first met at the postgraduate induction. I cherish our time together and look forward to our future. I also want to express my gratitude to Eve's parents, Somdeach and Prapavadee Ruksomboon, for their warm welcome and providing a supportive environment during the toughest times of writing this thesis.

# Contents

<b>Abstract</b>	<b>ii</b>
<b>Acknowledgements</b>	<b>iv</b>
<b>List of Figures</b>	<b>vii</b>
<b>List of Tables</b>	<b>ix</b>
<b>1 Introduction</b>	<b>1</b>
1.1 A brief history of Free-electron laser and its application . . . . .	2
1.2 Different types of Free-Electron Lasers . . . . .	7
1.3 FEL simulation . . . . .	9
1.4 Thesis Outline . . . . .	11
<b>2 Basic Theory of Free-Electron Lasers</b>	<b>13</b>
2.1 Radiation Mechanisms of Moving Charges . . . . .	13
2.1.1 Classical Electrodynamics and Retarded Time . . . . .	13
2.1.2 Radiation from Electron Motion in a Dipole Oscillator . . . . .	15
2.1.3 Radiation from Electron Motion in Circular Paths . . . . .	17
2.1.4 Radiation from Electron Motion in an Undulator . . . . .	18
2.2 Fundamental Equations of FEL Dynamics . . . . .	22
2.2.1 Radiation Coherence in Free-Electron Lasers . . . . .	22
2.2.2 Radiation Wavelength Calculation . . . . .	24
2.2.3 Rate of Change of Electron Energy . . . . .	27
2.2.4 One-Dimensional FEL Equations . . . . .	31

## Contents

2.2.5	One-Dimensional Wave Equations . . . . .	34
2.2.6	Analysis of the One-Dimensional FEL Differential Equation . . .	38
2.2.7	Universal Scaling . . . . .	43
2.3	Basic Optics Theory for the Cavity-Based Free-Electron Laser . . . . .	47
2.3.1	Ray Transfer Matrix Analysis . . . . .	47
2.3.2	Two-mirror optical cavity stability . . . . .	50
2.3.3	Gaussian beam propagation . . . . .	53
<b>3</b>	<b>Unaveraged Models of a Cavity-Based Free-Electron Laser</b>	<b>57</b>
3.1	Introduction . . . . .	57
3.2	Field Format Conversion . . . . .	59
3.3	Simulation parameters . . . . .	60
3.4	Example simulation . . . . .	64
3.5	Conclusion . . . . .	68
<b>4</b>	<b>Investigating Sub-Wavelength Effects in a Free-Electron Laser Oscillator</b>	<b>70</b>
4.1	Introduction . . . . .	70
4.2	Simulation model . . . . .	72
4.2.1	FEL and optics code . . . . .	72
4.2.2	Simulation parameters . . . . .	73
4.3	Simulation results . . . . .	76
4.3.1	Empty cavity . . . . .	76
4.3.2	Gain lethargy . . . . .	77
4.3.3	Sub-wavelength cavity detuning . . . . .	79
4.3.4	Steady-state gain . . . . .	84
4.3.5	Third-harmonic generation . . . . .	86
4.4	Conclusion . . . . .	92
<b>5</b>	<b>Saturation of Superradiant Pulses in Free-Electron Lasers</b>	<b>94</b>
5.1	Introduction . . . . .	95
5.2	Simulation model . . . . .	96

## Contents

5.3	Simulation Example . . . . .	98
5.3.1	Simulation of Superradiant Pulses . . . . .	99
5.3.2	Pulse saturation . . . . .	105
5.3.3	Estimation of diffractive effects . . . . .	113
5.4	Conclusion . . . . .	117
<b>6</b>	<b>Conclusion and Future work</b>	<b>119</b>
<b>A</b>	<b>Pulse saturation scaling</b>	<b>124</b>
A.1	Pulse saturation scaling . . . . .	124
<b>B</b>	<b>Conference papers</b>	<b>126</b>
<b>C</b>	<b>Peer-review papers</b>	<b>127</b>
<b>D</b>	<b>Code snippets</b>	<b>128</b>
D.1	Puffin to OPC . . . . .	128
D.2	OPC to Puffin . . . . .	134
	<b>Bibliography</b>	<b>137</b>

# List of Figures

1.1	Undulator . . . . .	3
2.1	Retarded time . . . . .	14
2.2	Radiation from dipole oscillator . . . . .	16
2.3	Radiation from circular motion . . . . .	18
2.4	Undulator radiation . . . . .	19
2.5	Incoherent and Coherent Emission . . . . .	23
2.6	Resonant emission . . . . .	24
2.7	Energy exchange in resonant emission . . . . .	30
2.8	Electron bunching in resonant emission . . . . .	31
2.9	Schematic representation of Gaussian beam propagation. . . . .	55
2.10	Gaussian beam propagation in FEL cavity . . . . .	56
3.1	Puffin-OPC conversion diagram . . . . .	61
3.2	Example of RAFEL diagram . . . . .	65
3.3	RAFEL simulation flow chart . . . . .	66
3.4	Transverse FEL output intensity . . . . .	67
3.5	RAFEL energy output . . . . .	68
4.1	FEL oscillator example diagram . . . . .	75
4.2	Beam waist evolution in the optical cavity . . . . .	76
4.3	FEL oscillator power evolution . . . . .	78
4.4	Cavity detuning diagram . . . . .	80
4.5	Cavity detuning results . . . . .	82

List of Figures

4.6	Optical beam waist evolution in undulator . . . . .	83
4.7	Gain and efficiency plots . . . . .	85
4.8	FEL temporal profiles at different passes . . . . .	87
4.9	Fundamental and Third Harmonics power evolution 1 . . . . .	88
4.10	Fundamental and Third Harmonics power evolution 2 . . . . .	89
4.11	Temporal FEL profiles of the Gaussian beam case . . . . .	91
4.12	FEL power evolution of the Gaussian beam case . . . . .	92
5.1	Simulation window showing the method to re-initialise macroparticles. . .	97
5.2	Electron phase-space and radiation evolution about post-linear saturation, for the case of $4\pi\rho = 1$ . . . . .	100
5.3	Electron phase space and radiation evolution at $\bar{z} = 40$ and $\bar{z} = 100$ , for the case of $4\pi\rho = 1$ . . . . .	102
5.4	Electron phase-space and radiation evolution at $\bar{z} = 200$ and $\bar{z} = 400$ , for the case of $4\pi\rho = 1$ . . . . .	106
5.5	Electron phase-space and radiation evolution at $\bar{z} = 800$ and $\bar{z} = 1100$ , for the case of $4\pi\rho = 1$ . . . . .	107
5.6	The plot of FEL evolution includes scaled peak power, scaled energy, scaled spike energy, and the spike duration. . . . .	108
5.7	The saturated scaled peak power and scaled undulator length as a function of $4\pi\rho$ . . . . .	110
5.8	The saturated scaled energy of the pulse and its duration as a function of $4\pi\rho$ . . . . .	111
5.9	The saturated scaled energy of the spike and its width as a function of $4\pi\rho$ . . . . .	112
5.10	Comparison of 1D simulations with 3D approximation for $\bar{z} = 200$ and $\bar{z} = 750$ . . . . .	115
5.11	Comparison of 1D simulations with 3D approximation for $\bar{z} = 1200.5$ and $\bar{z} = 2156.5$ . . . . .	116

# List of Tables

3.1	Summary of RAFEL FEL parameters used in the simulations . . . . .	64
4.1	Summary of FEL oscillator parameters used in the simulations . . . . .	74

## List of Tables

# Chapter 1

## Introduction

In the first chapter of this thesis, a brief history of electromagnetic radiation sources is reviewed, starting from the first-generation light sources to the most current facilities being developed around the world, including the free-electron laser (FEL). This introduction chapter covers various aspects of utilising the FEL source and briefly discusses different types of FELs, providing a qualitative understanding of their principles of operation. In addition, the chapter introduces the briefly FEL studies from theoretical approaches to computer simulations.

The thesis outline is provided at the end of this chapter, followed by an overview of the basic FEL theory chapter and three main chapters that contribute to FEL knowledge through peer-reviewed publications.

Firstly, a method for performing unaveraged simulations of cavity-based FELs is presented. This chapter explains how to convert the radiation field format from the unaveraged FEL code Puffin to work in conjunction with the optics code OPC, including an example simulation.

Secondly, the unaveraged model is applied to investigate sub-wavelength effects in an FEL oscillator. The results suggest that by performing sub-wavelength cavity detuning, the third harmonic can be amplified with greater gain than the fundamental wavelength.

Finally, an extreme one-dimensional case is used to study the saturation mechanism of the superradiant spike in an FEL. The simulation results reveal interesting electron

behaviour as they pass through the sub-wavelength superradiant spike causing it to saturate.

## 1.1 A brief history of Free-electron laser and its application

Electromagnetic radiation such as radio waves, microwaves, infrared, visible light, ultraviolet, x-rays, and gamma rays can be generated by accelerating a charged particle [29]. This theory is behind the making of the various radiation sources around the world in many applications across the electromagnetic spectrum. The free-electron laser (FEL) is one such radiation light source, which is generated from freely accelerated electrons from the linear particle accelerator (Linac) at about the speed of light travelling within alternating dipole magnetic fields, known as an ‘undulator’ (see figure 1.1). As the electrons pass through the undulator, the magnetic field forces them to oscillate rapidly in alternating directions along the undulator axis. With each oscillation, the electrons release their energy as electromagnetic radiation. At present, there are no other radiation light sources that generate such ultra-bright coherent and short-pulse X-rays. A view on X-ray free-electron lasers (XFELs) have reviewed through its radiation principle and the typical status of the XFEL facilities around the world and also the discussion of the new XFEL sources that are being developed worldwide [40]. This section firstly reviews the historical background of the development of radiation light sources from the late 1950s to the upcoming future XFELs. It will outline three benefits of using XFELs and compare these benefits with the previous existing radiation light sources namely, synchrotron radiation, more specifically in terms of high energy, high brightness, and extremely short pulse duration light source that can be used in frontier biological science experiments. Finally, it will investigate example works which appear to support its use in molecular imaging biology applications.

Nowadays, there are four generations of radiation light sources that have been used since the 1950s. The first generation of radiation source [6] was a cyclic particle accelerator in which the charged particles were accelerated in a closed-loop path. The magnetic

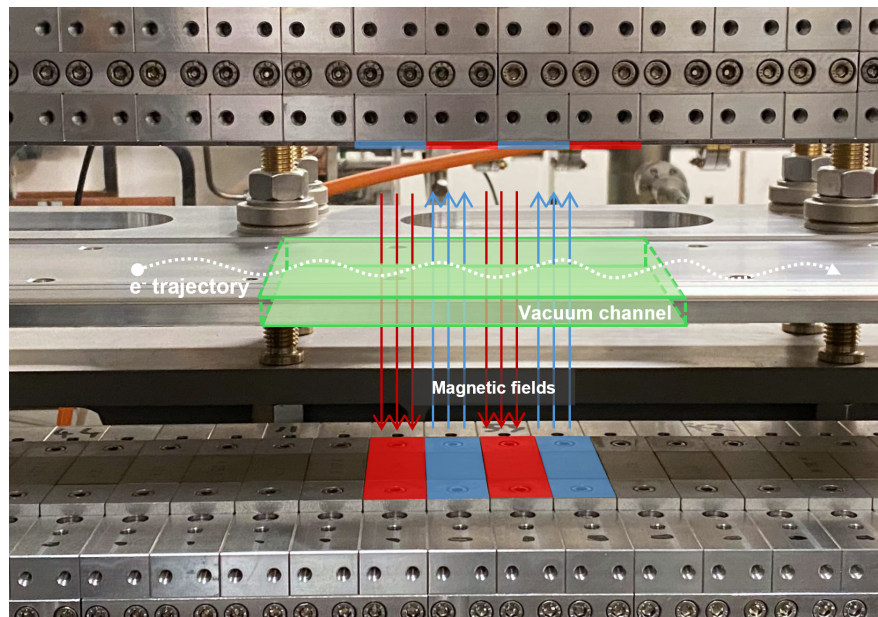


Figure 1.1: Photograph of a planar undulator from the FERMI light source at Elettra Sincrotrone, Trieste, taken by the author. The image includes a schematic overlay illustrating the periodic arrangement of alternating magnetic poles (red and blue) to depict the magnetic fields. The adjustable gap between the top and bottom plates defines the strength of the magnetic field, which is instrumental in tuning the wavelength of the emitted FEL radiation. As electrons travel through the vacuum channel, the magnetic fields induce an oscillatory motion, or ‘wobble,’ causing them to emit the FEL radiation.

field forces the particle beam into its closed path which increases with time during the accelerating process, being ‘synchronised’ to the increasing kinetic energy of the electrons – called synchrotron radiation (SR) [17]. That SR was operated parasitically on high energy particles accelerator. The first generation radiation sources slightly evolved toward the second-generation SR source [68], which can be defined from its used devices to control the propagation of electrons in the storage ring – a circular-shaped particle accelerator that was constructed to optimise its radiation from bending magnets. Then the electrons are forced to turn at every joint between two magnetic poles that electrons may lose their energy and emit the broadband electromagnetic spectrum, which covers the range of the electromagnetic spectrum from infrared to x-ray wavelength that are mostly interested in radiation in the x-ray regime. In an attempt to obtain more efficient energy and brightness of light, the new design and construction to optimise the synchrotron radiation from the insertion devices that may be used to upgrade the storage ring, which becomes the third-generation synchrotron radiation. Insertion devices, such as undulators and wigglers [50], which are long, periodic arrays of magnetic dipoles that force electrons to oscillate multiple times, resulting in the emission of more intense light. Many more of the third-generation synchrotrons have been and are being constructed around the world in countries on every continent as the national user facility to use in frontier scientific experiments. The main benefits of the development of radiation source facilities are the terms of obtaining high brightness and high energy that allow scientists to investigate in the cutting-edge fundamental research such as material science and structural biology. The competition in a new generation of radiation facilities development with enormously increased performance and efficiency has already started, despite the third-generation sources have shown their influence, which takes us beyond the present day to the fourth generation of radiation light sources. The competitor with the brand-new scientific case for a fourth-generation source is the hard x-ray, whose wavelength is less than  $1 \text{ \AA}$  (Angstrom) – a sub-nanometer (nm) scale e.g.  $1 \text{ \AA} = 0.1 \text{ nm}$ . XFELs, which are based on undulators installed in high-energy electron accelerators, are capable of producing fully coherent x-ray beams. While some XFELs require extensive setups spanning several kilometres, such as the European XFEL with

a total length of 3.4 km [77], others achieve similar results with more compact designs. For instance, the SPring-8 Angstrom Compact Free Electron Laser (SACLA) in Japan operates with a significantly shorter length of approximately 700 m [74].

The three benefits of using fourth-generation technology are listed as XFEL devices, which have a peak brightness far exceeding that of third-generation synchrotrons, achieved through significantly higher orders of light intensity. In contrast to SRs, the main advantage of XFELs is their exceptionally high-brightness x-ray source, which is billions of times brighter than third-generation SRs. XFELs produce x-ray photon beams from undulators that allow observation of atomic-scale structures. For example, using x-ray diffraction techniques, XFELs can now deliver highly intense x-rays to a sample with a sufficient number of diffraction photons. Calculations demonstrate that XFEL beams can be perfectly focused onto single molecular samples [47, 71]. These studies support the claim that high-energy, high-brightness x-ray FELs are promising tools for imaging at the atomic scale. Another advantage is their high energy, related to the shorter wavelength of x-rays with full coherence, which can achieve high-resolution x-ray imaging at the interatomic scale [18]. Compared to SRs, XFELs can resolve complex structures with a resolution of 3.5 Å, as shown in XFEL-processed data, outperforming synchrotron datasets that achieve only 4.1 Å resolution [37]. The shorter wavelength (higher energy) x-rays produced by XFELs are microscopic at the sub-nanometer scale. A review by [7] highlights the potential of XFELs for imaging single-molecule structures, supported by simulations and theory. Another advantage of XFELs is their extremely short pulse duration, often as brief as 100 fs or less—timescales unattainable by SRs. This makes XFELs particularly useful for time-resolved experiments to investigate ultrafast biochemical reactions [35]. Research and development of XFEL technology are underway at many research facilities worldwide. Starting with the world’s first XFEL in the United States, the ”Linac Coherent Light Source (LCLS)” was developed as a collaborative, multi-institutional project. It utilizes 14-GeV electrons from the Stanford Linear Accelerator Center (SLAC) Linac as the source for a 1.2-Å FEL [25]. Following the success of LCLS, the European XFEL—a collaboration among several European countries—was constructed in Hamburg, Germany. The

3.4-km-long facility uses a superconducting Linac to produce 17.5-GeV electrons with a wavelength of 1.0-Å [3]. XFELs, such as the LCLS and European XFEL, provide scientists with access to higher photon energies than previously available sources.

In 2014, the investigation of XFELs applications in biological imaging at the LCLS, SLAC National Accelerator Laboratory in Stanford, USA has focused on developing a technique called single particle imaging (SPI) [4]. The LCLS system used for the atomic-scale imaging of biological structures, the resolution of the imaging range of the system needs to be maximised, which has been carried out successfully to produce the X-ray diffraction images of viruses [71], bacteriophages [33], organelles [28], and cyanobacteria [75]. Eventually, the resolution of XFEL will be either limited by the operating wavelength of the XFEL or the optical structure properties of the samples. The resolution of the light beam is related to the used wavelength. The results suggest that XFELs operating at shorter wavelengths achieve a better atomic-scale resolution when imaging biological samples. Furthermore, XFEL can be used to identify the structure of small biological molecules that are difficult to study with conventional X-ray sources. One example is to study the structure of BinAB [20], which is obtained from bacteria and is toxic to mosquitoes. Understanding the structure of BinAB can help to develop the drug for the treatment of mosquito-borne diseases such as malaria, dengue fever, and Zika fever. Moreover, the advantage of XFELs in terms of ultra-fast laser pulses can be used to study the water-splitting process, which is one step in the photosynthesis process since it can capture real-time imaging of all processes in a short period of time when the reaction occurs suddenly [78]. Understanding the water-splitting process might help develop techniques to create artificial photosynthesis, which can be used to produce solar fuel and renewable energy.

In conclusion, XFEL has been reported to analyse a new approach to study biological samples, operating at a short wavelength region that achieves its goal to determine biological structures at atomic resolution. In addition, XFEL facilities are beginning to operate and have a major impact on scientific investigations. The applications of XFEL will be expanded and may provide important insight into many of the questions encountered in structural biology. XFEL would make the frontier technology easily ac-

cessible to other researchers in the field of biological structure research, single-particle imaging, diffraction imaging of viruses, and other related applications.

## 1.2 Different types of Free-Electron Lasers

FELs can be categorised into several types on the basis of their operational principles and configurations. These include Oscillator FELs, Self-Amplified Spontaneous Emission (SASE) FELs, Regenerative Amplifier FELs (RAFELs), and High-Gain Harmonic Generation (HG) FELs. Each type has unique characteristics and applications, which are discussed in detail below.

### FEL Oscillator

FEL oscillator is one of the earliest and simplest configurations of FELs. In an FEL oscillator, the electron beam passes through an undulator located within an optical cavity typically formed by two mirrors. The radiation emitted by the electron beam as it propagates through the undulator is reflected back and forth between the cavity mirrors, repetitively interacting with subsequent electron beams. This feedback mechanism allows radiation to build up coherently over many passes, leading to coherent lasing [22].

FEL oscillators operate effectively at lower frequencies, typically in the infrared to visible spectrum, and are characterized by their ability to produce radiation in continuous-wave (CW) or long-pulse modes, depending on the time scale under investigation [73]. They provide a stable, short-pulse, narrow-bandwidth radiation source with high spectral purity, making them particularly useful for applications requiring precise and stable light, such as spectroscopy and precision measurement. For example, FEL oscillators are used in studying molecular vibrations and rotations, allowing scientists to probe the fundamental properties of materials and molecules with great accuracy [46].

## **Self-Amplified Spontaneous Emission (SASE) FELs**

SASE FELs are a type of free-electron laser capable of generating high-brightness, short-wavelength radiation, including X-rays. Unlike Oscillator FELs, SASE FELs do not rely on an optical cavity. Instead, they utilize a single pass of the electron beam through a long undulator to achieve lasing.

In a SASE FEL, the electron beam begins to emit spontaneous radiation upon entering the undulator. This initial radiation interacts with the electron beam, causing microbunching of electrons at the scale of the radiation wavelength. This microbunching amplifies the emission process, resulting in the exponential growth of radiation intensity along the undulator. The output is a highly coherent and intense beam of light with extremely high brightness [45].

SASE FELs are particularly well-suited for producing ultra-short, high-intensity pulses and are widely employed in scientific research facilities. For example, the Linac Coherent Light Source (LCLS) at the SLAC National Accelerator Laboratory in the United States and the European XFEL in Germany are two prominent facilities [23, 25]. These sources enable researchers to perform time-resolved studies of atomic and molecular processes, offering valuable insights into chemical reactions, phase transitions, and other ultrafast phenomena occurring on femtosecond timescales [66].

## **Regenerative Amplifier FELs (RAFELs)**

RAFELs combine features of both Oscillator and SASE FELs. In a RAFEL, the electron beam passes through an undulator within an optical cavity, similar to an Oscillator FEL. However, unlike traditional oscillators, RAFELs operate in a high-gain regime with lower reflectivity mirrors, which allows for the amplification of radiation over fewer passes [48, 49].

The high-gain operation of RAFELs enables them to achieve lasing with fewer cavity round-trips [24], making them suitable for applications requiring rapid build-up of radiation intensity. This configuration allows RAFELs to produce coherent radiation at shorter wavelengths compared to conventional oscillator FELs, making them useful for various scientific and industrial applications. For example, RAFELs can be used in

advanced materials research, medical imaging, and the study of dynamic processes in matter [72].

### **High-Gain Harmonic Generation (HGHG) FELs**

HGHG FELs utilise a two-stage process to generate high-brightness, short-wavelength radiation. In the first stage, a seed laser (typically a conventional laser) is used to modulate the energy of the electron beam as it passes through a modulator undulator. This modulation creates a periodic energy structure in the electron beam.

In the second stage, the modulated electron beam passes through a radiator undulator tuned to a harmonic of the seed laser wavelength. The microbunched electron beam emits coherent radiation at this harmonic wavelength, resulting in high-brightness, short-wavelength output.

HGHG FELs are advantageous for producing stable, narrow-bandwidth radiation with high temporal coherence. They are particularly useful for applications requiring precise control over the radiation wavelength and phase, such as in spectroscopy and imaging. For instance, HGHG FELs enable high-resolution studies of chemical dynamics and biological processes, providing detailed information about the structure and behaviour of complex molecules [2, 79].

## **1.3 FEL simulation**

The study of FELs can be divided into three main approaches, including theoretical analysis, experimental investigations, and computational simulations. Each approach offers unique insights into the complex processes that govern the operation of FEL. Theoretical studies provide the fundamental principles and mathematical frameworks necessary to understand the underlying physics of FELs. Experimental investigations validate these theories and explore the practical aspects of FEL performance and optimisation. The scientists working in this field are focused on the hardware and devices to help improve the quality of the light source to match the user requirements, enabling the new techniques for experiment. However, due to the complex nature of FEL inter-

actions and the challenges of experimental measurements, computational simulations have become an essential tool in FEL research. FEL simulations enable researchers to model and predict the behaviour of electron beams and the emitted radiation with high precision, offering a detailed understanding that complements theoretical and experimental approaches.

FEL simulations are based on the interaction between a relativistic electron beam and a periodic magnetic field, typically provided by an undulator or wiggler. As the electrons traverse the undulator, they experience a sinusoidal magnetic field that forces them into an oscillatory motion. This motion causes the electrons to emit synchrotron radiation, which can become coherent under the right conditions.

The primary equations governing FEL simulations include the Lorentz force equation for the electron motion and Maxwell's equations for the electromagnetic fields. The FEL interaction can be described by the coupled Maxwell-Lorentz equations, which account for the self-consistent evolution of the electron beam and the radiation field.

Several computational tools have been developed to simulate FELs with high precision. These tools vary in their complexity and the specific aspects of the FEL process they model. Key simulation codes used in FEL research include the following:

- **GENESIS:** A widely-used 3D time-dependent simulation code that models the interaction between the electron beam and the radiation field in an FEL. It solves the coupled Maxwell-Lorentz equations and can simulate various FEL configurations, including SASE and HGHG FELs [67].
- **Ginger:** A code that provides both time-dependent and steady-state simulations of FELs. Ginger [26] is capable of modelling the detailed dynamics of the electron beam and the radiation field, making it suitable for studying the gain process and saturation effects in FELs.
- **Puffin:** An advanced 3D FEL simulation code that does not rely on the slowly varying envelope approximation (SVEA). Puffin can model the full temporal and spatial structure of the radiation field, providing more accurate simulations of the interaction between the electron beam and the radiation [14, 16].

- **OPC:** The Optical Propagation Code (OPC) is used to simulate the propagation of the radiation field within the optical cavity of an FEL oscillator [32, 76]. OPC can be coupled with other FEL codes like Puffin to model the complete FEL oscillator system. The process of the translation between Puffin and OPC codes will be discussed in Chapter 3.

Simulation plays an important role in the design and optimisation of FELs. By modelling the behaviour of the electron beam and the lasing cavity, scientists can predict the performance of different FEL configuration, and make adjustments to improve the output power, beam quality, and other parameters. This allows researchers to explore new designs and operating regimes that would be difficult or impossible to achieve experimentally.

Additionally, the use of simulation can help to reduce the cost and complexity of FEL experiments by allowing scientists to test different configurations virtually before building and testing them in the lab. This allows researchers to focus their experimental efforts on the most promising designs and avoid costly mistakes.

FEL simulations are a powerful tool for understanding and optimising the performance of free-electron lasers. Using advanced simulation codes and techniques, researchers can gain detailed insight into the complex interactions between the electron beam and the radiation field. These simulations play a crucial role in the development of next-generation FELs, enabling the exploration of new operational regimes and the design of more efficient and versatile light sources.

## 1.4 Thesis Outline

This thesis aims to provide a thorough understanding of the essential tools and methodologies required to simulate the principles of Free-Electron Laser (FEL) science. It incorporates detailed visual aids to facilitate comprehension of the complex physical interactions that occur during the FEL process. The thesis is structured into six chapters, each addressing a key aspect of FEL theory, simulation, and application.

**Chapter 2** revisits the fundamental theory of FELs, starting with an explanation

## Chapter 1. Introduction

of radiation produced by accelerating charged particles, as described by the Liénard-Wiechert potentials. It provides examples of radiation patterns from three types of electron motion: simple harmonic, circular, and wiggler/undulator. Following this, the chapter delves into the basic theory of FELs, including the fundamental equations governing the FEL mechanism. Additionally, the basic optical theory relevant to cavity-based FELs is discussed, covering principles of Ray Transfer Matrix, stability conditions for optical cavities, and Gaussian beam propagation.

**Chapter 3** details a method for translating between two simulation codes, Puffin and OPC, enabling the modeling of the FEL within a cavity-based framework. This chapter focuses on the integration and compatibility between these codes to ensure accurate simulations.

**Chapter 4** explores sub-wavelength effects by adjusting the optical cavity length in an FEL oscillator to produce third harmonic radiation. The chapter examines how these adjustments influence the generation and amplification of harmonics.

**Chapter 5** examines the saturation of high-power superradiant spikes, an important aspect of the FEL amplification process. This chapter delves into the dynamics of superradiant pulse saturation and its impact on FEL performance.

**Chapter 6** provides a summary of the thesis, reflecting on the findings and considering potential directions for future research. It consolidates the insights gained from the simulations and experiments conducted throughout the study.

**Appendix** includes a list of publications that have contributed to this thesis and presents useful snippets of code. The appendix serves as a resource for readers interested in further details and practical applications related to the thesis.

## Chapter 2

# Basic Theory of Free-Electron Lasers

### 2.1 Radiation Mechanisms of Moving Charges

The radiation emitted by an electron in motion is a fundamental concept in understanding the behaviour of FELs. This section explores the classical electrodynamics principles governing this radiation, including the concepts of retarded time and Liénard-Wiechert potentials. It also examines radiation from different electron motions: dipole oscillators, circular motion, and undulators. Theoretical results are complemented by visualisations of radiation patterns.

#### 2.1.1 Classical Electrodynamics and Retarded Time

In classical electrodynamics, the electromagnetic fields produced by a moving charge are determined by the charge's position and velocity at an earlier time, known as the retarded time. The concept of retarded time is essential for understanding how information about the electron's motion propagates through space.

For an electron at position  $\mathbf{r}_0(t)$  at time  $t$ , the fields at a point  $P$  in the location  $\mathbf{r}(t)$  are not determined by the instantaneous position  $S$  located at  $\mathbf{r}_0(t)$  and velocity of the charge. Instead, they are influenced by the earlier electron's position  $S'$  at the retarded time  $t'$ , defined by:

$$t' = t - \frac{|\mathbf{r}(t) - \mathbf{r}_0(t')|}{c} \quad (2.1)$$

Here,  $c$  is the speed of light, and  $|\mathbf{r}(t) - \mathbf{r}_0(t')|$  is the distance between the observation point and the electron at the retarded time. The retarded time accounts for the finite speed at which electromagnetic interactions propagate. It represents the time it takes for the effects of the electron's motion to travel outward at the speed of light, covering the distance  $|\mathbf{r}(t) - \mathbf{r}_0(t')|$  before arriving at point  $P$ . Therefore, when calculating the electromagnetic fields produced by a moving charge at a specific location, one must consider the state of the charge at the retarded time, rather than its state at the present moment. This approach ensures that the effects of the charge's motion are consistent with the causality principle and the finite propagation speed of electromagnetic interactions. The concept of retarded position and time is illustrated in Figure 2.1.

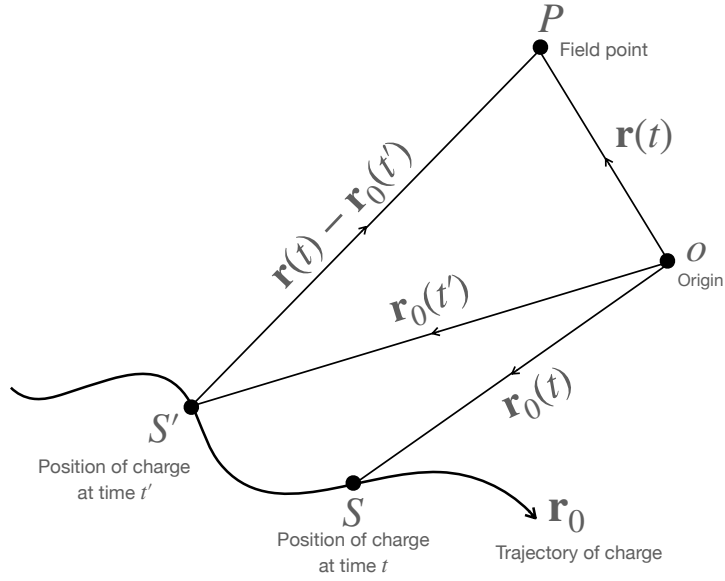


Figure 2.1: Illustration of the concept of retarded time for a moving charge. The trajectory of the charge is shown, with positions at the current time  $t$  and the retarded time  $t'$ . The point  $P$  represents the field point where the electromagnetic fields are being calculated. The distance  $|\mathbf{r}(t) - \mathbf{r}_0(t')|$  between the field point and the charge at the retarded time accounts for the time delay due to the finite speed of light, ensuring consistency with the causality principle and the finite propagation speed of electromagnetic interactions.

To accurately describe the electromagnetic fields produced by a moving charge, the Liénard-Wiechert potentials provide a precise solution to Maxwell's equations for the electric and magnetic potentials due to a moving point charge. The electric field  $\mathbf{E}$  generated by a moving point charge, observed at the position  $\mathbf{r}$  and time  $t$ , can be described as:

$$\mathbf{E}(\mathbf{r}, t) = \frac{q}{4\pi\epsilon_0} \left[ \frac{1}{R^2} \frac{(\hat{\mathbf{n}} - \boldsymbol{\beta})(1 - \beta^2)}{(1 - \hat{\mathbf{n}} \cdot \boldsymbol{\beta})^3} + \frac{1}{cR} \frac{\hat{\mathbf{n}} \times (\hat{\mathbf{n}} - \boldsymbol{\beta}) \times \dot{\boldsymbol{\beta}}}{(1 - \hat{\mathbf{n}} \cdot \boldsymbol{\beta})^3} \right]_{t_r}, \quad (2.2)$$

where the vector in the bracket  $[...]_{t_r}$  is evaluated at the retarded time  $t' = t - R(t')/c$ . Here,  $q$  is the charge of the particle,  $\epsilon_0$  is the permittivity of free space,  $\hat{\mathbf{n}}$  is the unit vector from the charge to the observation point,  $\boldsymbol{\beta} = \mathbf{v}/c$  is the normalised velocity of the charge,  $\dot{\boldsymbol{\beta}} = d\boldsymbol{\beta}/dt$  is the acceleration, and  $R = |\mathbf{r} - \mathbf{r}_0(t')|$  is the distance from the charge to the observation point.

The first term represents the velocity field, which falls off as  $1/R^2$ , and is a relativistic generalisation of Coulomb's law. The second term represents the radiation field, which falls off as  $1/R$ , and describes the electromagnetic waves emitted by the accelerating charge. This distinction between the velocity field and the radiation field highlights the different behaviours and influences of moving and accelerating charges.

### 2.1.2 Radiation from Electron Motion in a Dipole Oscillator

Consider an electron undergoing simple harmonic motion along the  $x$ -axis. This motion can be described by the position function:

$$\mathbf{r}_0(t) = x_0 \sin\left(\frac{\bar{\beta}ct}{x_0}\right) \hat{\mathbf{x}}, \quad (2.3)$$

where  $x_0$  is the amplitude of oscillation,  $\bar{\beta} = \frac{x_0\omega}{c}$  is the normalised relativistic electron velocity, and  $\omega$  is the angular frequency. The corresponding velocity and acceleration in the relativistic limits are given by:

$$\boldsymbol{\beta}(t) = \bar{\beta} \cos\left(\frac{\bar{\beta}ct}{x_0}\right) \hat{\mathbf{x}}, \quad (2.4)$$

$$\dot{\boldsymbol{\beta}}(t) = -\frac{\bar{\beta}^2 c}{x_0} \sin\left(\frac{\bar{\beta} c t}{x_0}\right) \hat{\mathbf{x}}. \quad (2.5)$$

Here,  $\boldsymbol{\beta}(t) = \frac{\mathbf{v}(t)}{c}$  represents the dimensionless velocity of the electron, and  $\dot{\boldsymbol{\beta}}(t) = \frac{d\boldsymbol{\beta}(t)}{dt}$  is the dimensionless acceleration.

This simple harmonic motion represents the simplest form of oscillation that generates electromagnetic radiation and is also the easiest to visualise using the Liénard-Wiechert potentials. The simulation result of the radiation field evolving from this behaviour is shown in Figure 2.2.

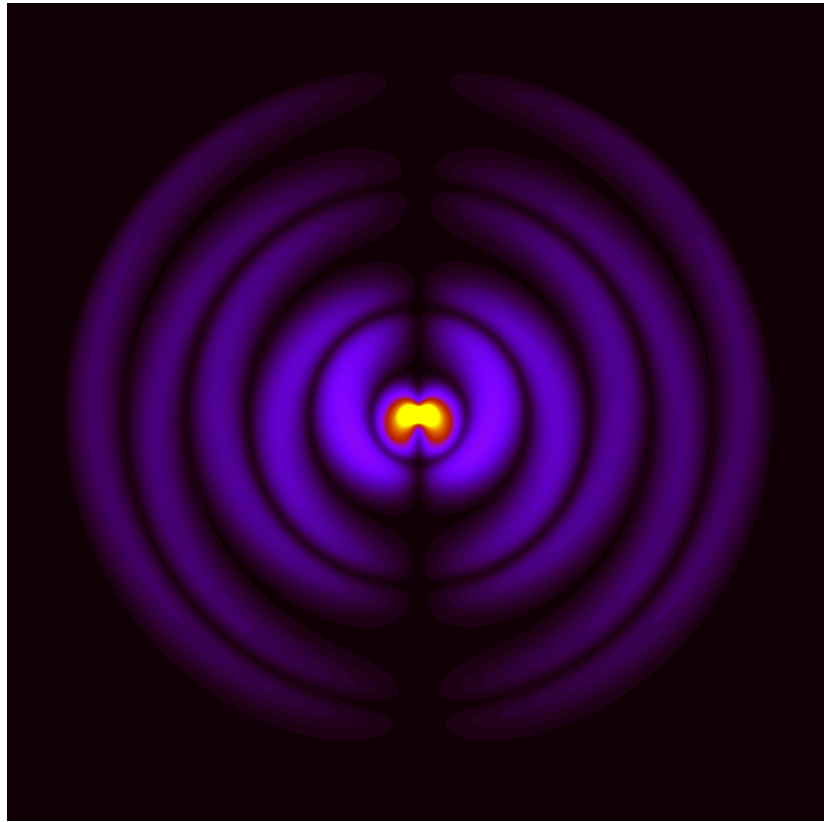


Figure 2.2: Simulation result illustrating the radiation field emitted from the simple harmonic motion of an electron in a dipole oscillator. The concentric wavefronts represent the radiated electromagnetic waves propagating outward from the electron. The colour intensity indicates the strength of the radiation field, with warmer colours (yellow and red) showing higher field intensities. The symmetric pattern reflects the dipole nature of the radiation, with the highest intensity emitted perpendicular to the direction of oscillation.

### 2.1.3 Radiation from Electron Motion in Circular Paths

Electrons moving in a circular trajectory, such as those in a synchrotron, emit radiation because of their continuous centripetal acceleration. The Lorentz force, resulting from the magnetic field, provides the necessary centripetal force for this circular motion. The details of the Lorentz force will be discussed later in Section 2.1.4. In this section, the simple circular path is considered to demonstrate the radiation field emitted from synchrotron-like motion.

The electron's motion in a circular trajectory can be described within a two-dimensional  $xz$ -plane, constrained by relativistic conditions. Assume that the electron has a normalised velocity  $\bar{\beta} = \bar{v}/c$ , where  $\bar{\beta} = \sqrt{1 - 1/\gamma^2}$ , and  $\gamma$  is the relativistic Lorentz factor related to the electron's energy  $E = \gamma m_e c^2$ , with  $m_e$  being its rest mass.

The position of the electron in a circular path is given by:

$$\mathbf{r}_0(t) = R \cos\left(\frac{\bar{\beta}ct}{R}\right) \hat{\mathbf{x}} + R \sin\left(\frac{\bar{\beta}ct}{R}\right) \hat{\mathbf{z}}, \quad (2.6)$$

where  $R$  is the radius of the circular trajectory.

Differentiating the position vector with respect to time  $t$  gives the velocity:

$$\mathbf{v}(t) = -\bar{\beta}c \sin\left(\frac{\bar{\beta}ct}{R}\right) \hat{\mathbf{x}} + \bar{\beta}c \cos\left(\frac{\bar{\beta}ct}{R}\right) \hat{\mathbf{z}}. \quad (2.7)$$

The magnitude of the velocity is  $v(t) = \bar{\beta}c$ . Dividing the equation by  $c$  gives the normalised velocity vector as:

$$\boldsymbol{\beta}(t) = -\bar{\beta} \sin\left(\frac{\bar{\beta}ct}{R}\right) \hat{\mathbf{x}} + \bar{\beta} \cos\left(\frac{\bar{\beta}ct}{R}\right) \hat{\mathbf{z}}. \quad (2.8)$$

Differentiating the velocity vector with respect to time  $t$  gives the acceleration:

$$\dot{\boldsymbol{\beta}}(t) = -\bar{\beta}^2 \frac{c}{R} \cos\left(\frac{\bar{\beta}ct}{R}\right) \hat{\mathbf{x}} - \bar{\beta}^2 \frac{c}{R} \sin\left(\frac{\bar{\beta}ct}{R}\right) \hat{\mathbf{z}}. \quad (2.9)$$

The magnitude of the acceleration is  $a(t) = \bar{\beta}^2 \frac{c^2}{R} = \frac{v^2(t)}{R}$ , which is centripetal and is directed towards the centre of the circular path.

This circular motion of electrons is significant in generating synchrotron radiation,

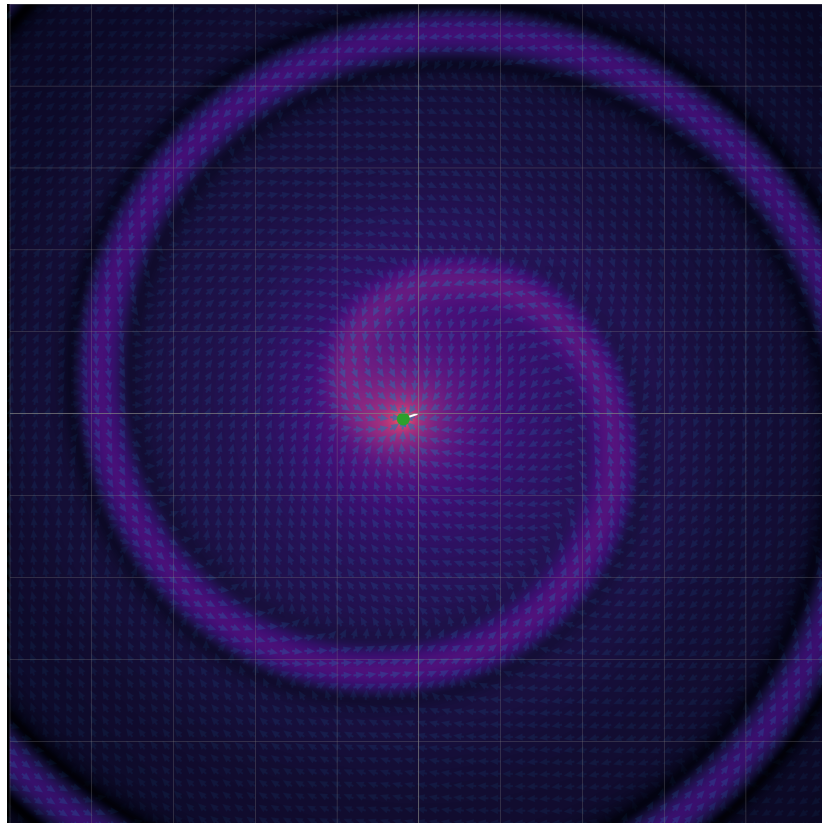


Figure 2.3: Simulation result illustrating the radiation field emitted from the circular motion of an electron in a synchrotron-like setup. The spiral pattern indicates the trajectory of the electron, and the emitted radiation is visualised as the surrounding wavefronts. The colour intensity represents the strength of the radiation field, with brighter regions indicating higher field intensities. The arrows depict the direction and relative magnitude of the radiation field vectors.

a key mechanism in many advanced radiation sources. The emitted radiation can be effectively visualised using the Liénard-Wiechert potentials, which account for the relativistic effects involved. The simulation result illustrating the radiation field from this behaviour is shown in Figure 2.3.

#### 2.1.4 Radiation from Electron Motion in an Undulator

A wiggler or undulator consists of a periodic arrangement of magnets that force the electron to oscillate transversely to its motion. This periodic motion leads to the emission of radiation at specific wavelengths, determined by the period of the magnetic structure and the energy of the electron.

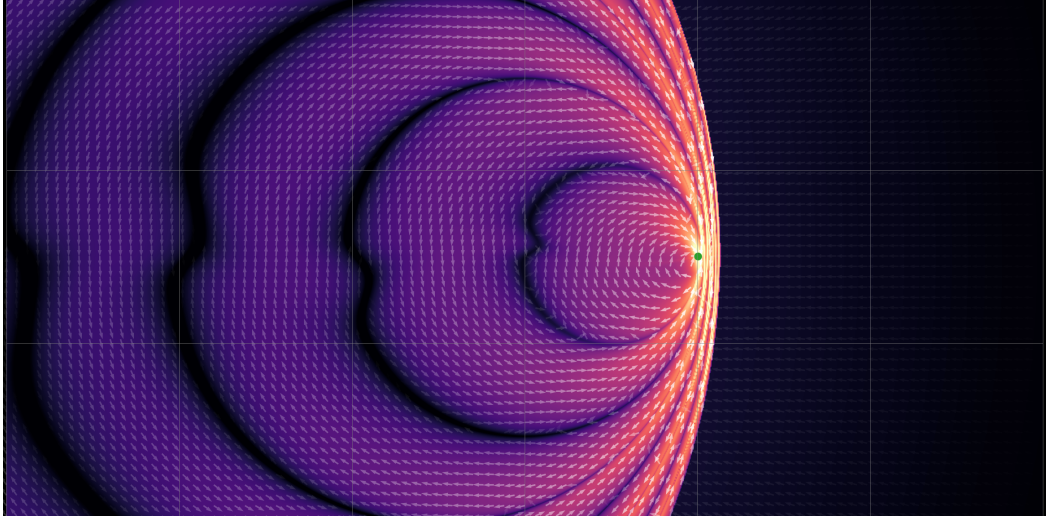


Figure 2.4: The radiation pattern from the accelerating electron in the undulator at the 4th magnetic period. The green dot shows the electron position. The white arrows represent the electric field vectors.

Assuming the electron propagates along the positive  $z$ -axis and the magnetic field from the periodic magnetic lattice points in the negative  $y$ -axis, the magnetic field of the planar undulator can be described as follows:

$$\mathbf{B}_w = -B_0 \sin\left(\frac{2\pi z}{\lambda_w}\right) \hat{\mathbf{y}}, \quad (2.10)$$

and in the case of a helical undulator:

$$\mathbf{B}_w = B_0 \left( \cos\left(\frac{2\pi z}{\lambda_w}\right) \hat{\mathbf{x}} - \sin\left(\frac{2\pi z}{\lambda_w}\right) \hat{\mathbf{y}} \right), \quad (2.11)$$

where  $B_0$  is the peak magnetic field of the undulator, and  $\lambda_w$  is the period of the undulator.

The Lorentz force describes the force experienced by a charged particle moving through electric and magnetic fields. For a charged particle with charge  $q$  moving with velocity  $\mathbf{v}$  in the presence of an electric field vector  $\mathbf{E}$  and a magnetic field flux density  $\mathbf{B}$ , the Lorentz force  $\mathbf{F}$  is given by:

$$\mathbf{F} = \frac{d\mathbf{p}}{dt} = q(\mathbf{E} + \mathbf{v} \times \mathbf{B}), \quad (2.12)$$

where  $\mathbf{p} = \gamma m_e \mathbf{v}$  is the momentum. Considering that the magnetic field of the undulator is dominant with a relatively weak radiation field before FEL amplification ( $E \sim 0$ ), and assuming  $\mathbf{v} = v_z \hat{z}$ , the electron motion due to the Lorentz force results from the cross product. The vector component in the  $x$ -direction gives:

$$\gamma m_e \frac{dv_x}{dt} = -e \frac{dz}{dt} B_0 \sin\left(\frac{2\pi z}{\lambda_w}\right), \quad (2.13)$$

for  $0 \leq z \leq N_w \lambda_w$ . Solving for the transverse oscillation  $v_x$ , continuing the algebra, and integrating both sides gives:

$$\gamma m_e v_x = \frac{e B_0 \lambda_w}{2\pi} \cos\left(\frac{2\pi z}{\lambda_w}\right). \quad (2.14)$$

It is suitable to rewrite Eq. 2.14 in terms of the dimensionless undulator parameter,  $a_w$ , as:

$$v_x = \frac{a_w c}{\gamma} \cos\left(\frac{2\pi z}{\lambda_w}\right), \quad (2.15)$$

where:

$$a_w = \frac{e B_0 \lambda_w}{2\pi m_e c}, \quad (2.16)$$

or, in bracketed units:

$$a_w = 0.9337 B_0 [\text{T}] \lambda_w [\text{cm}]. \quad (2.17)$$

In Eq. 2.15, note that  $z$  is not a linear function of time, and  $v_z$  is not constant. The approximation  $z(t) \cong ct$  has been made as the electron is relativistic. Recall that  $\gamma$  is constant in a magnetic field. For motion in the  $xz$ -plane, where  $v_y = 0$ :

$$\gamma \equiv \frac{1}{\sqrt{1 - \frac{v^2}{c^2}}} = \frac{1}{\sqrt{1 - \frac{v_x^2 + v_z^2}{c^2}}}. \quad (2.18)$$

Substitute  $v_x$  from Eq. 2.15 and solve for  $v_z$ :

$$\frac{v_z^2}{c^2} = 1 - \frac{1}{\gamma^2} - \frac{a_w^2}{\gamma^2} \cos^2\left(\frac{2\pi z}{\lambda_w}\right). \quad (2.19)$$

Using the first-order binomial series expansion in the small parameter  $a_w/\gamma$ , substitute the undulator wavenumber  $k_w = 2\pi/\lambda_w$  and  $\cos^2(k_w z) = \frac{1}{2}(1 + \cos(2k_w z))$ :

$$\frac{v_z}{c} = 1 - \frac{1 + a_w^2/2}{2\gamma^2} - \frac{a_w^2}{4\gamma^2} \cos(2k_w z). \quad (2.20)$$

Therefore, the electron velocity in the  $z$ -direction includes a reduced averaged term and an oscillating term at twice the magnet frequency. The averaged electron velocity over an integer number of undulator periods is given by:

$$\bar{\beta}_z = \frac{\bar{v}_z}{c} = 1 - \frac{1 + a_w^2/2}{2\gamma^2}. \quad (2.21)$$

To evaluate and visualise Eq. 2.2, the velocity in the components  $x$  and  $z$  becomes:

$$\beta_x = \frac{a_w}{\gamma} \cos(k_w z), \quad (2.22)$$

$$\beta_z = \bar{\beta}_z - \frac{a_w^2}{4\gamma^2} \cos(2k_w z). \quad (2.23)$$

By integrating and differentiating with respect to time, together with the approximation  $z \cong \bar{\beta}_z ct$ , the electron position and acceleration can also be expressed as:

$$r_{0x} = \frac{a_w}{\gamma \bar{\beta}_z k_w} \sin(k_w z), \quad (2.24)$$

$$r_{0z} = \bar{\beta}_z ct - \frac{a_w^2}{8\gamma^2 \bar{\beta}_z k_w} \sin(2k_w z), \quad (2.25)$$

$$\dot{\beta}_x = -\frac{a_w \bar{\beta}_z c k_w}{\gamma} \sin(k_w z), \quad (2.26)$$

$$\dot{\beta}_z = \frac{a_w^2 \bar{\beta}_z c k_w}{2\gamma^2} \sin(2k_w z). \quad (2.27)$$

The motion of electrons within the undulator, as described by these equations, results in the emission of highly collimated and coherent radiation. This radiation, known

as undulator radiation, has a characteristic wavelength determined by the undulator period and the electron energy. The simulation result illustrating the radiation field emitted from the electron motion within the undulator is shown in Figure 2.4. The figure demonstrates the spatial distribution and intensity of the radiation field at the fourth magnetic period, highlighting the transverse oscillations of the electron and the resulting radiation pattern.

## 2.2 Fundamental Equations of FEL Dynamics

The FEL equation, which will be discussed in Section 2.2.5 is fundamental to understanding the interaction between the electron beam and the radiation field within the undulator. This section derives the FEL equation from the principles of electrodynamics, building upon the concepts of electron motion and radiation discussed in Section 2.1.4. The FEL equation is crucial for describing the dynamics of the electron beam and the radiation field, and it provides the foundation for numerical simulations and theoretical analyses of FEL performance.

### 2.2.1 Radiation Coherence in Free-Electron Lasers

Figure 2.5 illustrates the difference between incoherent and coherent radiation emission from electrons in an FEL. Understanding this distinction is crucial for understanding the fundamental principles of FEL operation and the generation of high-intensity, coherent light.

Incoherent emission occurs when electrons emit radiation independently and out of phase with each other. This is depicted on the left side of Figure 2.5. In this scenario, the emitted wavelets do not align in phase, leading to a random superposition of electromagnetic waves. The resultant radiation is characterised by low intensity and a broad spectrum because the individual contributions from each electron do not add constructively.

In contrast, coherent emission, shown on the right side of Figure 2.5, arises when the electrons emit radiation in phase. This phase alignment occurs when the electron

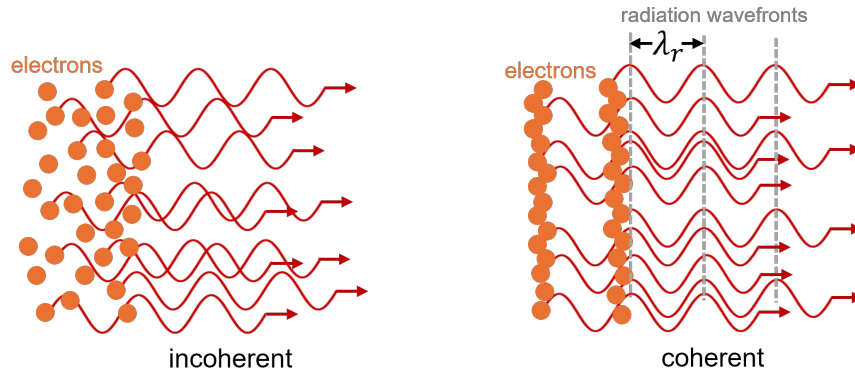


Figure 2.5: Illustration of incoherent and coherent emission from electrons in a Free-Electron Laser (FEL). On the left, electrons emit radiation incoherently, resulting in a superposition of out-of-phase wavelets. On the right, electrons emit radiation coherently, with wavelets in phase, forming distinct wavefronts separated by the radiation wavelength  $\lambda_r$ . The arrows indicate the direction of the electron motion and the emitted radiation. Constructive interference occurs in the coherent emission, significantly increasing the radiation intensity.

bunching matches the periodicity of the emitted wavelets, creating synchronised wavefronts. In this case, the electromagnetic waves constructively interfere, meaning that the peaks and troughs of the waves align, resulting in a significant increase in the overall radiation intensity and a narrow spectral linewidth.

Bunching refers to the process where electrons are grouped together at regular intervals along the undulator, synchronising their oscillations and resulting in coherent radiation emission. As the electrons progress through the undulator, the positive feedback from the radiation itself comes into play. The initial radiation emitted by the electrons induces further oscillations in subsequent electrons, reinforcing the phase alignment and enhancing the coherence of the emitted radiation. This feedback mechanism is crucial for achieving the high degree of coherence characteristic of FELs. The interaction between the electron beam and the periodic magnetic field of the undulator facilitates this process, leading to the generation of intense, monochromatic light.

The transition from incoherent to coherent emission in FELs is achieved through this feedback loop, where the emitted radiation influences the motion of the electrons, causing them to emit more radiation in phase. This self-amplifying process continues over successive undulator periods, resulting in the high-brightness and tunable radiation

output of FELs.

### 2.2.2 Radiation Wavelength Calculation

The radiation emitted by the oscillating electrons in an undulator is influenced by relativistic effects, which cause a Doppler shift of the emitted wavelength. To derive the radiation wavelength, the phase velocity of the radiation and the relativistic Doppler shift must be considered.

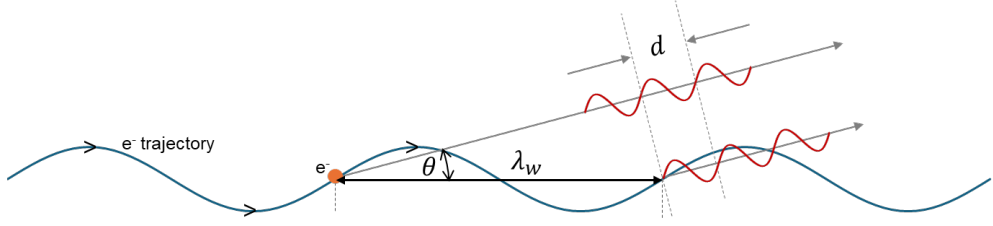


Figure 2.6: Illustration of resonant emission from an electron in an undulator.

Figure 2.6 illustrates the concept of resonant emission from an electron moving through an undulator. The electron follows a sinusoidal trajectory due to the periodic magnetic field of the undulator, and emits radiation at specific wavelengths determined by the resonance condition. The following derivation provides the mathematical foundation for calculating the radiation wavelength.

The averaged time taken for the  $j$ -th electron to travel one undulator period is given by:

$$t_j = \frac{\lambda_w}{c\bar{\beta}_z},$$

where  $\lambda_w$  is the undulator period,  $c$  is the speed of light, and  $\bar{\beta}_z$  is the averaged longitudinal velocity of the electron normalised by the speed of light.

A resonant radiation wavefront will have travelled:

$$t_r = \frac{\lambda_w \cos \theta + n\lambda_r}{c},$$

where  $\theta$  is the observation angle of the radiation relative to the electron's trajectory,  $\lambda_r$  is the radiation wavelength, and  $n$  is the harmonic number.

For the resonance condition, the time it takes for the electron to travel one undulator period must match the time it takes for a radiation wavefront to propagate the same distance. Therefore, setting  $t_j = t_r$  yields:

$$\frac{\lambda_w}{c\bar{\beta}_z} = \frac{\lambda_w \cos \theta + n\lambda_r}{c}$$

Rearranging to solve for the radiation wavelength  $\lambda_r$ :

$$\lambda_r = \frac{\lambda_w}{n} \left( \frac{1}{\bar{\beta}_z} - \cos \theta \right)$$

Next,  $\bar{\beta}_z$  needs to be expressed. The longitudinal velocity  $\bar{\beta}_z$  is modified by the transverse oscillations due to the undulator magnetic field. The expression for  $\bar{\beta}_z$  is (Eq.2.21):

$$\bar{\beta}_z = 1 - \frac{1}{2\gamma^2} \left( 1 + \frac{a_w^2}{2} \right)$$

Substituting this into the radiation wavelength equation results in:

$$\lambda_r = \frac{\lambda_w}{n} \left( \frac{1}{1 - \frac{1}{2\gamma^2} \left( 1 + \frac{a_w^2}{2} \right)} - \cos \theta \right)$$

Using the Taylor series approximation  $\frac{1}{1-x} \approx 1+x$  for  $x \ll 1$ , where  $x = \frac{1}{2\gamma^2} \left( 1 + \frac{a_w^2}{2} \right)$ :

$$\frac{1}{1 - \frac{1}{2\gamma^2} \left( 1 + \frac{a_w^2}{2} \right)} \approx 1 + \frac{1}{2\gamma^2} \left( 1 + \frac{a_w^2}{2} \right)$$

Thus, the equation becomes:

$$\lambda_r = \frac{\lambda_w}{n} \left( 1 + \frac{1 + \frac{a_w^2}{2}}{2\gamma^2} - \cos \theta \right)$$

Using the small angle approximation for  $\cos \theta \approx 1 - \frac{\theta^2}{2}$ :

$$\lambda_r = \frac{\lambda_w}{n} \left( 1 + \frac{1 + \frac{a_w^2}{2}}{2\gamma^2} - \left( 1 - \frac{\theta^2}{2} \right) \right)$$

Thus, the radiation wavelength equation becomes:

$$\lambda_r = \frac{\lambda_w}{2n\gamma^2} \left( 1 + \frac{a_w^2}{2} + \gamma^2\theta^2 \right) \quad (2.28)$$

For the fundamental harmonic ( $n = 1$ ) and on-axis radiation ( $\theta = 0$ ), the fundamental radiation wavelength  $\lambda_r$  simplifies to:

$$\lambda_r = \frac{\lambda_w}{2\gamma^2} \left( 1 + \frac{a_w^2}{2} \right) \quad (2.29)$$

Note that  $a_w$  is derived from the peak value of the magnetic field  $B_0$ . To use the RMS undulator parameter, where  $B_{\text{RMS}} = B_0/\sqrt{2}$ , the radiation wavelength equation becomes:

$$\lambda_r = \frac{\lambda_w}{2n\gamma^2} \left( 1 + \bar{a}_w^2 + \gamma^2\theta^2 \right), \quad (2.30)$$

and on-axis fundamental wavelength is

$$\lambda_r = \frac{\lambda_w}{2\gamma^2} \left( 1 + \bar{a}_w^2 \right). \quad (2.31)$$

Here,  $\bar{a}_w$  is the RMS undulator parameter. This equation is also valid for helical undulators.

The expression for the fundamental resonant wavelength (Eq. 2.31) highlights the origin of the FEL tunability. This relationship shows that the wavelength of the emitted radiation is inversely proportional to the square of the Lorentz factor,  $\gamma$ , which depends on the energy of the electron beam. As the beam energy increases, resulting in a higher  $\gamma$ , the resonant wavelength  $\lambda_r$  shifts to shorter values, allowing the FEL to produce radiation across a wide range of wavelengths. This tunability is a key feature of FELs, enabling them to generate coherent radiation from the infrared to the X-ray region by simply adjusting the electron beam energy and the undulator parameters. This relationship is fundamental to the design and optimisation of FELs for producing radiation at specific wavelengths.

### 2.2.3 Rate of Change of Electron Energy

Understanding the rate of change of the electron energy in a FEL is essential to comprehend the microbunching mechanism that underlies the FEL operation. As electrons travel through the undulator, they interact with the periodic magnetic field and the co-propagating radiation field. These interactions cause variations in the electron energy, leading to the formation of microbunches, where electrons are grouped at intervals corresponding to the radiation wavelength. This microbunching enhances the coherence of the emitted radiation, as electrons within a microbunch radiate in phase, resulting in constructive interference and amplification of the radiation field. By analysing the rate of change of electron energy, insights can be gained into the dynamics of this energy exchange process, which is fundamental to achieving high-intensity, coherent radiation in FELs. The following section derives the expression for the rate of change of electron energy and discusses its implications for the microbunching mechanism and FEL performance.

The rate of change of an electron's energy in the presence of a fixed radiation field can be derived from the Lorentz force equation. Starting from the Lorentz force:

$$\mathbf{F} = -e(\mathbf{E} + \mathbf{v} \times \mathbf{B})$$

The rate of change of the electron energy is given by:

$$\frac{dW}{dt} = \mathbf{v} \cdot \mathbf{F} \tag{2.32}$$

Substituting the Lorentz force:

$$\frac{dW}{dt} = \mathbf{v} \cdot (-e(\mathbf{E} + \mathbf{v} \times \mathbf{B}))$$

The term  $\mathbf{v} \cdot (\mathbf{v} \times \mathbf{B})$  is zero because the dot product of any vector with a vector perpendicular to it (resulting from a cross product) is zero. Therefore:

$$\frac{dW}{dt} = -e\mathbf{v} \cdot \mathbf{E}$$

## Chapter 2. Basic Theory of Free-Electron Lasers

The relativistic energy of the electron is  $\gamma m_0 c^2$ , so the rate of change of energy is:

$$\frac{d(\gamma m_0 c^2)}{dt} = -e\mathbf{v} \cdot \mathbf{E} \quad (2.33)$$

To find  $\frac{d\gamma}{dt}$ , we use the relationship:

$$\frac{d(\gamma m_0 c^2)}{dt} = m_0 c^2 \frac{d\gamma}{dt}$$

Thus:

$$m_0 c^2 \frac{d\gamma}{dt} = -e\mathbf{v} \cdot \mathbf{E}$$

Now, substituting the expressions for the velocity and electric field:

$$\mathbf{v} = c\beta_x \hat{x} + c\beta_z \hat{z}$$

From the provided trajectory equation (2.15):

$$c\beta_x = v_x = \frac{a_w c}{\gamma} \cos\left(\frac{2\pi z}{\lambda_w}\right)$$

And consider the plane-wave electric field:

$$\mathbf{E} = E_0 \cos(k_r z - \omega t) \hat{x}$$

The dot product  $\mathbf{v} \cdot \mathbf{E}$  is:

$$\mathbf{v} \cdot \mathbf{E} = v_x E_0 \cos(k_r z - \omega t)$$

Substituting  $v_x$ :

$$\mathbf{v} \cdot \mathbf{E} = \left( c \frac{a_w}{\gamma} \cos(k_w z) \right) E_0 \cos(k_r z - \omega t)$$

Therefore, the rate of change of the electron's energy is:

$$m_0 c^2 \frac{d\gamma}{dt} = -e \left( c \frac{a_w E_0}{\gamma} \cos(k_w z) \cos(k_r z - \omega t) \right)$$

## Chapter 2. Basic Theory of Free-Electron Lasers

Using the trigonometric identity  $\cos(A)\cos(B) = \frac{1}{2}[\cos(A+B) + \cos(A-B)]$ :

$$\cos(k_w z)\cos(k_r z - \omega t) = \frac{1}{2}[\cos((k_w + k_r)z - \omega t) + \cos((k_w - k_r)z + \omega t)]$$

So:

$$m_0 c^2 \frac{d\gamma}{dt} = -ec \frac{a_w E_0}{2\gamma} [\cos((k_w + k_r)z - \omega t) + \cos((k_w - k_r)z + \omega t)]$$

The rate of change of electron energy  $\frac{d\gamma}{dt}$  becomes:

$$\frac{d\gamma}{dt} = -\frac{ea_w E_0}{2m_0 c \gamma} [\cos((k_w + k_r)z - \omega t) + \cos((k_w - k_r)z + \omega t)] \quad (2.34)$$

The equation for the rate of change of the relativistic factor  $\gamma$  includes two cosine terms, each representing different variations in the phase velocity in  $z$ .

Introducing two phase terms:

$$\theta_s = (k_w + k_r)z - \omega t, \quad (2.35)$$

First Cosine Term:  $\theta_s = (k_w + k_r)z - \omega t$ . The sum of the wave numbers  $k_w + k_r$  indicates a slow spatial variation. This term represents slower oscillations that are more beneficial to a maintained interaction between the electrons and the radiation field.

$$\theta_f = (k_w - k_r)z + \omega t, \quad (2.36)$$

Second Cosine Term:  $\theta_f = (k_w - k_r)z - \omega t$ . The difference of the wave numbers  $k_w - k_r$  indicates a fast spatial variation. This term represents rapid oscillations that average out over longer distances and do not contribute significantly to the sustained energy exchange.

For resonance, the phase velocity of the electron's motion must match the phase velocity of the radiation field. The slow variation term ensures that the phases remain matched over longer distances. The slow oscillations allow the emitted radiation to constructively interfere over many undulator periods, leading to coherent radiation and amplification. The slow variation enables a maintained interaction between the

electron bunches and the radiation field, resulting in continuous energy exchange and efficient amplification.

The following figures illustrate electron bunching and the energy exchange process in the context of resonant emission.

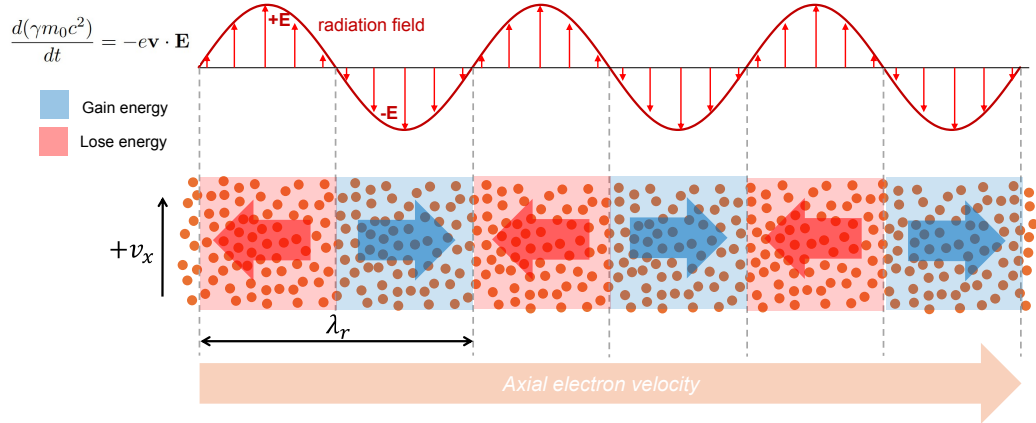


Figure 2.7: Illustration of energy exchange in a FEL. The electron beam travels through the undulator, experiencing periodic regions of energy gain (blue) and energy loss (red). The axial electron velocity and radiation field facilitate energy exchange, indicative of the slow energy exchange process.

The rate of change of electron energy in a FEL is a fundamental concept that explains the microbunching mechanism, which is significant for FEL operation. As electrons travel through the undulator, they interact with the periodic magnetic field and the co-propagating radiation field. This interaction causes periodic variations in the electron energy, leading to the formation of microbunches, where electrons are grouped at intervals corresponding to the radiation wavelength  $\lambda_r$ .

Fig. 2.7 illustrates how electrons experience alternating regions of energy gain (blue) and energy loss (red) as they interact with the radiation field. The energy exchange between the electrons and the radiation field is governed by the interaction of the electron velocity  $\mathbf{v}$  and the electric field  $\mathbf{E}$ , as shown in Eq. 2.33. This continuous modulation of electron energy results in a periodic distribution of energy states along the electron beam's path.

Fig. 2.8 demonstrates how these periodic energy exchanges lead to the formation of microbunches. As electrons gain and lose energy in phase with the radiation field, they

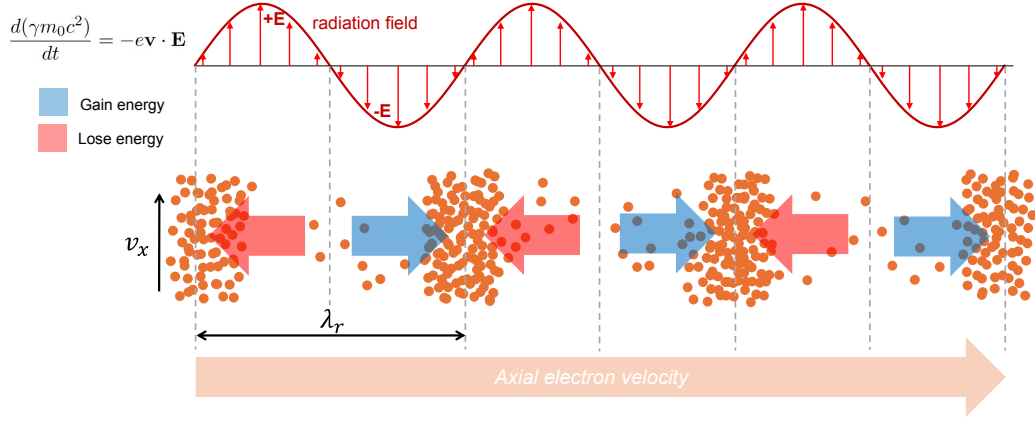


Figure 2.8: Illustration of microbunching and energy exchange in a FEL. The equation  $\frac{d(\gamma m_0 c^2)}{dt} = -e\mathbf{v} \cdot \mathbf{E}$  shows the rate of change of electron energy as they interact with the radiation field. Electrons in blue regions gain energy and move faster, while those in red regions lose energy and move slower, leading to the formation of microbunches that radiate coherently.

cluster into tight bunches at intervals of the radiation wavelength. This microbunching effect enhances the coherence of the emitted radiation because electrons within a microbunch radiate in phase, resulting in constructive interference and amplification of the radiation field. This process is essential for achieving high-intensity, coherent radiation in FELs.

### 2.2.4 One-Dimensional FEL Equations

Recalling the fast and slow varying phase terms from Eq.2.36 and Eq.2.35.

$$\theta_s = (k_w + k_r)z - \omega t$$

$$\theta_f = (k_w - k_r)z + \omega t$$

Differentiating these phase terms with respect to time, we obtain:

$$\frac{d\theta_s}{dt} = (k_w + k_r)\frac{dz}{dt} - \omega$$

$$\frac{d\theta_f}{dt} = (k_w - k_r) \frac{dz}{dt} + \omega$$

The averaged electron velocity over an integer number of undulator periods is given by  $\frac{dz}{dt} = \bar{v}_z = c(1 - \frac{1+a_w^2/2}{2\gamma^2})$ , as seen in Eq.2.21. Thus,

$$\frac{d\theta_s}{dt} = (k_w + k_r)c \left(1 - \frac{1 + \frac{a_w^2}{2}}{2\gamma^2}\right) - \omega$$

Substituting  $\omega = k_r c$  and distributing  $(k_w + k_r)c$ , we get:

$$\frac{d\theta_s}{dt} = k_w c + k_r c - c(k_w + k_r) \left(\frac{1 + \frac{a_w^2}{2}}{2\gamma^2}\right) - k_r c$$

Factoring  $k_w c$  out:

$$\frac{d\theta_s}{dt} = k_w c \left[1 - \frac{k_w + k_r}{k_w} \left(\frac{1 + \frac{a_w^2}{2}}{2\gamma^2}\right)\right]$$

Assuming  $k_r \gg k_w$ , thus  $\frac{k_w+k_r}{k_w} \simeq \frac{k_r}{k_w}$ :

$$\frac{d\theta_s}{dt} = k_w c \left[1 - \frac{k_r}{k_w} \left(\frac{1 + \frac{a_w^2}{2}}{2\gamma^2}\right)\right]. \quad (2.37)$$

Introducing the normalised electron energy,

$$\eta \equiv \frac{\gamma - \gamma_r}{\gamma_r}, \quad (2.38)$$

such that  $\gamma = \gamma_r(1 + \eta)$ , and  $\gamma^2 \cong \gamma_r^2(1 + 2\eta)$  for  $\eta \ll 1$ . Recalling the undulator equation (Eq.2.29) for the resonance condition:

$$\lambda_r = \frac{\lambda_w}{2\gamma_r^2} \left(1 + \frac{a_w^2}{2}\right)$$

$$\frac{\lambda_w}{\lambda_r} \left(\frac{1 + \frac{a_w^2}{2}}{2\gamma_r^2}\right) = \frac{k_w}{k_r} \left(\frac{1 + \frac{a_w^2}{2}}{2\gamma_r^2}\right) = 1$$

substitute this expression and  $\gamma^2$  into Eq.2.37:

$$\frac{d\theta_s}{dt} = k_w c \left(1 - \frac{1}{1 + 2\eta}\right)$$

Using the approximation  $1/(1 + 2\eta) \approx 1 - 2\eta$  for  $\eta \ll 1$ , the equation simplifies to:

$$\frac{d\theta_s}{dt} = 2k_w c \eta \quad (2.39)$$

Following the same algebra the equation for the fast phase term simplifies to:

$$\frac{d\theta_f}{dt} = 2k_w c. \quad (2.40)$$

It should be noted that the fast variation occurs at twice the undulator frequency,  $2k_w$ , resulting in energy exchange in both ways, twice during each undulator period of travel. This rapid oscillation cancels out any significant net energy exchange between the electrons and the field. In contrast, the slow variation,  $d\theta_s/dt$ , is reduced by the factor  $\eta \ll 1$ . This slower and more consistent energy exchange over multiple periods can significantly contribute to the growth of the wave.

From Eq.2.38, we get:

$$\frac{d\gamma}{dt} = \gamma_r \frac{d\eta}{dt}$$

Substituting the rate of change of the electron energy from Eq.2.34 by considering only the slowly varying term, so that the electron energy equation takes the form:

$$\frac{d\eta}{dt} = -\frac{ea_w E_0}{2m_0 c \gamma^2} \cos \theta_s \quad (2.41)$$

The average axial velocity is almost equal to  $c$ , implying  $z \simeq ct$ , the equation for electron position in relation to the wave phase  $\theta_s$ , and normalised energy is given by:

$$\boxed{\frac{d\theta}{dz} = 2k_w \eta} \quad (2.42)$$

$$\boxed{\frac{d\eta}{dz} = -\frac{ea_w E_0}{2m_0 c^2 \gamma^2} \cos \theta} \quad (2.43)$$

Here,  $\theta = \theta_s \equiv (k_w + k_r)z - \omega t$ . These are the coupled equations of motion that describe the oscillation between the electron energy ( $\eta$ ) and position (relative phase,  $\theta$ ) within the combined fields of the wave and the undulator.

### 2.2.5 One-Dimensional Wave Equations

The coupled equations of motion ((2.42) and (2.43)) describe the interaction between the electron beam and the electromagnetic wave in a FEL. These equations account for the dynamics of electron energy and position relative to the wave phase, which are essential for understanding the FEL's operation. In a high gain FEL, the wave amplitude grows exponentially along the undulator length, leading to significant amplification of the emitted radiation. This process is governed by the wave equation, which describes the evolution of the electric field.

The wave equation for an electric field polarized in the x-direction can be written as:

$$\left[ \frac{\partial^2}{\partial t^2} - c^2 \frac{\partial^2}{\partial z^2} \right] E_x(z, t) = -\frac{1}{\epsilon_0} \frac{\partial J_x(z, t)}{\partial t} \quad (2.44)$$

where  $c^2 = \frac{1}{\mu_0 \epsilon_0}$ , and the current density is given by:

$$J_x(z, t) = -en_e(z, t)v_x(z, t). \quad (2.45)$$

In the previous section, a wave of constant amplitude  $E_0$  was used to consider the equation of motion. However, now we wish to consider the growth of the wave in the FEL amplifier. Introducing the complex electric field amplitude  $\tilde{E}_x$ , we can write the monochromatic, one-dimensional wave as:

$$E_x(z, t) = \tilde{E}_x(z) e^{-i(\omega t - kz)} \quad (2.46)$$

where  $\tilde{E}_x(0) = E_0$ .

The time derivative in the wave equation can be found as follows: The first derivative with respect to  $t$  is:

$$\frac{\partial}{\partial t} E_x(z, t) = \tilde{E}_x(z) \frac{\partial}{\partial t} e^{-i(\omega t - kz)} = -i\omega \tilde{E}_x(z) e^{-i(\omega t - kz)},$$

and then, the second derivative with respect to  $t$  is:

$$\frac{\partial^2}{\partial t^2} E_x(z, t) = -i\omega \tilde{E}_x(z) \frac{\partial}{\partial t} e^{-i(\omega t - kz)} = -\omega^2 \tilde{E}_x(z) e^{-i(\omega t - kz)}.$$

For the spatial derivatives, applying the product rule for two  $z$ -dependent functions

$$\frac{d}{dz}[u(z)v(z)] = u(z)\frac{d}{dz}v(z) + v(z)\frac{d}{dz}u(z):$$

$$\frac{\partial}{\partial z}E_x(z, t) = \tilde{E}_x(z) \cdot (ik)e^{-i(\omega t - kz)} + \frac{\partial \tilde{E}_x(z)}{\partial z}e^{-i(\omega t - kz)}$$

and then

$$\frac{\partial^2}{\partial z^2}E_x(z, t) = -k^2\tilde{E}_x(z)e^{-i(\omega t - kz)} + 2ik\frac{\partial \tilde{E}_x(z)}{\partial z}e^{-i(\omega t - kz)} + \frac{\partial^2 \tilde{E}_x(z)}{\partial z^2}e^{-i(\omega t - kz)}$$

Thus, the one-dimensional wave equation becomes:

$$\left[ -\omega^2\tilde{E}_x(z) + k^2c^2\tilde{E}_x(z) - 2ikc^2\frac{\partial \tilde{E}_x(z)}{\partial z} - c^2\frac{\partial^2 \tilde{E}_x(z)}{\partial z^2} \right] e^{-i(\omega t - kz)} = -\frac{1}{\varepsilon_0} \frac{\partial J_x(z, t)}{\partial t}$$

Here, the first two terms cancel by the dispersion relation  $\omega = kc$ , leaving:

$$\left[ 2ik\frac{\partial \tilde{E}_x(z)}{\partial z} + \frac{\partial^2 \tilde{E}_x(z)}{\partial z^2} \right] e^{-i(\omega t - kz)} = \mu_0 \frac{\partial J_x(z, t)}{\partial t} \quad (2.47)$$

for the slowly growing field amplitude,  $\tilde{E}_x(z)$ . Because the field amplitude increases gradually over many wavelengths, the gradient with respect to  $z$ ,  $(\partial/\partial z)^{-1}$ , is much larger than the wavelength  $\lambda = 2\pi/k$  or equivalently,  $\partial/\partial \ll k$ . As a result, the second term in Eq.(2.47) becomes negligible. The one-dimensional wave equation for the slowly growing field thus simplifies to:

$$2ik\frac{\partial \tilde{E}_x(z)}{\partial z}e^{-i(\omega t - kz)} = \mu_0 \frac{\partial J_x(z, t)}{\partial t} \quad (2.48)$$

Multiplying both sides by  $-\frac{i}{2k}e^{i(\omega t - kz)}$ , we obtain:

$$\frac{\partial \tilde{E}_x(z)}{\partial z} = -i\frac{\mu_0}{2k}e^{i(\omega t - kz)} \frac{\partial J_x(z, t)}{\partial t} \quad (2.49)$$

To analyse the slow growth of the wave, we take an average over a small but finite number of cycles within a time interval  $\Delta = 2\pi n/\omega$ , where  $n$  is an integer. This averaging process filters out the high-frequency oscillations. The gradient of the slowly

Chapter 2. Basic Theory of Free-Electron Lasers

varying electric field, averaged over time, is then expressed as:

$$\left\langle \frac{d\tilde{E}_x}{dz} \right\rangle_{\Delta} = -i \frac{\mu_0}{2k} \int_{t-\frac{\Delta}{2}}^{t+\frac{\Delta}{2}} e^{i(\omega t' - kz)} \frac{\partial J_x(z, t')}{\partial t'} dt'$$

Using an integration by parts,  $\int u dv = uv - \int v du$ . Here, let:

$$u = e^{i(\omega t' - kz)} \quad \text{and} \quad dv = \frac{\partial J_x(z, t')}{\partial t'} dt'$$

First, we find  $du$  and  $v$ :

$$du = i\omega e^{i(\omega t' - kz)} dt'$$

Integrating  $dv$  to find  $v$ :

$$v = J_x(z, t')$$

Substituting into integration by parts formula, we obtain:

$$\left\langle \frac{d\tilde{E}_x}{dz} \right\rangle_{\Delta} = -i \frac{\mu_0}{2k} \left\{ \underbrace{\left[ J_x(z, t') e^{i(\omega t' - kz)} \right]_{t-\frac{\Delta}{2}}^{t+\frac{\Delta}{2}}}_0 - i\omega \int_{t-\frac{\Delta}{2}}^{t+\frac{\Delta}{2}} J_x(z, t') e^{i(\omega t' - kz)} dt' \right\}$$

$$\left\langle \frac{d\tilde{E}_x}{dz} \right\rangle_{\Delta} = -\frac{\mu_0 c}{2} \left\langle J_x(z, t) e^{i(\omega t - kz)} \right\rangle_{\Delta} \quad (2.50)$$

Recalling (2.45) and (2.15):

$$J_x(z, t) = -en_e(z, t)v_x(z, t)$$

$$v_x = \frac{a_w c}{\gamma} \cos\left(\frac{2\pi z}{\lambda_w}\right)$$

Then Eq.(2.50) becomes:

$$\left\langle \frac{d\tilde{E}_x}{dz} \right\rangle_{\Delta} = \left\langle \frac{ea_w}{2\epsilon_0 \gamma} n_e(z) \cos(k_w z) e^{i(\omega t - kz)} \right\rangle_{\Delta} \quad (2.51)$$

Expanding the exponential term into its cosine and sine components using  $e^{i\theta} = \cos\theta +$

$i \sin \theta$ , we get:

$$\cos(k_w z) e^{i(\omega t - kz)} = \cos(k_w z) (\cos(\omega t - kz) + i \sin(\omega t - kz))$$

Applying the trigonometric identities  $\cos(A) \cos(B) = \frac{1}{2}[\cos(A+B) + \cos(A-B)]$  and  $\sin(A) \cos(B) = \frac{1}{2}[\sin(A+B) + \sin(A-B)]$ , and recognising the phase terms  $\theta_s$  and  $\theta_f$  from Eq.(2.35) and (2.36), we obtain:

$$\cos(k_w z) e^{i(\omega t - kz)} = \frac{1}{2} \{ (\cos \theta_s + \cos \theta_f) - i(\sin \theta_s - \sin \theta_f) \}$$

The fast phase terms,  $\theta_f$ , average to zero over the slice interval  $\Delta$ . Therefore, the slowly varying gradient simplifies to:

$$\boxed{\frac{d\tilde{E}_x}{dz} = \frac{ea_w}{4\varepsilon_0\gamma} n_e(z) \langle e^{-i\theta_s} \rangle_{\Delta}} \quad (2.52)$$

where the subscript  $\Delta$  denotes averaging over an integer number of cycles.

Combined with the previously derived equations of motion, Eqs. (2.42) and (2.43), we obtain three coupled first-order equations involving the variables,  $\tilde{E}_x$ ,  $\eta$  and  $\theta_s$ . In these equations,  $E_0$  has been replaced by the slowly growing field amplitude,  $\tilde{E}_x$ . For convenience, the three first-order coupled FEL equations are restated here as follows:

$$\frac{d\theta_s}{dz} = 2k_w \eta \quad (2.53)$$

$$\frac{d\eta}{dz} = -\frac{e\hat{K}}{2mc^2\gamma^2} \tilde{E}_x \cos \theta_s \quad (2.54)$$

$$\frac{d\tilde{E}_x}{dz} = \frac{e\hat{K}}{4\varepsilon_0\gamma} n_e e^{-i\theta_s} \quad (2.55)$$

where  $\hat{K}$  as the effective undulator parameter  $\hat{K} = a_w [JJ]$ . The multiplication factor  $[JJ]$  is given by the difference of Bessel function of the first kind, order zero and one,  $[JJ] = J_0(\xi) - J_1(\xi)$ , and  $\xi = a_w^2/4(1 + a_w^2/2)$ .

### 2.2.6 Analysis of the One-Dimensional FEL Differential Equation

To gain a clearer understanding of the dynamics within the FEL system, it is beneficial to combine the coupled first-order differential equations into a single higher-order differential equation. This simplification allows for a more focused analysis on the evolution of the electric field amplitude, which is essential to the operation of the FEL. By removing intermediate variables, the growth and behaviour of the radiation field within the undulator can be more directly assessed. This reduction not only offers deeper insights into the amplification mechanism, but also aids in determining critical parameters such as the power gain length and saturation power. The procedure involves differentiating and substituting the coupled equations, resulting in a third-order differential equation that encapsulates the fundamental physics of the FEL interaction. This method highlights the inherent stability and growth characteristics of the FEL, informing both theoretical analysis and practical design.

The three first-order coupled FEL equations [(2.53), (2.54), and (2.55)] can be linearised and combined into a single third-order differential equation for the slowly varying field amplitude,  $\tilde{E}_x$  by following the FEL process for a distance of only the modest wave growth, where  $\theta_s$  and  $\eta$  remain small, with only slight modulation of  $n_e$ . The linearisation process proceeds by approximating  $\cos \theta_s \simeq 1$  in Eq.(2.54),  $e^{-i\theta_s} \simeq 1 - i\theta_s$  in Eq. (2.55).

By differentiating Eq.(2.55) with respect to  $z$ , we can derive a second-order differential equation for  $\tilde{E}_x$ . This process involves substituting the linearised approximation of Eq.(2.53) and Eq.(2.54) into the resulting expression. Differentiating Eq.(2.55) yields:

$$\frac{d^2 \tilde{E}_x}{dz^2} = \frac{d}{dz} \left( \frac{e\hat{K}}{4\varepsilon_0\gamma} n_e (1 - i\theta_s) \right)$$

$$\frac{d^2 \tilde{E}_x}{dz^2} = \frac{e\hat{K}}{4\varepsilon_0\gamma} n_e \frac{d}{dz} (1 - i\theta_s) = \frac{e\hat{K}}{4\varepsilon_0\gamma} n_e \cdot (-i) \frac{d\theta_s}{dz}$$

Using Eq.(2.53), we have:

$$\frac{d^2 \tilde{E}_x}{dz^2} = \frac{-i2k_w e\hat{K} n_e}{4\varepsilon_0\gamma} \eta$$

Taking the third derivative:

$$\frac{d^3 \tilde{E}_x}{dz^3} = \frac{-i2k_w e \hat{K} n_e}{4\varepsilon_0 \gamma} \frac{d\eta}{dz}$$

Substituting linearised approximation of Eq. (2.54), we obtain:

$$\frac{d^3 \tilde{E}_x}{dz^3} = \frac{ik_w e^2 \hat{K}^2 n_e}{4\varepsilon_0 m c^2 \gamma^3} \tilde{E}_x$$

Thus, the third-order differential equation for the evolving electric field amplitude,  $\tilde{E}_x$  becomes:

$$\frac{d^3 \tilde{E}_x}{dz^3} - i\Gamma^3 \tilde{E}_x = 0 \quad (2.56)$$

where

$$\Gamma = \left[ \frac{\hat{K}^2 e^2 n_e k_w}{4\varepsilon_0 m c^2 \gamma^3} \right]^{1/3} \quad (2.57)$$

This is known as the gain parameter, derived from the coefficients in Eqs.(2.53)-(2.55). Here,  $n_e$  represents the average electron density, and  $k_w = 2\pi/\lambda_w$  denotes the wavenumber related to the undulator period.

We look for solutions of the form  $\tilde{E}_x = E_0 e^{\mu z}$ , where  $\mu$  is a constant to be determined. Substituting into  $\tilde{E}_x = E_0 e^{\mu z}$  the differential equation (2.56) gives:

$$\mu^3 E_0 e^{\mu z} - i\Gamma^3 E_0 e^{\mu z} = 0$$

Factor out  $E_0 e^{\mu z}$ :

$$E_0 e^{\mu z} (\mu^3 - i\Gamma^3) = 0$$

Since  $E_0 e^{\mu z} \neq 0$ , we get the characteristic equation:

$$\mu^3 - i\Gamma^3 = 0,$$

which is the third-order dispersion relation

$$\mu^3 = i\Gamma^3. \quad (2.58)$$

## Chapter 2. Basic Theory of Free-Electron Lasers

To solve for  $\mu$ , take the cube root of both sides:

$$\mu = (i\Gamma^3)^{1/3}$$

The cube root of a complex number has three solutions. Express  $i$  in polar form:

$$i = e^{i\pi/2}$$

Thus, the three solution can be found from:

$$\mu = \Gamma e^{i(\pi/2+2k\pi)/3} \text{ for } k = 0, 1, 2$$

For  $k = 0$ :

$$\begin{aligned} \mu_1 &= \Gamma e^{i\pi/6} = \Gamma \left( \cos \frac{\pi}{6} + i \sin \frac{\pi}{6} \right) \\ \mu_1 &= (i + \sqrt{3})\Gamma/2 \end{aligned} \tag{2.59}$$

For  $k = 1$ :

$$\begin{aligned} \mu_2 &= \Gamma e^{i(5\pi/6)} = \Gamma \left( \cos \frac{5\pi}{6} + i \sin \frac{5\pi}{6} \right) \\ \mu_2 &= (i - \sqrt{3})\Gamma/2 \end{aligned} \tag{2.60}$$

For  $k = 2$ :

$$\begin{aligned} \mu_3 &= \Gamma e^{i(3\pi/2)} = \Gamma \left( \cos \frac{3\pi}{2} + i \sin \frac{3\pi}{2} \right) \\ \mu_3 &= -i\Gamma \end{aligned} \tag{2.61}$$

For the first solution (2.59), the real part,  $\sqrt{3}\Gamma/2$ , is positive, indicating exponential growth. This represents the amplification of the electric field as it travels through the undulator, which is a desired effect in an FEL, where the initial small field gets amplified to produce significant radiation. The imaginary part,  $\Gamma/2$ , indicates oscillatory behaviour. This oscillation arises from the interaction between the electron beam and the radiation field, resulting in periodic energy exchange.

The second solution (2.60), the real part,  $-\sqrt{3}\Gamma/2$ , is negative, indicating expo-

nential decay. This represents the damping or attenuation of the electric field as it propagates. In practice, this could result from energy losses or destructive interference. The imaginary part,  $\Gamma/2$ , is similar to the first solution that indicates oscillatory behaviour. Despite the decay, the field exhibits periodic variations due to the same interaction mechanisms.

The third solution (2.61) has no real part, indicating that it describes purely oscillatory behaviour without any exponential growth or decay. This solution represents steady-state oscillations of the electric field amplitude. Such behaviour might correspond to situations where the gain and loss mechanisms are balanced.

The first solution of an exponentially growing amplitude can be expressed as:

$$\tilde{E}_x = E_0 e^{i(\Gamma/2)z} e^{(\sqrt{3}\Gamma/2)z} \quad (2.62)$$

with a corresponding power growth

$$\hat{P}(z) \propto |\tilde{E}_x|^2 \propto e^{(\sqrt{3}\Gamma)z}$$

In terms of the power gain length,  $L_G$ , which is defined as the distance along the undulator (or wiggler) over which the power of the radiation increases by a factor of  $e$  (the base of natural logarithms).

$$\frac{\hat{P}}{\hat{P}_0} = e^{z/L_G} \quad (2.63)$$

Then,

$$\hat{P}(z) \propto E_0^2 e^{z/L_G} \quad (2.64)$$

where

$$L_G = \frac{1}{\sqrt{3}\Gamma} \quad (2.65)$$

A key dimensionless parameter that arises from the mathematical analysis is the ‘‘FEL parameter’’,  $\rho$ , which was initially introduced in the work of Bonifacio, Pellegrini, and Narducci [11].

$$\rho = \left( \frac{\hat{K}^2 e^2 n_e}{32 \varepsilon_0 \gamma^3 m c^2 k_w^2} \right)^{1/3} \quad (2.66)$$

where the gain parameter,  $\Gamma$ , is corresponding with FEL parameter,  $\rho$  via:

$$\Gamma = \frac{4\pi\rho}{\lambda_w} \quad (2.67)$$

Thus, the gain length can be written in term of FEL parameter,  $\rho$ , as

$$L_G = \frac{\lambda_u}{4\sqrt{3}\pi\rho} \quad (2.68)$$

This equation applies to an idealised one-dimensional FEL amplifier model. However, real-world factors such as finite electron beam energy spread,  $\sigma_\gamma$ , and three-dimensional effects, including the overlap between the electron beam cross-section and the radiation beam, their alignment and co-propagation, and diffraction from the finite size of the radiation emission area, tend to increase the power gain length beyond the value given in (2.68).

In addition to the gain length, another critical parameter that characterises an FEL is its saturation power,  $\hat{P}_{\text{sat}}$ . The saturation power represents the maximum power level that the FEL can achieve before nonlinear effects limit further amplification. It can be expressed as:

$$\hat{P}_{\text{sat}} \simeq \rho\hat{P}_e \quad (2.69)$$

where  $\hat{P}_e = \gamma mc^2 \cdot \hat{I}/e$  is the electron beam energy, and  $\hat{I}/e$  is the number of electrons passing per second. Understanding the saturation power is essential for optimising the performance of FELs.

In summary, the equations derived in this section pertain to the idealised case of a cold, mono-energetic electron beam, where two-dimensional effects are neglected. This simplification allows for a clearer understanding of the fundamental dynamics of the FEL interaction. The analysis focuses on the evolution of the electric field amplitude and provides critical insights into key parameters such as the gain length, and saturation power. These parameters are essential for characterising the performance of the FEL. While real-world FELs must account for factors such as beam energy spread and three-dimensional effects, the idealised model serves as a foundational framework for

understanding the basic principles governing FEL operation and guides the optimisation of practical FEL systems. In experimental settings, the gain lengths are expected to be somewhat longer due to energy spread and variations within the electron beam, highlighting the importance of these factors in practical applications.

### 2.2.7 Universal Scaling

In this section, we delve into a widely adopted method to scale FEL parameters, commonly referred to as universal scaling, as introduced by Bonifacio et al. [11]. This approach is particularly beneficial because it combines various properties of a high-gain FEL into a single parameter,  $\rho$  (known as the FEL, Pierce, or  $\rho$ -parameter). This parameter is a function of the electron beam density and energy, the undulator parameter, the undulator period, and several fundamental constants. Essentially, this scaling provides a way to measure the amplification rate within the FEL, enabling rapid and accurate predictions of FEL performance under a wide array of operational conditions.

To scale the FEL equation, dimensionless variables are introduced and normalised to the FEL parameter, defined as:

$$\rho = \frac{1}{\gamma} \left( \frac{\bar{a}_w \omega_p}{4ck_w} \right)^{\frac{2}{3}} \quad (2.70)$$

where  $\omega_p$  is the plasma frequency, defined as

$$\omega_p = \sqrt{\frac{e^2 n_p}{\epsilon_0 m}} \quad (2.71)$$

and  $n_p$  is the peak electron number density of the electron bunch.

The distance through the undulator,  $z$ , can be scaled as follow

$$\bar{z} = \frac{4\pi\rho}{\lambda_w} z \quad (2.72)$$

or,

$$\bar{z} = 2k_w \rho z \quad (2.73)$$

## Chapter 2. Basic Theory of Free-Electron Lasers

To change the variable from  $z \rightarrow \bar{z}$  in the FEL equations (2.53)-(2.55), we start by expressing the derivative with respect to  $z$  in terms of  $\bar{z}$ :

$$\frac{d\theta}{dz} = \frac{d\theta}{d\bar{z}} \frac{d\bar{z}}{dz} = \frac{d\theta}{d\bar{z}} 2k_w \rho = 2k_w \eta$$

The scaled rate of change of phase equation becomes,

$$\frac{d\theta}{d\bar{z}} = p \quad (2.74)$$

where we introduced  $p$  is the scaled normalised electron energy, can be expressed as:

$$p = \frac{\eta}{\rho} = \frac{\gamma - \gamma_r}{\rho \gamma_r} \quad (2.75)$$

Next, the rate of change of electron energy (2.54),

$$\frac{d\eta}{dz} = \frac{dp}{d\bar{z}} \frac{d\eta}{dp} \frac{d\bar{z}}{dz} = \frac{dp}{d\bar{z}} 2k_w \rho^2 = -\frac{e\hat{K}}{2mc^2\gamma^2} \tilde{E} \cos \theta$$

The scaled rate of change of electron energy becomes:

$$\frac{dp}{d\bar{z}} = -A \cos \theta \quad (2.76)$$

where we introduced  $A$  is the complex scaled field amplitude, defined as:

$$A = \frac{e\hat{K}}{4mc^2k_w\rho^2\gamma^2} \tilde{E} \quad (2.77)$$

The 1D-wave equation (2.55) can be now changed into the scaled variable as follow:

$$\frac{d\tilde{E}}{dz} = \frac{dA}{d\bar{z}} \cdot \frac{d\tilde{E}}{dA} \cdot \frac{d\bar{z}}{dz} = \frac{dA}{d\bar{z}} \cdot \frac{4mc^2k_w\rho^2\gamma^2}{e\hat{K}} \cdot (2k_w\rho) = \frac{e\hat{K}}{4\varepsilon_0\gamma} n_e e^{-i\theta}$$

$$\frac{dA}{d\bar{z}} = \frac{\hat{K}^2 e^2 n_e}{32\varepsilon_0\gamma^3 mc^2 k_w^2 \rho^3} e^{-i\theta}$$

recognising the  $\rho$ -parameter from Eq.(2.66). Thus, the scaled 1D wave equation be-

comes:

$$\frac{dA}{d\bar{z}} = e^{-i\theta} \quad (2.78)$$

For convenience, the scaled three first-order coupled FEL equations are restated here as follows:

$$\frac{d\theta}{d\bar{z}} = p \quad (2.79)$$

$$\frac{dp}{d\bar{z}} = -A \cos \theta \quad (2.80)$$

$$\frac{dA}{d\bar{z}} = e^{-i\theta} \quad (2.81)$$

Performing the linearised approximation similar to process from the previous section. The third order differential equation for the scaled field amplitude,  $A$ , becomes:

$$\frac{d^3 A}{d\bar{z}^3} - iA = 0 \quad (2.82)$$

Assuming the solution of the form  $A = A_0 e^{\lambda\bar{z}}$ , the third-order dispersion relation becomes:

$$\lambda^3 = i \quad (2.83)$$

with three solutions

$$\lambda_1 = -i, \quad \lambda_2 = \frac{i}{2} - \frac{\sqrt{3}}{2}, \quad \lambda_3 = \frac{i}{2} + \frac{\sqrt{3}}{2} \quad (2.84)$$

The first solution corresponds to an oscillatory mode with a constant amplitude, the second to a damped oscillation, and the third to a wave with exponentially growing amplitude, which is the key characteristic of the high-gain FEL. This can be expressed as:

$$A = A_0 e^{i(\bar{z}/2)} e^{\sqrt{3}\bar{z}/2} \quad (2.85)$$

with the corresponding scaled intensity growth given by:

$$|A(\bar{z})|^2 \propto e^{\sqrt{3}\bar{z}} \propto e^{\sqrt{3}z/l_g} \quad (2.86)$$

where  $l_g = \sqrt{3}L_G$  is the nominal gain length in the context of universal scaling. This parameter relates to the FEL parameter,  $\rho$ , via:

$$l_g = \frac{\lambda_w}{4\pi\rho} \quad (2.87)$$

Another important scaled parameter is  $l_c$ , the cooperation length, which is defined by the relative slippage length between radiation and electrons over one gain length:

$$l_c = l_g \frac{\lambda_r}{\lambda_w} = \frac{\lambda_r}{4\pi\rho} \quad (2.88)$$

where  $\lambda_r$  is the radiation wavelength.

The analysis of high-gain FELs involves the introduction of scaled independent variables to describe the dynamics in different reference frames. These variables facilitate understanding the interactions between the electron beam and the radiation field within the undulator. The scaled variables are particularly useful for describing the evolution of the system and simplifying the equations governing FEL operation.

First,  $(\bar{z}_1, \bar{z})$  are the scaled distances along the undulator and within a window travelling at the resonant electron velocity along  $z$ , representing the electron frame of reference. This scaling captures the dynamics relative to the electron beam's motion:

$$\bar{z}_1 = \frac{z - c\bar{\beta}_z t}{l_c \bar{\beta}_z} \quad (2.89)$$

where  $c\bar{\beta}_z$  is the mean electron velocity in the  $z$  direction. This scaled variable is crucial for analysing how the radiation interacts with the electron beam from the perspective of the electrons.

Second,  $(\bar{z}_2, \bar{z})$  are the scaled distances along the undulator and within a window travelling at the speed of light  $c$  along  $z$ , representing the radiation frame of reference. This scaling focuses on the dynamics relative to the radiation field:

$$\bar{z}_2 = \frac{ct - z}{l_c} \quad (2.90)$$

These scaled variables provide insights into the behaviour of the radiation as it propa-

gates through the undulator.

It is important to note that  $\bar{z}$ , the total scaled distance along the undulator, is related to the electron and radiation frames by:

$$\bar{z} = \bar{z}_1 + \bar{z}_2 \tag{2.91}$$

These scaled variables, particularly  $(\bar{z}_2, \bar{z})$ , are widely used in numerical simulations such as those performed with the code Puffin and will be applied throughout the following chapters of this thesis. By introducing these scaled parameters, complex physical phenomena within the FEL can be expressed in a more manageable form. This approach not only facilitates the mathematical manipulation of the equations, but also enhances the physical intuition behind the behaviour of the system.

For instance, using the scaled parameters  $\bar{z}_1$  and  $\bar{z}_2$  allows for a clear distinction between the electron and radiation reference frames, enabling a more precise analysis of their interaction within the undulator. The scaled gain length  $l_g$  and cooperation length  $l_c$  help standardise the descriptions of gain and slippage effects, respectively, across different FEL configurations, making comparative studies more straightforward. Furthermore, these parameters align with the universal scaling laws, providing a unified framework for understanding the scaling behaviour of FELs with respect to their fundamental parameters such as the wavelength  $\lambda$ , the undulator period  $\lambda_w$  and the FEL parameter  $\rho$ .

## 2.3 Basic Optics Theory for the Cavity-Based Free-Electron Laser

### 2.3.1 Ray Transfer Matrix Analysis

The ray transfer matrix method is an analytical tool used to describe the propagation of light rays through an optical system. Each optical element within the system, such as lenses, mirrors, and free space, can be represented by a 2x2 matrix, often referred to as the ABCD matrix. By multiplying these matrices, one can determine the overall effect

of a series of optical elements on a light ray. In the context of a FEL optical cavity, the ABCD matrix method is instrumental in analysing the stability of the optical cavity and the behaviour of the optical modes.

In the paraxial approximation, when all angles are sufficiently small ( $\sin \theta \simeq \theta$ ), the optical ray can be described by its height,  $y$ , and angle,  $\theta$ , with respect to the optical axis. The transformation of this ray through an optical element can be described by:

$$\begin{bmatrix} y_1 \\ \theta_1 \end{bmatrix} = \begin{bmatrix} A & B \\ C & D \end{bmatrix} \begin{bmatrix} y_0 \\ \theta_0 \end{bmatrix} \quad (2.92)$$

where the matrix  $\mathbf{M}$ , with elements  $A, B, C$ , and  $D$ , represents the optical properties of the system.  $\begin{bmatrix} y_0 \\ \theta_0 \end{bmatrix}$  and  $\begin{bmatrix} y_1 \\ \theta_1 \end{bmatrix}$  are the ray vectors denoting the ray's height and angle before and after the optical element, respectively.

The ABCD matrix for common optical elements are as follows:

- Free Space Propagation (distance  $d$ ):

$$\mathbf{M} = \begin{bmatrix} 1 & d \\ 0 & 1 \end{bmatrix} \quad (2.93)$$

- Thin Lens (focal length  $f$ ):

$$\mathbf{M} = \begin{bmatrix} 1 & 0 \\ -\frac{1}{f} & 1 \end{bmatrix} \quad (2.94)$$

- Mirror (radius of curvature  $R$ ):

$$\mathbf{M} = \begin{bmatrix} 1 & 0 \\ -\frac{2}{R} & 1 \end{bmatrix} \quad (2.95)$$

The ray transfer matrix can be used in cascaded optical systems, leading to the formation of periodic optical systems such as a cavity. By considering the combined effect of multiple optical elements in sequence, one can analyse complex optical systems and determine the overall transformation matrix. This approach is particularly useful

for understanding the behaviour of optical cavities, where the periodic nature of the system leads to the eigenvalue problem. Solving this eigenvalue problem allows for the determination of the stability and resonance conditions of the cavity, providing insights into the modes supported by the system and their respective properties.

Consider a periodic optical system where the light ray traverses through a sequence of optical elements and returns to its starting point after one round trip. The overall ray transfer matrix for one round trip in the cavity is denoted by  $\mathbf{M}$ , and is given by:

$$\mathbf{M} = \mathbf{M}_n \cdot \mathbf{M}_{n-1} \cdot \dots \cdot \mathbf{M}_2 \cdot \mathbf{M}_1$$

where  $\mathbf{M}_i$  represents the ray transfer matrix of the  $i$ -th optical element in the sequence.

For the optical cavity to be stable, the eigenvalues of the round-trip matrix  $\mathbf{M}$  must be in the complex unit circle. The equation of eigenvalues for the matrix  $\mathbf{M}$  is given by:

$$\mathbf{M} \begin{bmatrix} y \\ \theta \end{bmatrix} = \lambda \begin{bmatrix} y \\ \theta \end{bmatrix}$$

where  $\lambda$  represents the eigenvalues of the matrix  $\mathbf{M}$ . This can also be rewritten as:

$$(\mathbf{M} - \lambda \mathbf{I}) \begin{bmatrix} y \\ \theta \end{bmatrix} = 0 \tag{2.96}$$

where  $\mathbf{I}$  is the identity matrix.

For the system to have a non-trivial solution (i.e.  $\begin{bmatrix} y \\ \theta \end{bmatrix} \neq 0$ ), the determinant of the matrix  $(\mathbf{M} - \lambda \mathbf{I})$  must be zero: To find the eigenvalues, we solve the characteristic equation:

$$\det(\mathbf{M} - \lambda \mathbf{I}) = 0$$

where  $\mathbf{I}$  is the identity matrix. For a 2x2 matrix  $\mathbf{M}$ , this expands to:

$$\det \begin{bmatrix} A - \lambda & B \\ C & D - \lambda \end{bmatrix} = 0$$

$$(A - \lambda)(D - \lambda) - BC = 0$$

$$\lambda^2 - (A + D)\lambda + (AD - BC) = 0$$

The solutions to this quadratic equation are the eigenvalues  $\lambda_1$  and  $\lambda_2$ , given by:

$$\lambda_{1,2} = \frac{(A + D) \pm \sqrt{(A + D)^2 - 4(AD - BC)}}{2}$$

For the cavity to be stable, the magnitudes of the eigenvalues must be equal to 1. This condition can be satisfied if the trace of the matrix  $\mathbf{M}$ , which is  $A + D$ , satisfies:

$$-2 \leq A + D \leq 2$$

This inequality ensures that the real part of the eigenvalues lies between -1 and 1, corresponding to stable periodic orbits of the optical rays within the cavity. Solving the eigenvalue problem allows us to determine the stability and resonance conditions of the cavity, providing insights into the modes supported by the system and their respective properties.

### 2.3.2 Two-mirror optical cavity stability

A straightforward cavity design for the FEL oscillator is based on the semi-concentric configuration. In this setup, the optical waist position of the cavity is located between the two mirrors, depending on their radii of curvature. This configuration is ideal for maintaining the optical beam confined within the FEL undulator, enhancing the electron/light interaction during the amplification process of FEL operation.

To analyse the stability of an optical cavity, one needs to consider the round-trip ABCD matrix of the cavity. For a cavity consisting of two mirrors separated by a distance  $L$ , the round-trip ABCD matrix is given by the product of the matrices representing each segment of the optical path:

- Propagation from mirror 1 to mirror 2 over a distance  $L$ :

$$\mathbf{M}_1 = \begin{bmatrix} 1 & L \\ 0 & 1 \end{bmatrix}$$

- Reflection from mirror 2 (radius of curvature  $R_2$ ):

$$\mathbf{M}_2 = \begin{bmatrix} 1 & 0 \\ -\frac{2}{R_2} & 1 \end{bmatrix}$$

- Propagation from mirror 2 to mirror 1 over a distance  $L$ :

$$\mathbf{M}_3 = \begin{bmatrix} 1 & L \\ 0 & 1 \end{bmatrix}$$

- Reflection from mirror 1 (radius of curvature  $R_1$ ):

$$\mathbf{M}_4 = \begin{bmatrix} 1 & 0 \\ -\frac{2}{R_1} & 1 \end{bmatrix}$$

The round-trip matrix  $\mathbf{M}_{\text{rt}}$  is obtained by multiplying these matrices in sequence:

$$\mathbf{M}_{\text{rt}} = \mathbf{M}_4 \cdot \mathbf{M}_3 \cdot \mathbf{M}_2 \cdot \mathbf{M}_1$$

Substituting the individual matrices, we get:

$$\mathbf{M}_{\text{rt}} = \begin{bmatrix} 1 & 0 \\ -\frac{2}{R_1} & 1 \end{bmatrix} \begin{bmatrix} 1 & L \\ 0 & 1 \end{bmatrix} \begin{bmatrix} 1 & 0 \\ -\frac{2}{R_2} & 1 \end{bmatrix} \begin{bmatrix} 1 & L \\ 0 & 1 \end{bmatrix}$$

Performing the matrix multiplications:

$$\mathbf{M}_{\text{rt}} = \begin{bmatrix} A & B \\ C & D \end{bmatrix}_{\text{rt}} = \begin{bmatrix} 1 - \frac{2L}{R_2} & 2L - \frac{2L^2}{R_2} \\ \frac{4L}{R_1 R_2} - \frac{2}{R_1} - \frac{2}{R_2} & 1 + \frac{4L^2}{R_1 R_2} - \frac{4L}{R_1} - \frac{2L}{R_2} \end{bmatrix}$$

The stability of the cavity is determined by the eigenvalues of the round-trip matrix

$\mathbf{M}_{rt}$ . The cavity is stable if the absolute values of the eigenvalues are less than or equal to 1. This can be expressed in terms of the trace of the matrix:

$$|A + D| \leq 2, \quad (2.97)$$

which can also be expressed as:

$$-1 \leq \frac{A + D}{2} \leq 1. \quad (2.98)$$

For convenience, it can be rewritten by adding 1 to both sides and dividing by 2, resulting in:

$$0 \leq \frac{A + D + 2}{4} \leq 1 \quad (2.99)$$

Substituting the elements  $A$  and  $D$  of  $\mathbf{M}_{rt}$  into 2.99, the cavity will be stable if and only if:

$$0 \leq \frac{(1 - \frac{2L}{R_2}) + (1 + \frac{4L^2}{R_1 R_2} - \frac{4L}{R_1} - \frac{2L}{R_2}) + 2}{4} \leq 1$$

When simplified, this becomes:

$$0 \leq \left(1 - \frac{L}{R_1}\right) \left(1 - \frac{L}{R_2}\right) \leq 1 \quad (2.100)$$

This is the well-known stability criterion for a two-mirror optical cavity, the two terms in the product are defined as:

$$g_1 \equiv 1 - \frac{L}{R_1} \quad \text{and} \quad g_2 \equiv 1 - \frac{L}{R_2} \quad (2.101)$$

indicating that the cavity will be stable if the product of the terms  $g_1$  and  $g_2$  lies within the range  $[0, 1]$ . This ensures that the optical beam remains confined and stable within the FEL undulator, enhancing the overall amplification performance of the FEL system.

### 2.3.3 Gaussian beam propagation

From ray optics, we now shift our focus to Gaussian optics, which is crucial for understanding beam propagation in FEL cavities. The optical cavity of an FEL is a critical component that determines the efficiency and stability of the laser. Understanding Gaussian beam propagation principles is essential for designing these cavities to ensure optimal interaction between the electron beam and the optical field. This section discusses the propagation of Gaussian beams in FEL cavities, addressing key parameters, design considerations, and the challenges involved in optimising these systems.

A Gaussian beam is a specific type of beam in which the electric field distribution follows a Gaussian function. This beam profile is characterised by several key parameters that define its spatial and propagation properties. The fundamental equation describing a Gaussian beam is given by:

$$\Psi(x, y, z) = \Psi_0 \frac{w_0}{w(z)} \exp\left(-\frac{x^2 + y^2}{w(z)^2}\right) \exp\left(i\left(kz + k\frac{x^2 + y^2}{2R(z)} - \zeta(z)\right)\right) \quad (2.102)$$

Here,  $\Psi(x, y, z)$  is the complex amplitude of the electric field, and  $\Psi_0$  is a normalisation constant. The key characteristics of the Gaussian beam are:

- **Beam Waist ( $w_0$ ):** This is the location along the beam propagation direction where the beam radius is at its minimum. It represents the tightest focus of the beam.
- **Beam Radius ( $w(z)$ ):** The radius of the beam at a distance  $z$  from the waist, given by:

$$w(z) = w_0 \left(1 + \left(\frac{z}{z_R}\right)^2\right) \quad (2.103)$$

This equation shows that the beam expands as it propagates away from the waist.

- **Rayleigh Range ( $z_R$ ):** The Rayleigh range is the distance from the beam waist to the point where the beam area has doubled. It is given by:

$$z_R = \frac{\pi w_0^2}{\lambda} \quad (2.104)$$

where  $\lambda$  is the wavelength of the light. Within the Rayleigh range, the beam remains relatively collimated.

- **Beam Divergence Angle ( $\theta$ ):** Far from the waist, the beam diverges at a constant angle. The divergence angle is:

$$\theta = \frac{\lambda}{\pi w_0} \quad (2.105)$$

- **Radius of Curvature ( $R(z)$ ):** The radius of curvature of the beam's wavefront at a distance  $z$  from the waist is:

$$R(z) = z \left( 1 + \left( \frac{z_R}{z} \right)^2 \right) \quad (2.106)$$

At the beam waist ( $z = 0$ ),  $R_z \rightarrow \infty$ , indicating a flat wavefront.

- **Gouy Phase Shift ( $\zeta(z)$ ):** The Gouy phase shift represents an additional phase change that occurs as the beam propagates through the waist. It is given by:

$$\zeta(z) = \tan^{-1} \left( \frac{z}{z_R} \right) \quad (2.107)$$

The schematic representation in Figure 2.9 illustrates the variation in beam size  $w(z)$  and wavefront curvature  $R(z)$  as functions of the distance  $z$  from the beam waist, providing a visual understanding of the beam's propagation characteristics..

These parameters are essential for understanding and describing the behaviour of Gaussian beams, which are fundamental to designing and optimising the optical cavities in FELs. Properly managing these characteristics ensures that the beam remains well-confined and interacts efficiently with the electron beam in the undulator.

When a Gaussian beam is reflected by a spherical mirror, it retraces its path if the radius of curvature of the beam's wavefront matches the radius of curvature of the mirror. This principle is fundamental in designing optical cavities for FELs. The Gaussian beam has a specific wavefront curvature that changes as it propagates. At the beam waist, the curvature is zero. As the beam moves away from the waist, the

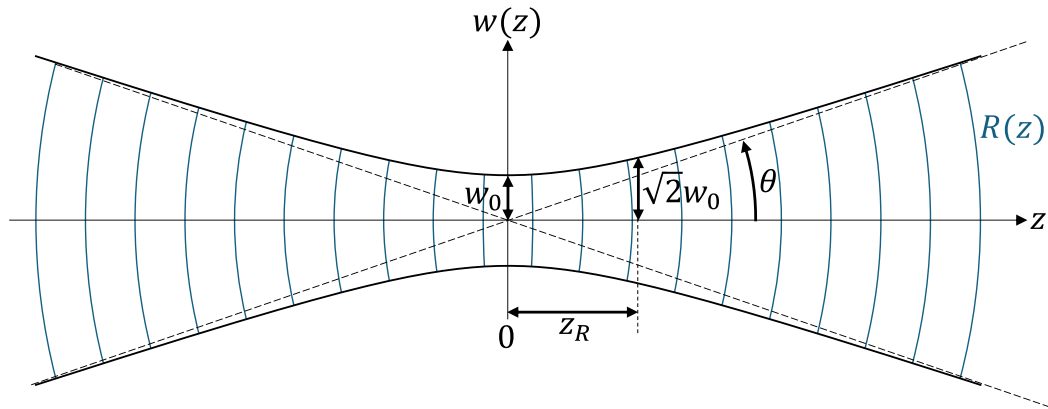


Figure 2.9: Schematic representation of Gaussian beam propagation. The plot illustrates the variation in beam size  $w(z)$  as a function of the distance  $z$  from the beam waist. The wavefront curvature  $R(z)$  is also depicted, showing the changing curvature of the beam's phase front as it propagates. The beam waist is located at  $z = 0$ , where the beam radius is at its minimum, and the Rayleigh range  $z_R$  is marked, indicating the distance over which the beam radius increases by a factor of  $\sqrt{2}$ . The figure highlights how the Gaussian beam expands and changes curvature as it moves away from the waist, providing a visual understanding of the beam's propagation characteristics.

curvature increases. By positioning spherical mirrors such that their radii of curvature match the beam's wavefront curvature at the points of reflection, the beam is confined within the cavity, maintaining its path, and ensuring stability.

As we can see from Figure 2.10, the red shaded area represents the cross-sectional profile of the beam, which narrows at the beam waist and diverges as it moves away from this point. The blue lines indicate the wavefronts, showing how they transition from flat at the waist to curved as the beam propagates. The optical cavity is formed by two spherical mirrors with radii of curvature  $R_1$  and  $R_2$ , positioned at distances  $L_1$  and  $L_2$ , from the beam waist, respectively. These mirrors ensure that the beam retraces its path upon reflection, maintaining the correct radius of curvature of the beam's wavefront to match that of the mirrors.

In summary, the precise design of the optical cavity using spherical mirrors with matching radii of curvature is crucial to achieve stable and efficient FEL operation. The mirrors provide the necessary optical feedback and mode selection, ensuring high beam quality and effective interaction with the electron beam. This configuration enhances the amplification process, leading to a high-quality laser output.

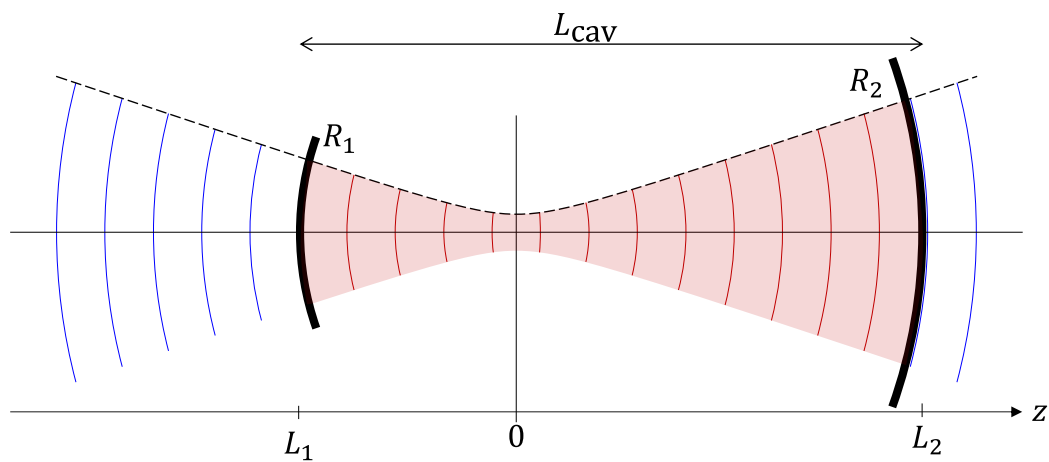


Figure 2.10: Propagation of a Gaussian laser beam through an FEL optical cavity formed by two spherical mirrors with radii of curvature  $R_1$  and  $R_2$ . The red area represents the beam's cross-sectional profile, with the beam waist at the centre and divergence as it moves away from the waist. The blue lines depict the wavefronts of the laser beam, showing the change in curvature during propagation. The spherical mirrors, positioned at distances  $L_1$  and  $L_2$  from the beam waist, ensure that the reflected beam retraces the incident path.

## Chapter 3

# Unaveraged Models of a Cavity-Based Free-Electron Laser

The simulation of a cavity-based (oscillator) free electron laser (FEL) requires the modelling of both the interaction between electrons and light within the FEL undulator as well as the propagation of radiation inside the optical cavity. The 3D unaveraged FEL simulation code, Puffin, has been integrated with the Optical Propagation Code (OPC) to enable the first time modelling of a broadband, high temporal-resolution cavity FEL. This integration requires converting the radiation field formats between the Puffin and OPC codes. The process of this conversion is detailed, and the combined codes are utilised to simulate a Regenerative Amplifier FEL (RAFEL) example operating in the VUV spectrum.

### 3.1 Introduction

To simulate a Free Electron Laser functioning within an optical cavity (oscillator), it is typically necessary to use two distinct simulation codes: one for modelling the FEL interaction in the undulator system and another for simulating the radiation travel through the optical cavity. Different 3D FEL simulation codes, including Genesis 1.3 [67], are capable of simulating the FEL interaction using the Slowly Varying Envelope Approximation (SVEA). In contrast, Puffin [14, 16] (accessible from [15]) op-

erates as an unaveraged FEL code that neither applies the SVEA approximation nor utilises the undulator period averaging for electron trajectories. This unaveraged approach retains the rapidly oscillating term of the radiation field, enabling the simulation of broadband radiation fields (few-cycle) and more intricate electron dynamics. This chapter presents a methodology for achieving such unaveraged modelling within a FEL oscillator system.

Previously, the Genesis 1.3 FEL simulation code has been combined with the Optical Propagation Code (OPC) [32, 76] (accessible from [31]), to model a cavity-based Regenerative Amplifier FEL functioning in the VUV, by employing both codes in sequence within the optical cavity [44]. The OPC incorporates 3D mirror reflections and the propagation in free space through the cavity's optical path.

In this study, OPC is utilised to simulate the optical propagation within a cavity, whereas the direct FEL interaction is captured using Puffin. This chapter initially explains the process of converting the optical field between the Puffin and OPC code formats, which is essential for connecting the radiation output from one code to the other. The conversion code can be accessed here [55] (see also in D).

When designing an FEL oscillator intended to function at shorter wavelengths approaching the X-ray range, the optical components forming the cavity can be restrictive due to their lower reflectivity, increased absorption, and lack of tunability, especially when using Bragg reflectors. The Regenerative Amplifier FEL (RAFEL) employs a high-gain FEL undulator system operating below saturation, alongside a minimised optical feedback cavity to achieve FEL saturation within a few cavity round-trips. RAFEL generally utilises low reflectivity mirrors for the optical cavity, enabling operation within the short wavelength domain [41]. A summary of RAFEL performance over a broad parameter range in the 1D limit is provided in [24]. The model of a RAFEL design that operates in the VUV at approximately 65 nm is then presented. The optical cavity was designed to fulfil the cavity stability requirements and to align the undulator and cavity lengths with the electron beam repetition rate.

### 3.2 Field Format Conversion

The Puffin radiation field data is stored as a 4-dimensional array in an HDF5 (.h5) file. It has dimensions of  $(2, n_z, n_y, n_x)$  that represent two orthogonal polarised 3D fields in the  $x$  and  $y$  directions, with  $n_z$  indicating the field propagation direction. Figure 3.1 shows a diagram for converting the format of a short Gaussian pulse. The Puffin output field includes the ‘fast’ oscillatory components of the radiation for both  $x$  and/or  $y$  polarisations, allowing for conversion to both planar and circular polarisations.

Unlike Puffin, which uses a single HDF5 file to store the radiation field, OPC utilises two separate files. The first is a binary data file in the Genesis field format (.dff) [67]. Each data point is represented as an 8-byte (64-bit) floating point number and stored in a 1D array. The size of this array is determined by the product of the grid points in  $x$ ,  $y$ , and  $z$ , with grid size parameters and the number of slices in  $z$  stored in a second text file with OPC parameters (.param). The transverse optical field data comprises pairs forming complex numbers, interleaved in the array at odd and even indices. For temporal data in the OPC files, the number of slices corresponds to the additional axis of the array that corresponds to the  $z$ -direction of optical propagation.

The Python script for converting from the Puffin to OPC file format starts by analysing the optical field envelope in its complex form. The conversion technique independently handles both the  $x$  and  $y$  polarisations of the Puffin field. For a basic plane wave, the radiation field for a single polarisation direction derived from Puffin can be expressed in Eq. 3.1 as:

$$A_{puffin}(\mathbf{r}, t) = A_0(\mathbf{r}, t) \cos(kz - \omega t + \phi(\mathbf{r}, t)), \quad (3.1)$$

where  $A_{puffin}$  is the scaled radiation field with amplitude  $A_0$ , radiation wave number  $k$ , angular frequency  $\omega$  and phase  $\phi$ . An analytic form is then used to translate the real-value field  $A_{puffin}$  into the complex representation of the OPC field format by using a Hilbert transform [36], which also has the effect of shifting the phase of the original signal by  $-\pi/2$ . The Hilbert transform, denoted by a ‘hat’, of the Puffin field can then

be expressed as:

$$\begin{aligned}\hat{A}_{puffin}(\mathbf{r}, t) &= \mathcal{H}[A_{puffin}(\mathbf{r}, t)] \\ &= A_0(\mathbf{r}, t) \sin(kz - \omega t + \phi(\mathbf{r}, t))\end{aligned}\quad (3.2)$$

The OPC envelope is then constructed from the original Puffin field via its Hilbert transform, as:

$$\begin{aligned}\tilde{A}_{opc}(\mathbf{r}, t) &= A_{puffin}(\mathbf{r}, t) + i\hat{A}_{puffin}(\mathbf{r}, t) \\ &= A_0(\mathbf{r}, t) \exp[i(kz - \omega t + \phi(\mathbf{r}, t))]\end{aligned}\quad (3.3)$$

In this way,  $A_{puffin}(\mathbf{r}, t) = \text{Re}(\tilde{A}_{opc}(\mathbf{r}, t))$ .

In practice, Puffin stores the radiation field data as a function of  $\bar{z}_2 = (ct - z)/l_c$ , where  $l_c = \lambda_r/(4\pi\rho)$  is the cooperation length,  $\lambda_r$  is the resonant radiation wavelength and  $\rho$  is the FEL parameter [14]. When converting the Puffin field into the OPC format, the negative imaginary part must therefore be used so that:

$$\begin{aligned}\tilde{A}_{opc}(\mathbf{r}, \bar{z}_2) &= A_{puffin}(\mathbf{r}, \bar{z}_2) - i\hat{A}_{puffin}(\mathbf{r}, \bar{z}_2) \\ &= A_0(\mathbf{r}, \bar{z}_2) \exp[i(\bar{z}_2/2\rho - \phi(\mathbf{r}, \bar{z}_2))]\end{aligned}\quad (3.4)$$

The parameters that define the grid size, number of grid points, and so on, for both transverse and temporal directions, are first derived from the Puffin scaled parameters as detailed in [14]. These are then converted into OPC scaling and documented in the OPC parameter text file. For the reverse transformation from OPC binary format to Puffin HDF5 format, the method extracts the real part of the OPC data file, reads the number of grid points, grid size, etc., from the OPC parameter text file, and inputs this information into the Puffin HDF5 file format.

### 3.3 Simulation parameters

In the simulation described here, a steady-state (non-pulsed) interaction is considered, with parameters that are similar to those outlined in the 4GLS conceptual design

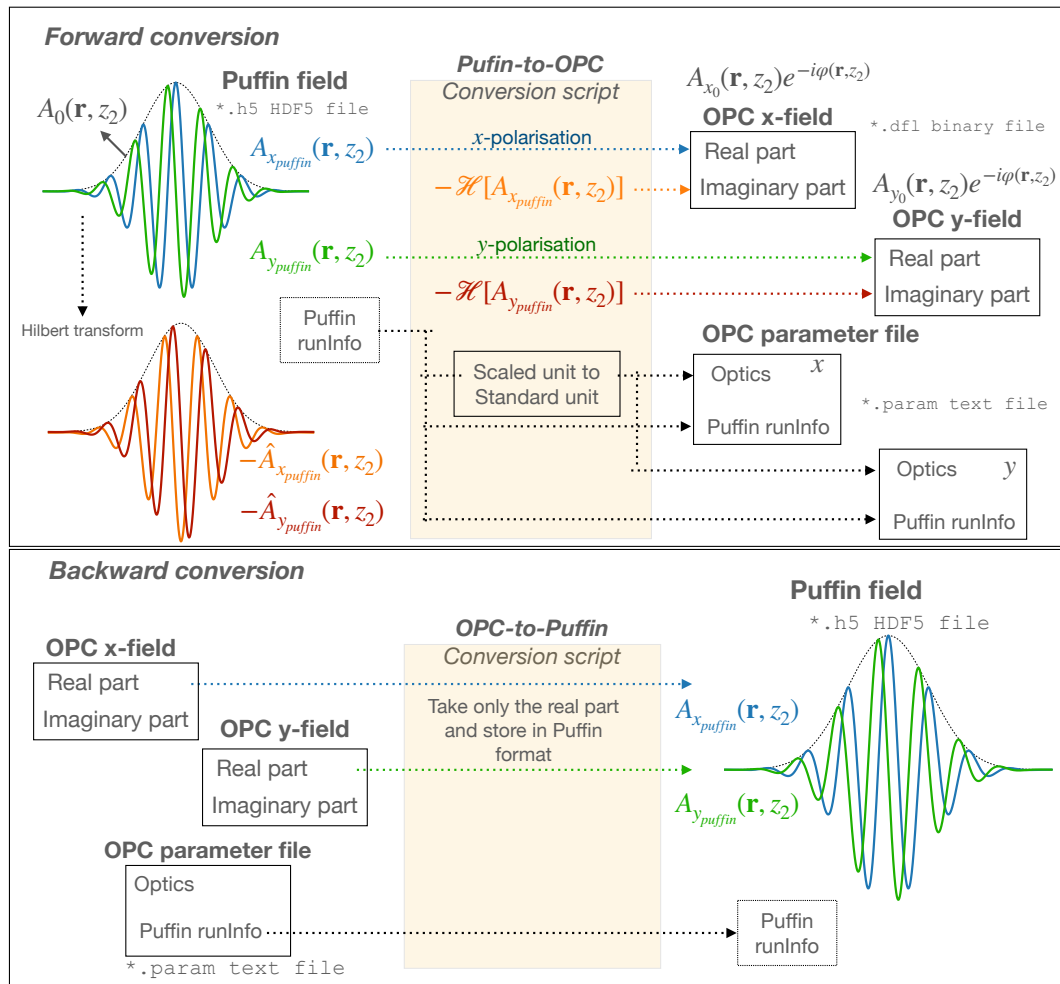


Figure 3.1: The format of the Puffin output radiation field and the conversion methods to and from the OPC radiation field format. (Top): Puffin-to-OPC and (Bottom): OPC-to-Puffin. The field conversion scripts written in python can be seen in D.

report [19] for a RAFEL functioning in the VUV spectrum. The simulation parameters are detailed in Table 3.1. The electron beam energy is 600 MeV, featuring a Gaussian energy spread of  $\sigma_E = 0.01\%$  and a peak current of  $I = 355$  A, along with a normalised beam emittance of  $\epsilon_{x,y} = 2$  mm-mrad. The transverse electron beam size, matched in the undulator with natural focusing, is given by:

$$\sigma_{x,y} = \sqrt{\frac{\epsilon_{x,y}\lambda_u}{\sqrt{2\pi}a_w}}, \quad (3.5)$$

where  $\lambda_u$  is the undulator period, and  $a_w$  is the RMS undulator parameter.

A helical undulator that is 12 m long, and consists of 200 periods with a wavelength of  $\lambda_u = 6$  cm, has an undulator parameter of  $a_w = 1.414$ . This configuration results in a resonant radiation wavelength of  $\lambda_r = 65.28$  nm and a matched transverse electron beam size of  $\sigma_{x,y} = 138$   $\mu\text{m}$ . The electron beam FEL parameter is  $\rho = 0.002487$ , and the gain length is calculated as  $l_g = \lambda_w/4\pi\rho = 1.92$  m, which corresponds to a 1D scaled length in the high gain regime of  $\bar{z} = 6.25$  [24].

The cavity length for a round trip,  $L_{cav}$ , is adjusted to correspond to the electron bunch repetition rate,  $f_{rep}$ , and is defined as:

$$L_{cav} = \frac{c}{2f_{rep}}. \quad (3.6)$$

This simulation employs a stable symmetric cavity to illustrate basic RAFEL functionality, characterised by equal radii of curvature for the mirrors, ( $R_1 = R_2 = R$ ). Here, the optical waist is situated at the cavity's centre, with the waist size defined as:

$$w_0^2 = \frac{\lambda_r}{2\pi} \sqrt{L_{cav}(2R - L_{cav})}. \quad (3.7)$$

At a position  $z$  from the cavity centre the optical beam waist size is then:

$$w(z) = w_0 \left( 1 + \left( \frac{z}{z_R} \right)^2 \right), \quad (3.8)$$

where  $z_R$  is the Rayleigh range:

$$z_R = \frac{\pi w_0^2}{\lambda_r}. \quad (3.9)$$

From equations 3.7 and 3.9, the radius of curvature of both mirrors is then:

$$R = \frac{2z_R^2}{L_{cav}} + \frac{1}{2}L_{cav}. \quad (3.10)$$

In the RAFEL cavity, the optical waist size is matched to the electron beam transverse size to obtain optimum coupling and is given by:

$$w_0 = \sqrt{2}\sigma_{x,y} \quad (3.11)$$

The RAFEL requires only a small optical feedback cavity to achieve optimal performance [24]. The configuration of the undulator and optical cavity utilised here is represented in Figure 3.2. The cavity length is defined as  $L_{cav} = 34.62$  m to synchronise with the electron pulse repetition rate of 4.33 MHz. The simulation converts the output field of Puffin from the undulator exit into its OPC format, as detailed earlier, and then it propagates through the cavity mirrors  $M_1$  and  $M_2$  back to the undulator entrance. There, it is reverted to the Puffin format to initiate the next incoming electron pulse.

The radiation initially reflects off mirror  $M_1$  with a curvature radius of  $R = 17.5$  m, as determined by Eq. 3.10, giving it a focal length of  $17.5/2 = 8.75$  m. This mirror is positioned 11.31 m away from the undulator exit, featuring a 1.0 mm diameter out-coupling hole. The second mirror,  $M_2$ , located before the undulator entrance, has the same curvature radius as  $M_1$  to create a symmetrical cavity with a concentric layout, thereby forming a stable resonator. The mirrors' reflectivity in these simulations varies between  $r = 20\%$  and  $60\%$ . Consequently, the RAFEL operation is expected to achieve saturation within relatively few cavity round-trips [24, 44].

The parameters utilised in this design provide a clear representation of how the Puffin and OPC simulation codes are integrated together. The steady-state method used for the 3D simulations incorporates periodic boundary conditions on the constant current electron beam and radiation across an integer number of radiation wavelengths. This implies that optical diffraction is included in the model, but pulse effects such as

Table 3.1: Summary of RAFEL FEL parameters used in the simulations

<b>Electron beam parameters</b>	
Electron energy (MeV)	600
Normalised emittance, $\sigma_{x,y}$ (mm mrad)	2/2
Energy spread	0.01%
Peak current (A)	355
Transverse size, $\sigma_{x,y}$ ( $\mu\text{m}$ )	138
Bunch repetition (MHz)	4.33
<b>Undulator</b>	
Undulator type	Helical
Polarisation	Circular
Undulator parameter (rms)	1.414
Pitch (cm)	6.0
Number of periods	200
<b>Oscillator</b>	
Rayleigh range (m)	1.83
Cavity length (m)	34.62
Mirror 1 radius (m)	17.5
Mirror 1 reflectivity	0.2-0.6
Out-coupling hole diameter (mm)	1.0
Mirror 2 radius (m)	17.5
Mirror 2 reflectivity	0.2-0.6
Waist position (m)	17.31
<b>FEL</b>	
Radiation wavelength (nm)	65.28
FEL parameter ( $\rho$ )	0.002487

electron pulse length, slippage, and cavity detuning are excluded. For a deeper insight into pulse effects, refer to [65], which details comprehensive 3D short-pulse simulations of an Infra-Red FEL oscillator with sub-wavelength cavity detunings.

### 3.4 Example simulation

The Puffin-OPC radiation field conversion technique mentioned above is evaluated in a straightforward steady-state RAFEL setup, as detailed by the specified parameters. The simulation employs a steady-state periodic boundary window spanning 10 radiation wavelengths and initialises from the Puffin simulation of the electron beam's shot-noise, serving as the spontaneous radiation source for the initial pass through the FEL undulator. The spontaneous radiation output from the Puffin simulation is then transformed into the OPC format as previously described. It is crucial to align the grid sizes of both codes at the start of the simulation setup. The OPC primary input file encompasses the entire optical path and the optical components, such as the mirrors

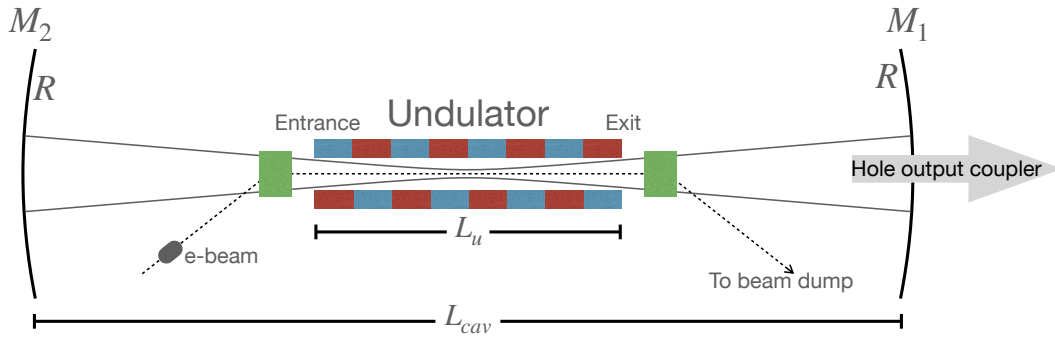


Figure 3.2: Schematic of the RAFEL used in the simulation. The cavity of length  $L_{cav}$  uses two spherical mirrors with the same radius of curvature  $R$  and of reflectivity  $r$ . The optical waist is positioned at the centre of the cavity, coincident with the centre of the FEL undulator of length  $L_u$ . The upstream mirror uses a hole for out-coupling of the radiation.

and the output coupling hole. The converted field is subsequently propagated through the optical cavity system using OPC, via free space propagation and the two mirrors  $M_1$  and  $M_2$ , back to the undulator entrance. At the undulator entrance, this field is converted from OPC format back to Puffin format and utilised as the radiation seed file in the Puffin main input file for the subsequent pass through the FEL undulator. This process iterates sequentially, as illustrated in Figure 3.3.

Figure 3.4 presents the simulation results of a 10-wavelength periodic optical field as a function of  $\bar{z}_2$  along with the scaled transverse intensities at various locations within the cavity. The use of Puffin and OPC shows that the rapid oscillations in the radiation field in  $\bar{z}_2$  are preserved. Additionally, the diffraction of radiation through the cavity-undulator system and the radiation emitted from the hole out-coupling mirror  $M_1$  are distinctly noticeable.

The RAFEL operation can be examined through the energy of the radiation pulse out-coupled from the hole, as depicted in Figure 3.5. It should be noted that the output accounts for all possible system losses, including cavity diffractive losses, mirror reflectivity losses, and out-coupling losses. The findings indicate that there is adequate optical feedback to reach saturated RAFEL operation for mirror reflectivities of  $r = 20\%$ ,  $40\%$ , and  $60\%$  for both mirrors  $M_1$  and  $M_2$ , and for the output mirror  $M_1$ 's out-coupling hole with a diameter of 1.0 mm. The RAFEL system achieves saturation

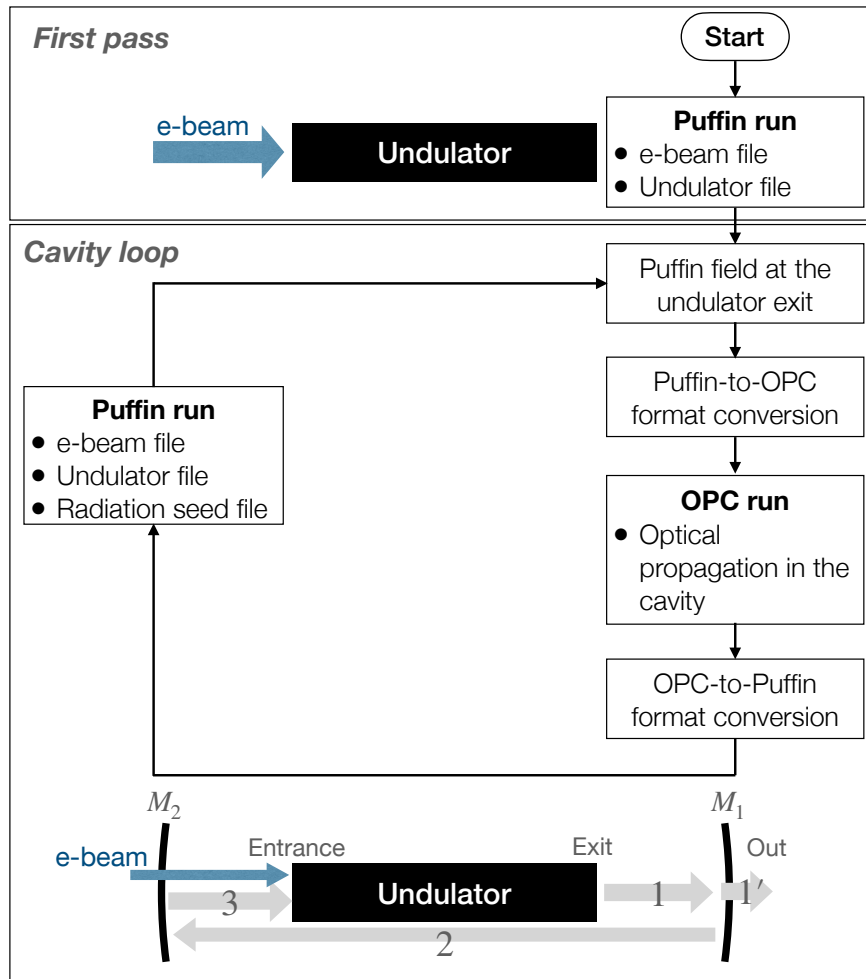


Figure 3.3: The schematic shows the flow chart of the RAFEL simulation. It begins with the first pass, Puffin to OPC conversion script, and then enters the cavity loop which is a simple Bash shell script. (1) is the radiation propagation from the undulator exit to  $M_1$  using OPC with a hole out-coupling diagnostic point (1'). (2) The OPC propagation of the reflected radiation at  $M_1$  to  $M_2$ . (3) The OPC propagation from  $M_2$  to the undulator entrance where the field is converted to Puffin format and is used as the radiation seed field for the next pass through the undulator.

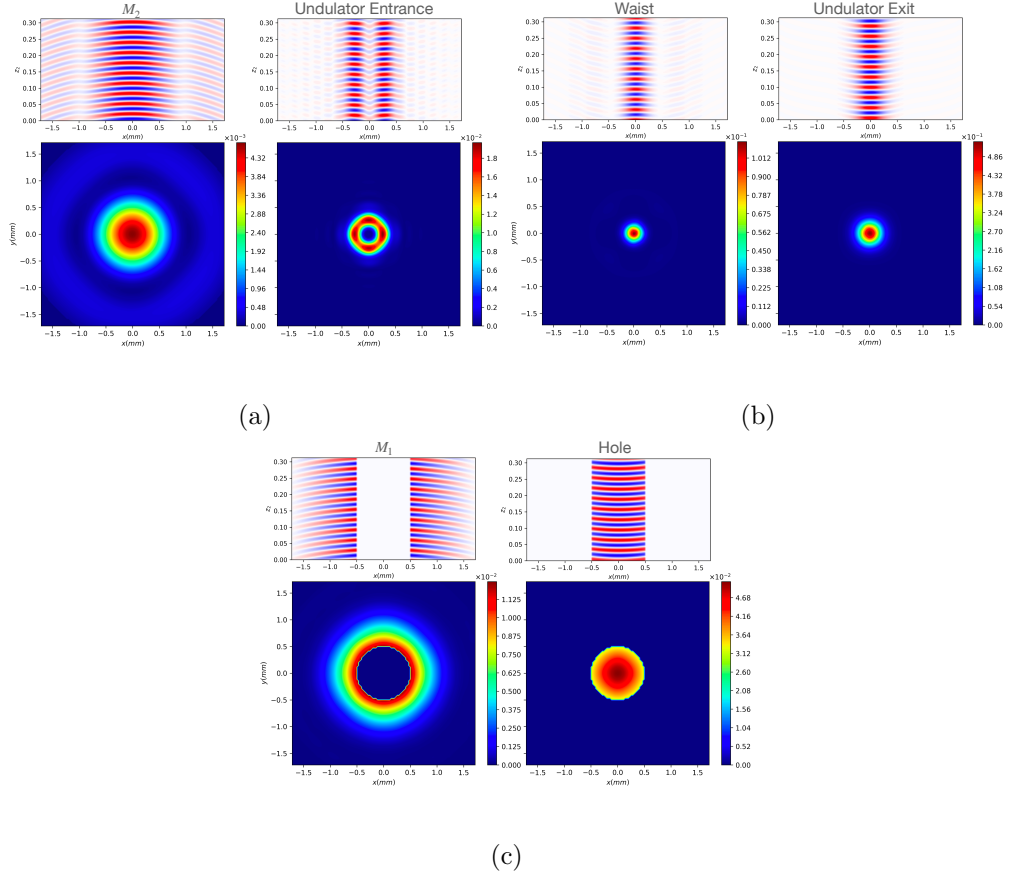


Figure 3.4: The steady-state (saturated) radiation field (top sub-plots) and the optical transverse intensity (bottom sub-plots) at different diagnostic positions for one pass through the RAFEL. The top sub-plots show the positive (red) and negative (blue) values of the electric field for the 10 wavelength periodic radiation field sample. The plots start from the mirror  $M_2$  (a-left) which is propagated by OPC to the undulator entrance (a-right) where it is translated into Puffin format as a seed field. Puffin then models the FEL interaction through the undulator waist (b-left) and to the undulator exit (b-right) where it is translated into OPC format. OPC then propagates it to mirror  $M_1$ . Part of the radiation is then transmitted through the output hole (c-right). The reflected radiation (c-left) is then propagated back to  $M_2$  and the simulation process repeats.

after approximately 5 to 15 round-trips as mirror reflectivities decrease. The similar saturated energy outputs for the higher reflectivities,  $r = 40\%$  and  $60\%$ , compared to the lower energy for  $r = 20\%$ , align with the previous findings of [44], which did not use the hole-output coupling in the cavity.

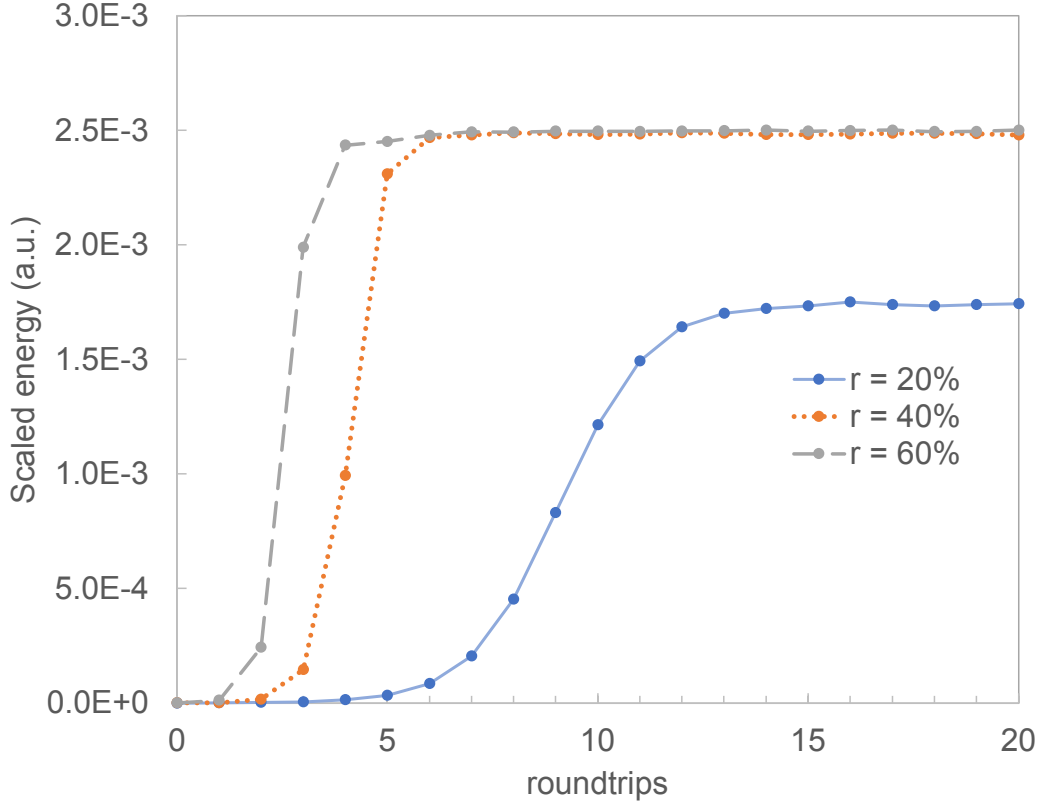


Figure 3.5: The RAFEL scaled output pulse energy, as measured at the hole out-coupling, contained within the 10 radiation wavelengths of the steady-state model, as a function of cavity round-trip number. Mirror reflectivities of  $r = 20\%$ ,  $40\%$  and  $60\%$  were used and saturation is seen to occur at around 15, 6, and 5 round-trips respectively.

### 3.5 Conclusion

The unaveraged FEL Puffin and OPC optical simulation codes can now be utilised together in FEL simulations that incorporate optical components, like a cavity-based FEL oscillator. To facilitate the transfer of the radiation field between the two simulation codes, conversion scripts have been created. This was demonstrated by modelling

a periodic mode (steady-state) model of a VUV-RAFEL design. This advancement will allow for the development of FEL models for potential future ultra short-pulse (few-wavelength), broadband simulations in cavity-based FEL designs. Additionally, other methods that require the use of unaveraged FEL and optics simulations, which have not yet been explored, should now be feasible for the first time.

## Chapter 4

# Investigating Sub-Wavelength Effects in a Free-Electron Laser Oscillator

Previous simulation studies of cavity-based free-electron lasers (FELs) used models that averaged the optical field in the FEL interaction over an integer number of radiation wavelengths. In this chapter, two unaveraged simulation codes, OPC and Puffin, are combined to enable the modelling, for the first time, of a cavity-based FEL at the sub-wavelength scale. This allows the simulation of effects such as Coherent Spontaneous Emission from the electron beam and sub-wavelength cavity length detuning. A mid-infrared cavity FEL is modelled, demonstrating that, for small sub-wavelength cavity detunings, the FEL can preferentially lase at the third harmonic of the fundamental FEL wavelength. This novel finding implies that other modes of operation might be possible, opening up cavity-based FEL operation to the exploration of additional, potentially advantageous modes of operation.

### 4.1 Introduction

FELs serve as a highly efficient, adjustable, and adaptable radiation source, covering the spectrum from microwaves to hard X-rays, thus offering extensive current and

potential applications in both science and industry. FELs may function as a high-gain, single-pass amplifier or in a lower-gain oscillator mode, which necessitates placing the FEL undulator inside a cavity to provide radiation feedback.

This study focuses on the FEL oscillator mode of operation. Several factors affect the performance of these FELs, including the design of the cavity resonator, the properties of the electron beam, and the undulator. The length of the cavity resonator, which is the distance between its mirrors, is a crucial parameter that must be adjusted to ensure that the radiation emitted by one electron pulse overlaps with the next electron pulse entering the FEL undulator. When the round-trip time of a radiation pulse within the cavity matches the difference in arrival times between electron pulses, the cavity is considered resonant. The cavity length can be ‘detuned’ from this resonant length to modify and enhance radiation output for specific uses.

A significant benefit of cavity detuning is that it can be integrated into current FEL facilities without requiring major modifications. Furthermore, the cavity length can be modified dynamically in real-time during FEL operation, offering enhanced control over output characteristics such as intensity and efficiency, thus allowing its performance to be fine-tuned for particular applications [81].

In this chapter, we employ unaveraged simulations to explore, for the first time, the impacts of cavity detuning at a sub-wavelength scale in an FEL oscillator. This study demands a sub-wavelength resolution of the radiation/electron FEL interaction, which is beyond the capabilities of averaged computational models that average the FEL interaction over an integer number of radiation wavelengths. When modelling short pulses, the simulation accounts for both the coherent and shot-noise spontaneous emission of the electron beam [38]. Coherent Spontaneous Emission (CSE) has the potential to dominate the initial amplification in an FEL undulator, particularly in the low-gain operating regime of FELs [43]. CSE is primarily triggered by a short electron pulse with a fine current structure at the wavelength level, such as a rectangular beam current with ‘sharp edges’. Thus, a more comprehensive understanding of these sub-wavelength phenomena is essential, especially for short-pulse FEL oscillators. Here, we present a preliminary investigation in the mid-IR wavelength region of the spectrum.

The unaveraged FEL simulation software Puffin [14, 16] (accessible from [15]), and the Optical Propagation Code (OPC) [32, 76] (accessible from [31]), were earlier integrated to simulate a Regenerative Amplifier FEL (RAFEL) oscillator [64] within the steady-state operational area, applying periodic boundary conditions to the electron-radiation interaction, thus eliminating all pulse effects, including CSE. By employing the combined Puffin-OPC simulation in pulsed mode, it is possible to model wide-bandwidth and sub-wavelength phenomena, such as harmonic radiation generation, CSE, and sub-wavelength cavity detuning. Consequently, it leads to a comprehensive, 3D unaveraged computational representation of a short-pulse FEL oscillator, with its initial findings presented here for the first time.

This study explores various impacts of sub-wavelength cavity detuning on the performance of FEL, with a specific focus on its influence on harmonic generation within the FEL oscillator. The initial demonstration of generating radiation at the third harmonic of the fundamental resonant wavelength in an FEL was achieved by inserting a dispersive material into the FEL oscillator cavity. This modification altered the round-trip transit times of the fundamental and third harmonic pulses in the cavity [8].

The simulation outcomes presented herein, utilising both a ‘sharp’ rectangular electron beam current profile and a ‘smooth’ Gaussian-profiled electron beam, consistently indicate that cavity detuning on a sub-radiation wavelength scale can elevate harmonic radiation output beyond that of the fundamental mode, thereby achieving harmonic lasing without the necessity for any dispersive materials. These results propose that harmonic lasing arises due to sub-wavelength cavity detuning and not solely from CSE generated by a sharp-edged beam current. A mid-infrared FEL oscillator is simulated to showcase this innovative mode of FEL operation.

## 4.2 Simulation model

### 4.2.1 FEL and optics code

Chapter 2 provides a summary of the unaveraged simulation approach for FEL oscillators. This approach employs two simulation codes, Puffin and OPC, which simulate the

interaction of electrons with radiation in the FEL undulator and the transmission of the resulting radiation field through the oscillator cavity, respectively. Puffin is an un-averaged FEL simulation code that models the interaction between electrons and light within an undulator. After the Puffin FEL simulation, the output field at the undulator's exit is converted into the OPC code format. OPC then simulates the propagation of the radiation field through the optical oscillator cavity, including the mirrors and various optical components. The two codes are executed one after the other, starting with Puffin's simulation of the FEL interaction. The OPC simulation of the radiation's propagation through the oscillator cavity then allows for adjustments in the optical path length due to cavity detuning. After the radiation field is propagated back to the undulator entrance via OPC, it is transformed back into a format that serves as the input seed field for the next iteration through Puffin. This iterative process, pass-by-pass, ensures a precise simulation of the FEL interaction and the radiation field's propagation through the optical components of the oscillator cavity.

#### 4.2.2 Simulation parameters

In the demonstrated example, the parameters listed in Table 4.1 are almost identical to those used in the one-dimensional IR-FEL simulations described in [27], with the inclusion of additional optics and beam parameters necessary for the three-dimensional modelling. A curved-pole undulator focussing mechanism is implemented to ensure that the transverse electron beam size remains constant throughout the length of the undulator [30, 70]. The undulator module, which is 1.8 m long, comprises 40 periods with a wavelength of  $\lambda_u = 4.5$  cm. The transverse electron beam size in the undulator focusing is calculated as  $\sigma_{x,y} = (\epsilon_{x,y}\lambda_u/(\sqrt{2\pi}a_w))^{1/2}$ , where  $\epsilon_{x,y}$  is the normalised emittance of the beam,  $\lambda_u$  is the period of the undulator, and  $a_w$  is the RMS undulator parameter, resulting in  $\sigma_{x,y} = 311.8 \mu\text{m}$ . The temporal profile of each electron pulse's current in the beam is rectangular with a duration of 400 fs. The mean energy of the electron beam is denoted by  $\gamma$  in units of  $m_e c^2$ , leading to a resonant radiation wavelength of  $\lambda_r = \lambda_u(1 + a_w^2)/2\gamma^2 \approx 6 \mu\text{m}$  in the mid-infrared range. Consequently, each electron pulse in the beam has a length of  $20\lambda_r$ . To satisfy the resonant cavity

condition, the time interval between two consecutive electron pulses must align with the cavity's round-trip time, such that  $c/f_{\text{rep}} = 2L_{\text{cav}}$ , where  $f_{\text{rep}}$  is the electron pulse repetition rate, and  $L_{\text{cav}}$  is the cavity length between the two mirrors.

Table 4.1: Summary of FEL oscillator parameters used in the simulations

<b>Electron beam parameters</b>		Rectangular	Gaussian
Electron energy (MeV)	50		
Bunch charge (pC)	100		
Normalised emittance, $\sigma_{x,y}$ (mm mrad)	12/12		
Energy spread	0.5%		
Bunch length (fs)		400	470 (FWHM)
Peak current (A)		250	200
Transverse size, $\sigma_{x,y}$ ( $\mu\text{m}$ )	311.8		
Bunch repetition (MHz)	10		
<b>Undulator</b>			
Undulator type	Curved pole		
Polarisation	Linear		
Undulator parameter (rms)	1.25		
Pitch (cm)	4.5		
Number of periods	40		
<b>Oscillator</b>			
Rayleigh range (m)	0.52		
Cavity length (m)	14.9896		
Mirror 1 radius (m)	9.00024		
Mirror 1 reflectivity	0.960		
Mirror 2 radius (m)	6.064		
Mirror 2 reflectivity	0.999		
Waist position (m)	6.02		
<b>FEL</b>			
Radiation wavelength ( $\mu\text{m}$ )	6.0		
FEL parameter ( $\rho$ )	0.0052		

The 2-mirror optical cavity is configured as a nearly concentric resonator with a Rayleigh range of 52 cm, as depicted in Figure (4.1). The first mirror  $M_1$ , which can be either partially transmissive or utilise a hole for out-coupling, is positioned just after the undulator's exit. The second mirror  $M_2$ , completing the simple cavity, is positioned just before the entrance of the undulator. When the spacing between the two mirrors results in a round-trip propagation time that matches the electron beam's repetition rate, the cavity achieves zero length detuning. The optical beam waist is located at the midpoint of the undulator, with the Rayleigh range being roughly one-third of the undulator's length.

The propagation of radiation within the optical cavity is simulated using the OPC code [32, 76]. The selection of the radiation propagation method in the code, among

other factors, critically influences the simulation's accuracy. In OPC, three propagation methods can be implemented: the spectral method, Fresnel diffraction integrals, and modified Fresnel integrals. Of these, the spectral method and Fresnel diffraction integrals are numerically solvable using Fast Fourier Transforms (FFTs). On the other hand, the modified Fresnel integral, although producing valuable results, is the least efficient method [32]. Nevertheless, it offers a promising alternative by enabling the propagation of an optical beam through a complex optical system in a single step. An essential requirement for using this method is that all optical components must be precisely described by an ABCD matrix [69]. Moreover, the scaling applied to this method permits the use of a magnification factor for the grid, allowing different transverse mesh sizes at the Puffin input and the cavity mirror output planes.

In this research, the oscillator's waist is positioned at the centre of the undulator, allowing the FEL output to travel approximately 7.1 metres from the undulator exit to the first mirror,  $M_1$ , within the resonant cavity's length. Diffraction causes considerable variations in the size of the transverse optical beam, ranging from about  $1 \text{ cm}^2$  to roughly  $100 \text{ cm}^2$ . This is modelled using the OPC modified Fresnel integral algorithm to expand the optical nodes' transverse dimensions by a factor of 10. For the round-trip OPC oscillator simulation to be completed, the reflected optical beam from  $M_1$  is then directed to  $M_2$ , and subsequently back to the undulator entrance. There, the size of the transverse node is reduced by a factor of 10 and converted to the Puffin input format, before proceeding with the next pass through the Puffin FEL simulation.

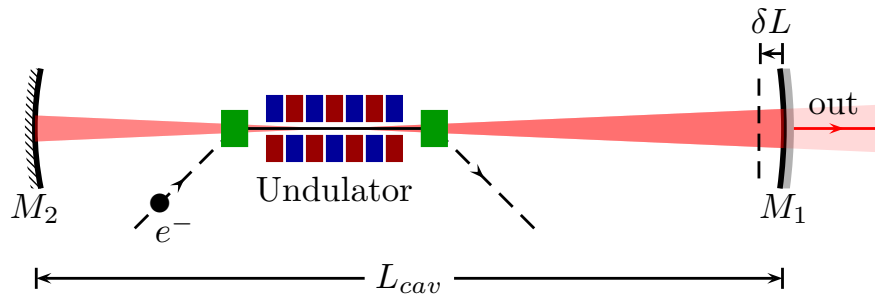


Figure 4.1: Schematic of the FEL oscillator as used in the simulation. The cavity, formed by the two mirrors  $M_1$  and  $M_2$ , can be changed in length by the cavity detuning parameter  $\delta L$ . This adjusts the synchronisation between the electron pulse arrival times and the radiation round-trip time in the cavity which are synchronous when  $\delta L = 0$ .

## 4.3 Simulation results

### 4.3.1 Empty cavity

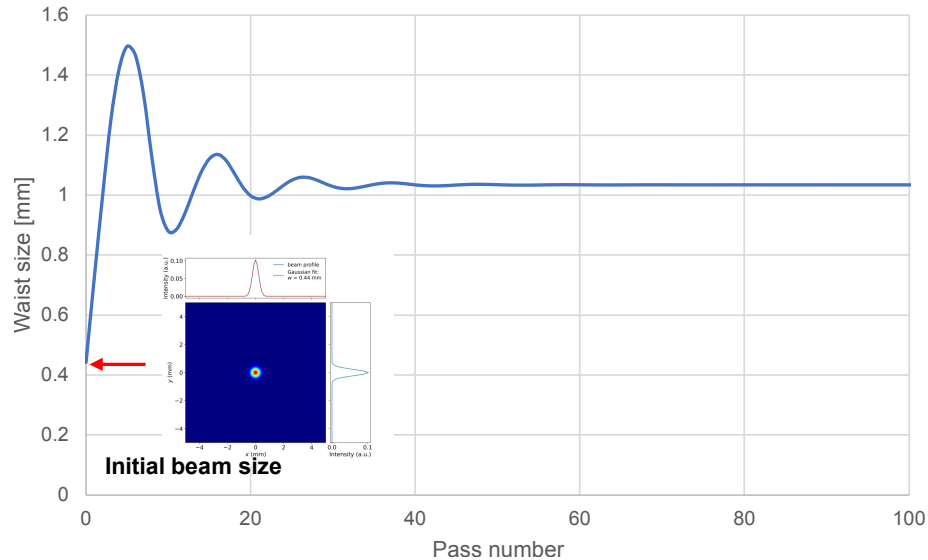


Figure 4.2: Evolution of the beam waist size as a function of the pass number in a FEL oscillator. The beam waist size starts from an initial value of approximately 0.4 mm (indicated by the red arrow) and stabilises over time. The inset shows the initial beam profile with a Gaussian fit.

The examination of an empty cavity, without an undulator, is essential to validate the functionality of the Gaussian mode in the FEL cavity, as the beam spreads due to diffraction. To start this procedure, the Gaussian optical beam is initialised using Puffin with a starting beam waist of 0.4 mm and then transmitted through the OPC for several round-trips until stability is reached. This method guarantees that the cavity layout is suitable for containing the optical beam within the initial region of the undulator, thus enhancing the alignment with the electron beam.

Figure 4.2 illustrates the change in waist size relative to the number of round-trips (pass number). The waist size of the beam initially measures around 0.4 mm (highlighted by the red arrow) and shows oscillatory behaviour before reaching a stable state. The inset plot zooms in on the initial beam profile, featuring a Gaussian fit with a waist size of 0.44 mm. The main plot represents the dynamics of the beam size as it

traverses the cavity multiple times, eventually settling at the intended beam waist of approximately 1.0 mm.

### 4.3.2 Gain lethargy

The simulation techniques and parameters specified in Section (4.2) are now used to model the FEL oscillator. Figure 4.3a illustrates the initial position of the rectangular current electron pulse at the start of the undulator, along with the development of the radiation power and phase during the first pass through the cavity. The trailing edge of the electron pulse produces a CSE wavefront at a temporal position of  $(ct - z)/\lambda_r = 20$  as it passes through the undulator at a speed lower than  $c$ . The CSE generated by the rectangular current profile electron pulse propagates vertically at a temporal position of 20 wavelengths in the Figure 4.3a and exhibits greater power compared to the spontaneous power resulting from shot-noise.

Near the end of the undulator, an increase in radiation is observed towards the back of the window, where the electrons are more tightly bunched as a result of the FEL interaction and emit more intensely. Consequently, the centroid of the optical pulse (at  $(ct - z)/\lambda_r \approx 50$  and phase  $\approx 0$ ) moves slower than the speed of light. The centroid of the optical pulse is subsequently delayed with each pass of the electron pulse through a resonant cavity, where  $\delta L = 0$ , leading to a gradual decoupling of the optical pulse from the electron beam over successive passes within the cavity.

The evolution of the FEL scaled power and phase as a function of the cavity round-trip number, depicted in Figure 4.3b, illustrates that the peak power travels at a velocity slower than  $c$ , known as ‘gain lethargy’. Beginning from the first passage through the cavity, the pulse experiences amplification, attaining its maximum energy at approximately the 20th pass, before gradually reducing until it separates from the electrons around the 80th pass. This pattern of radiation pulse evolution for a zero cavity detuning case,  $\delta L = 0$ , corresponds with the theoretical model of short pulse evolution in a FEL oscillator [21].

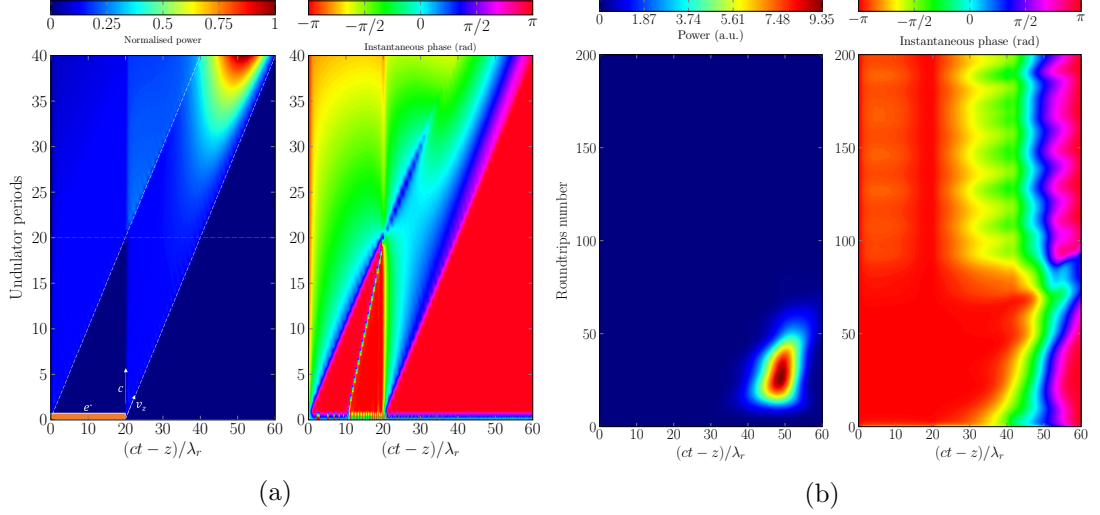


Figure 4.3: (a) Contour plot of the normalised FEL power evolution (left) and phase (right) as the electron pulse propagates through the undulator during the first pass through the oscillator. The plot is in a window travelling at the speed of light, so that the electron beam of length  $20\lambda_r$  (initially bottom left) moves left-to-right in the radiation window frame as it propagates through the undulator, as shown by the white dashed lines. The radiation power starts from both electron beam shot-noise and Coherent Spontaneous Emission. (b) Contour plot of the scaled FEL power  $\bar{P}$  evolution as a function of the number of round-trips within the oscillator cavity for zero cavity detuning,  $\delta L = 0$ . It is seen that the radiation pulse power drifts from left to right in the window between increasing round-trip number 10 - 50, indicating that its net velocity is less than the speed of light. This causes a slow decoupling with the electron pulse after each round trip and the radiation power is seen to decrease after round trip  $\sim 25$ .

### 4.3.3 Sub-wavelength cavity detuning

Cavity detuning serves to synchronise the timing between the optical pulse and the electron bunch within an undulator, mitigating the delay induced by gain lethargy in FEL oscillators [1, 21]. By reducing the cavity length, the optical pulse reaches the electron bunch sooner, reducing gain lethargy and enhancing the FEL interaction performance. Furthermore, this cavity shortening offers additional control over the temporal properties of the FEL pulse. The cavity detuning diagram in the FEL oscillator is shown in Figure 4.4, illustrating the position of the radiation feedback relative to the fresh electron beam during the subsequent pass.

In this research, a positive cavity detuning,  $\delta L > 0$ , indicates a reduction in cavity length, as illustrated in Figure 4.1. Consequently, the light pulse covers a shorter distance of  $2\delta L$  during each round-trip. The Puffin code, which does not average out the FEL field, permits sub-wavelength adjustments to the cavity detuning with a minimum resolution equivalent to the spacing between adjacent nodes of the radiation field sampling. Using Puffin, 21 nodes are employed to sample each radiation wavelength, allowing  $\delta L$  to be altered in steps of  $0.05\lambda_r$ , resulting in a change of  $2\delta L = 0.1\lambda_r$  for the round-trip distance of the radiation from the cavity. Thus, the cavity detuning can be finely tuned in small, sub-wavelength steps, facilitating the investigation of the effects of such precise cavity detuning adjustments on the FEL output.

The oscillator model employs Puffin scaled units [14, 16], where  $\rho$  represents the FEL parameter. The expression for the scaled pulse energy is given by:

$$\bar{\epsilon} = \int \bar{P} d\bar{z}_2, \quad (4.1)$$

where  $\bar{P}$  is the scaled power from Puffin (see Figure 4.3),  $\bar{z}_2$  is the temporal scaling parameter given by  $\bar{z}_2 = (ct - z)/l_c$ , and  $l_c = \lambda_r/(4\pi\rho)$  is the cooperation length. Note that the radiation power is related to the scaled power from Puffin via:

$$P = s_p \bar{P}, \quad (4.2)$$

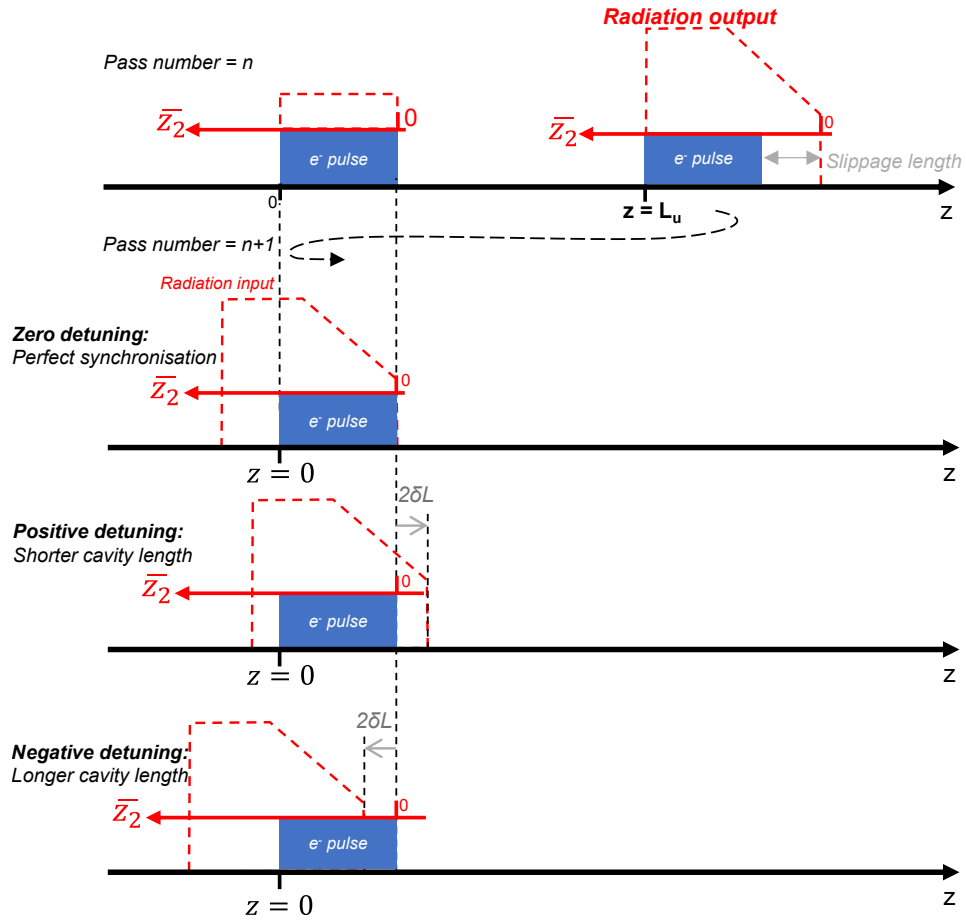


Figure 4.4: The figure illustrates the effects of cavity detuning on the synchronisation between the electron pulse and the radiation field in an FEL oscillator in the radiation frame of reference  $\bar{z}_2$  as the radiation propagate from left to right on  $z$  axis. **Zero detuning:** This represents perfect synchronisation where the radiation cavity length matches the electron repetition rate. **Positive detuning:** Here, the length of the cavity is shorter than the ideal length, causing the radiation field to move forward relative to the electron pulse. **Negative detuning:** In this scenario, the cavity length is longer than the ideal, causing the radiation field to slide backward relative to the electron pulse.

where

$$s_p = l_g l_c c \epsilon_0 \left( \frac{\gamma m_e c^2}{e \kappa l_g} \right)^2, \quad (4.3)$$

$$\kappa = \frac{a_w}{2\rho\gamma}, \quad (4.4)$$

and  $l_g = \lambda_w / (4\pi\rho)$  is the gain length.

The pulse energy is then:

$$\varepsilon = \frac{1}{c} s_p l_c \bar{\varepsilon}. \quad (4.5)$$

For example in Figure 4.5, a scaled pulse energy of  $\bar{\varepsilon} = 10$  corresponds to a real pulse energy of  $\varepsilon \sim 0.9$  mJ.

The scaled pulse energy  $\bar{\varepsilon}$  is plotted in Figure 4.5 against the number of cavity round-trips, considering a range of cavity sub-wavelength detunings from resonance,  $\delta L = 0$ , and an output mirror reflectivity of  $R = 0.96$ . The detuning range of  $0 \leq 2\delta L < 0.5$  is illustrated in Figure 4.5a), where it can be observed that, for smaller cavity detunings  $2\delta L = 0.0 - 0.3\lambda_r$ , the scaled pulse energy  $\bar{\varepsilon}$  initially increases but then decreases for round trips  $0 - 100$ , influenced by the lethargy effect. For  $2\delta L = 0.2$  and  $0.3\lambda_r$ , the pulse energy increases again after exceeding about 200 round trips, eventually reaching steady-state behaviour for round-trip numbers  $> 400$ . Note that steady-state behaviour occurs for fewer round trips ( $< 100$ ) with increasing cavity detuning, as depicted in Figure 4.5b). For  $2\delta L > 1.0\lambda_r$ , the steady-state is achieved in fewer round-trips ( $< 50$ ) because the FEL gain initially occurs toward the front of the electron pulse more quickly than for smaller detunings. After saturation, the pulse energy exhibits limit-cycle behaviour [5], with an oscillation frequency dependent on the detuning of the cavity, as noted in [34].

The steady-state post-saturation pulse energies as a function of cavity detuning, depicted in Figure 4.5 (a & b), are summarised in Figure 4.5c. The cases for output mirror  $M_1$  reflectivities of  $R = 0.6, 0.5$ , and  $0.4$  are also illustrated, with optimal cavity detunings occurring at  $2\delta L \approx 2\lambda_r, 2.5\lambda_r$ , and  $4\lambda_r$ , respectively. This indicates that as mirror reflectivity decreases, the optimal detuning of steady-state pulse energy shifts to larger values, consistent with the analytical model of [51]. Although only intracavity behaviour is shown here using the scaled FEL power from the undulator

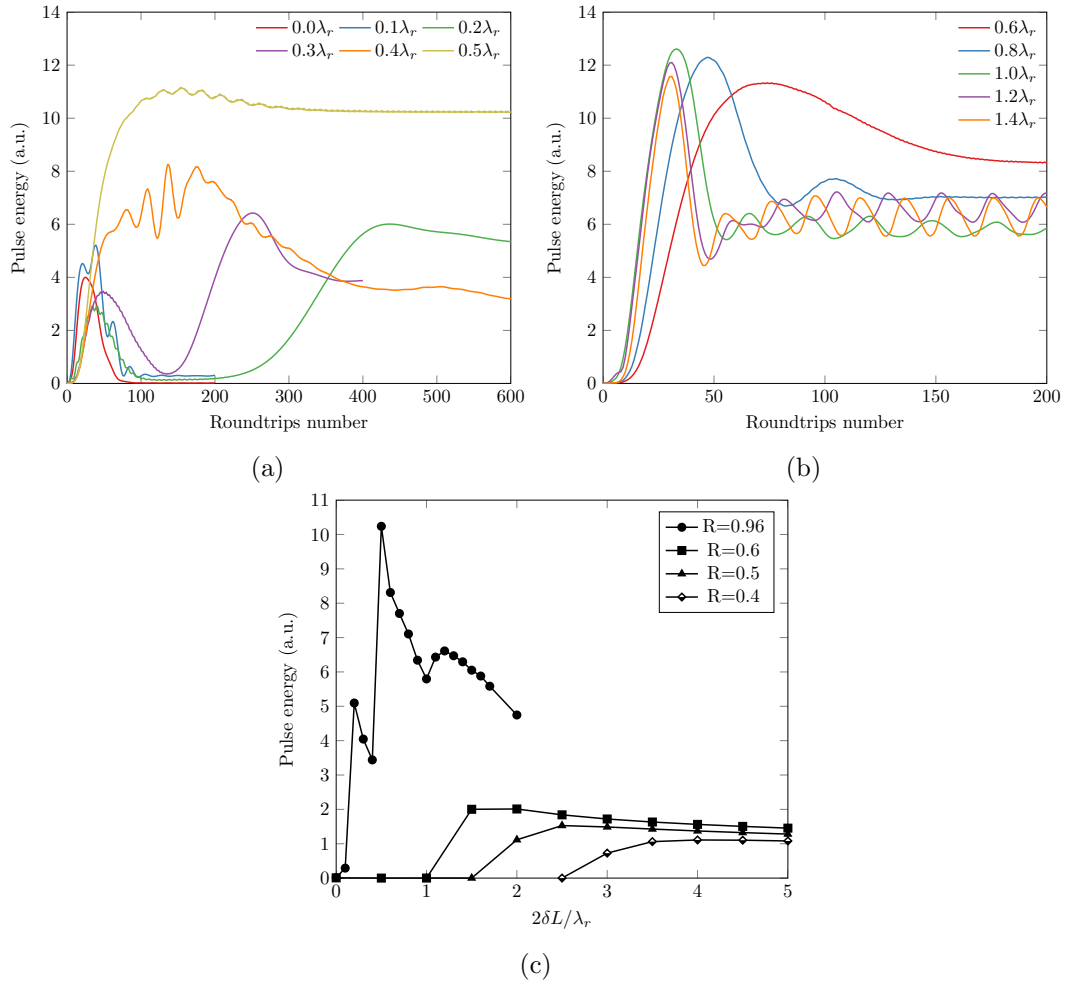


Figure 4.5: Radiation scaled pulse energy  $\bar{\epsilon}$  as the function of roundtrip number for a range of sub-wavelength cavity detunings: (a)  $0.0 < 2\delta L < 0.5\lambda_r$  and (b)  $0.6 < 2\delta L < 1.4\lambda_r$  for the case of cavity mirror  $M_1$  reflectivity of  $R = 0.96$ . Note different horizontal scales. (c) Steady-state (saturated) scaled pulse energy  $\bar{\epsilon}$  at the undulator exit from Puffin-OPC simulation Vs cavity detuning  $2\delta L$  in units of radiation wavelengths for a total reflectivity  $R = 0.96$ . The additional plots are for cavity reflectivities of  $R = 0.6, 0.5$ , and  $0.4$ .

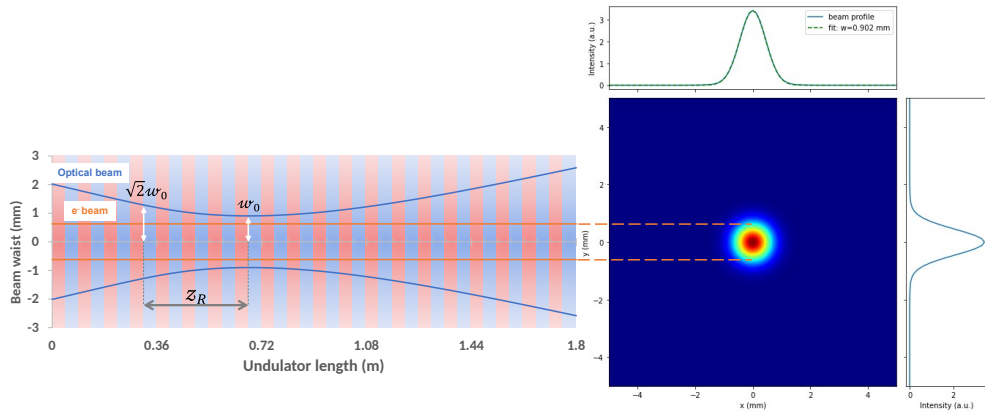


Figure 4.6: Evolution of the beam waist as it propagates through the undulator. The left plot shows the beam waist size in relation to the undulator length, highlighting the optical beam (blue) and the electron beam (orange). The right plot shows the beam profile at the waist position, with a Gaussian fit indicating a waist size of 0.902 mm.

exit, all subsequent optical cavity effects, such as diffraction and out-coupling losses, can be modelled.

Figure 4.6 offers an extra depiction of how the beam waist evolves as it traverses the undulator, specifically for the optimal condition of  $2\delta L = 0.5\lambda_r$  in steady state beyond the round-trip number  $> 400$ . The graph on the left shows the relative size of the beam waist along the undulator's length, distinguishing the optical (blue) and electron (orange) beams. At the centre of the undulator, the optical beam waist hits a minimum ( $w_0$ ), then expands symmetrically, showcasing a Gaussian beam profile. The Rayleigh range ( $z_R$ ) is marked, indicating the distance over which the waist size increases by a factor of  $\sqrt{2}$ . The graph on the right presents the beam profile at the waist position, with a Gaussian fit indicating a waist size of 0.902 mm. The inset graph provides a detailed view of the beam intensity distribution along with its cross-sections, confirming the Gaussian nature of the beam profile. Although the waist position is not centred within the undulator as designed, this could be attributed to the FEL interaction and the length of the cavity detuning.

#### 4.3.4 Steady-state gain

The steady-state gain is expressed as:

$$G = \frac{P_G - P_0}{P_0}, \quad (4.6)$$

where  $P_0$  is the peak radiation power measured at the entrance of the undulator, and  $P_G$  represents the peak intracavity radiation power at the undulator exit. Assuming that the out-coupling is achieved through a partially transmissive mirror with reflectivity  $R$ , the out-coupling power can be expressed as:

$$P_{\text{out}} = (1 - R)P_G. \quad (4.7)$$

In this simulation,  $P_G$  is derived from the Puffin output file, while  $P_0$  is calculated after cavity propagation using OPC. Consequently,  $P_0$  integrates all cavity effects during the propagation from the undulator exit to the cavity mirrors and back to the undulator entrance, and can be depicted as  $P_0 = (1 - \alpha)P_G$ , where  $\alpha$  denotes the total cavity losses. In the steady-state condition, the gain will balance these total losses. The extraction efficiency  $\eta = P_{\text{out}}/P_e$ , where  $P_e = \gamma mc^2 I_b/e$  is the peak electron beam power approximately  $\sim 12.5$  GW.

In Figure 4.7, the steady-state peak power gain  $G_p$  and the mean energy gain  $G_\epsilon$  (4.7a), the FWHM pulse duration measured in units of  $\lambda_r$ , the FEL beam waist at the undulator exit in millimeters (4.7b), and the extraction efficiencies for the peak ( $\eta_p$ ) and the mean energy ( $\eta_\epsilon$ ) (4.7c) are depicted. For a cavity detuning of  $2\delta L/\lambda_r = 0.2$ , where lasing occurs at the third harmonic, the steady-state loss is observed to balance the gain at approximately 10%. This value exceeds the total mirror reflectivity loss of around 4%, attributed to diffractive losses in the cavity mirrors. When the cavity detuning  $2\delta L/\lambda_r > 0.5$ , lasing occurs at the fundamental frequency. Here, diffractive losses are larger because of the longer fundamental wavelength, resulting in an increased beam radius at the undulator's end, as illustrated in Figure 4.7b. However, the gain for the fundamental is higher and compensates for these diffractive losses, as shown in Figure 4.7a.

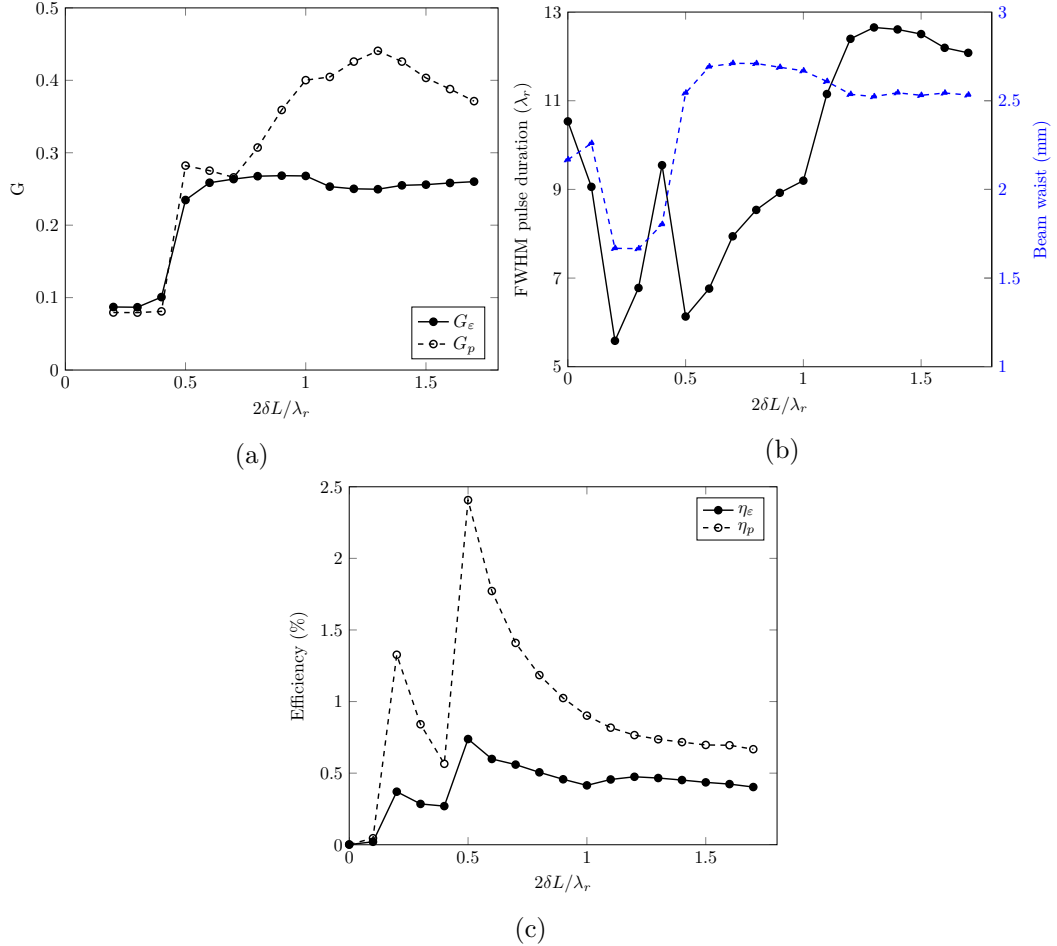


Figure 4.7: The plot illustrates the results from Puffin-OPC simulations in relation to cavity detuning  $2\delta L$  for a total reflectivity of  $R = 0.96$ . The calculated values shown include (a) peak and mean gains  $G_p$ ,  $G_\varepsilon$ , (b) full-width at half maximum (FWHM) FEL pulse duration (solid line), FEL beam waist at the undulator exit (dashed blue line), and (c) extraction efficiency. In (a & c), the peak pulse powers are represented by the dashed line, while those for the mean pulse energy are represented by the solid line. Note that for the gains of (a), cavity detunings  $2\delta L = 0$  and  $0.1$  are not plotted due to the very limited lasing, as seen from the efficiencies plotted in (c), leading to a noisy value.

### 4.3.5 Third-harmonic generation

Figure 4.5c shows a departure in saturation energies as a function of cavity detuning from previous studies, such as those by [34], for the  $R = 0.96$  case and for small, sub-wavelength cavity detunings  $2\delta L/\lambda_r < 1$ . Specifically, there are two peaks in the saturated pulse energy around  $2\delta L/\lambda_r = 0.2$  and  $0.5$ . To better understand this behaviour, it is beneficial to examine how the radiation field and spectral components of the FEL output pulse power for the  $2\delta L = 0.2$  case progress with cavity pass number, as illustrated in Figure 4.8. It demonstrates that, although the fundamental frequency growth  $\omega/\omega_r = 1$  initially dominates, the third harmonic growth becomes predominant in the steady state at higher pass numbers.

The effect of this behaviour is illustrated more clearly in Figure 4.9, which shows the scaled spectral pulse energies for three different cavity detunings. In the  $2\delta L = 0.2\lambda_r$  case depicted in Figure 4.8, it can be seen that the pulse energy at the fundamental frequency (solid line) initially gains more rapidly and peaks after about 40 roundtrips. Following this, its gain gradually decreases because of gain lethargy at the fundamental frequency, coupled with insufficient cavity detuning to offset it. Conversely, this particular cavity detuning permits the pulse energy at the third harmonic (dashed line) to be amplified over numerous round-trips, as depicted in the contour plots of the instantaneous pulse power and phase over an increasing number of cavity roundtrips. The evolution of the pulse phase contour reveals that the amplification of the third-harmonic pulse starts to dominate after approximately 100 passes, as the fundamental frequency declines due to lethargy. Thereafter, the third-harmonic pulse continues its amplification until it reaches a steady-state saturation beyond 700 passes. Figure 4.9 represents the progression of the fundamental and third-harmonic for cavity detunings at  $2\delta L = 0.3\lambda_r$  and  $0.4\lambda_r$ . The fundamental pulse energy increases as the cavity detuning becomes larger. Expanding the cavity detuning values to  $2\delta L = 0.6\lambda_r$ ,  $0.9\lambda_r$ , and  $1.2\lambda_r$ , as illustrated in Figure 4.10, reveals that the fundamental harmonic starts to dominate the evolution, consistent with the findings of [34].

In addition to simulations performed with a rectangular electron beam current profile, which produces significant CSE powers exceeding spontaneous emission due to

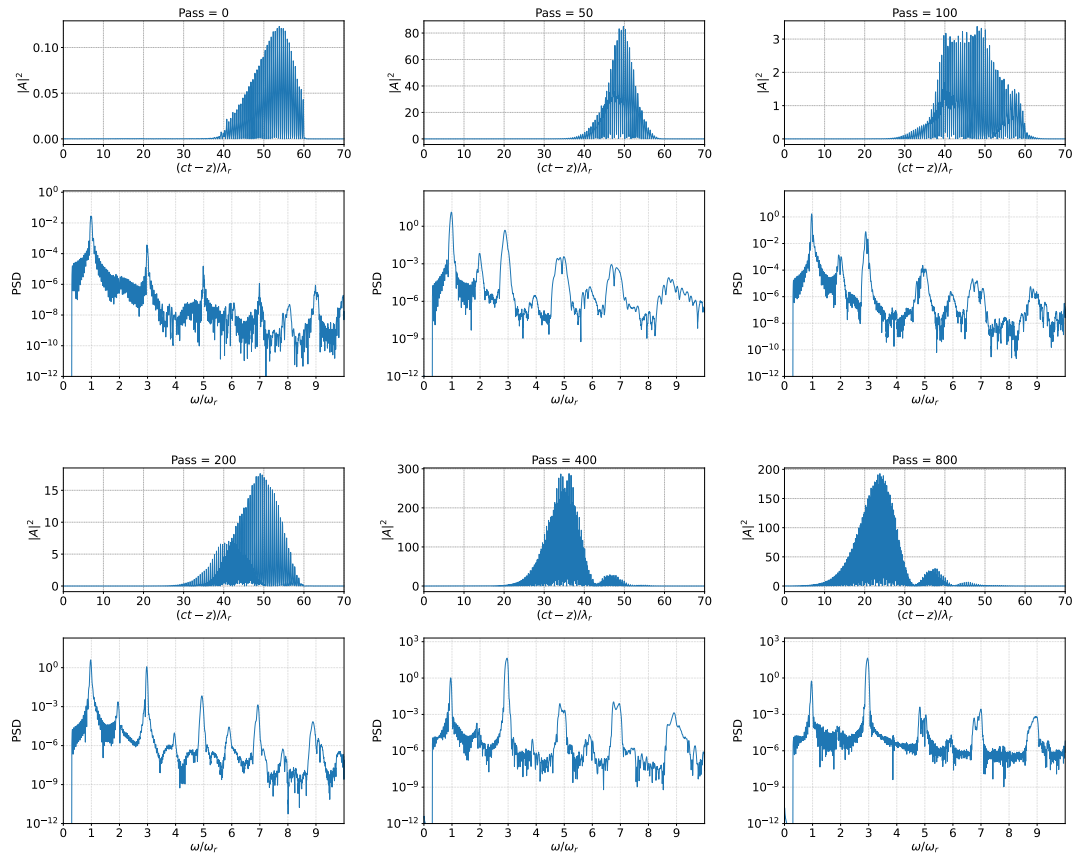


Figure 4.8: The temporal, scaled power profiles,  $|A|^2$ , at the undulator exit for the central transverse node of the Puffin output field, corresponding to the midpoint of the 2D transverse grid along the temporal axis, and its corresponding power spectral density (PSD), for different pass numbers through the cavity for a cavity detuning of  $2\delta L = 0.2\lambda_r$ . It can be seen that, while there is initial growth of the fundamental  $\omega/\omega_r \approx 1$ , the third harmonic  $\omega/\omega_r \approx 3$  evolves to dominate at larger pass numbers into the steady state.

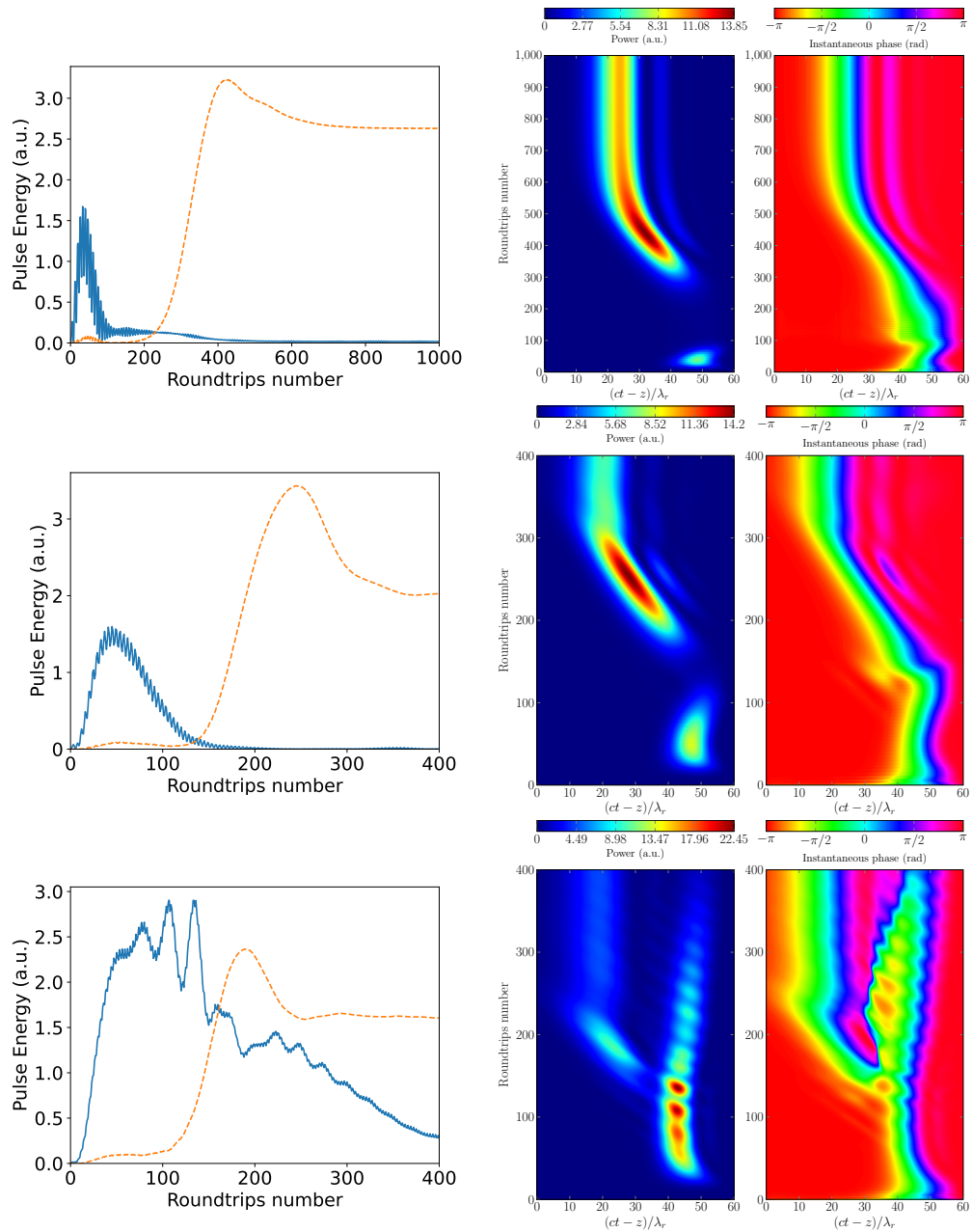


Figure 4.9: (Left) The fundamental (solid blue) and third harmonic (dashed orange) spectral pulse energy evolution as the function of cavity roundtrip number for cavity detunings of (top to bottom)  $2\delta L = 0.2\lambda_r$ ,  $2\delta L = 0.3\lambda_r$ , and  $2\delta L = 0.4\lambda_r$ . (Right) Contour plot of the FEL pulse power and phase evolution over multiple passes for the corresponding cavity detunings.

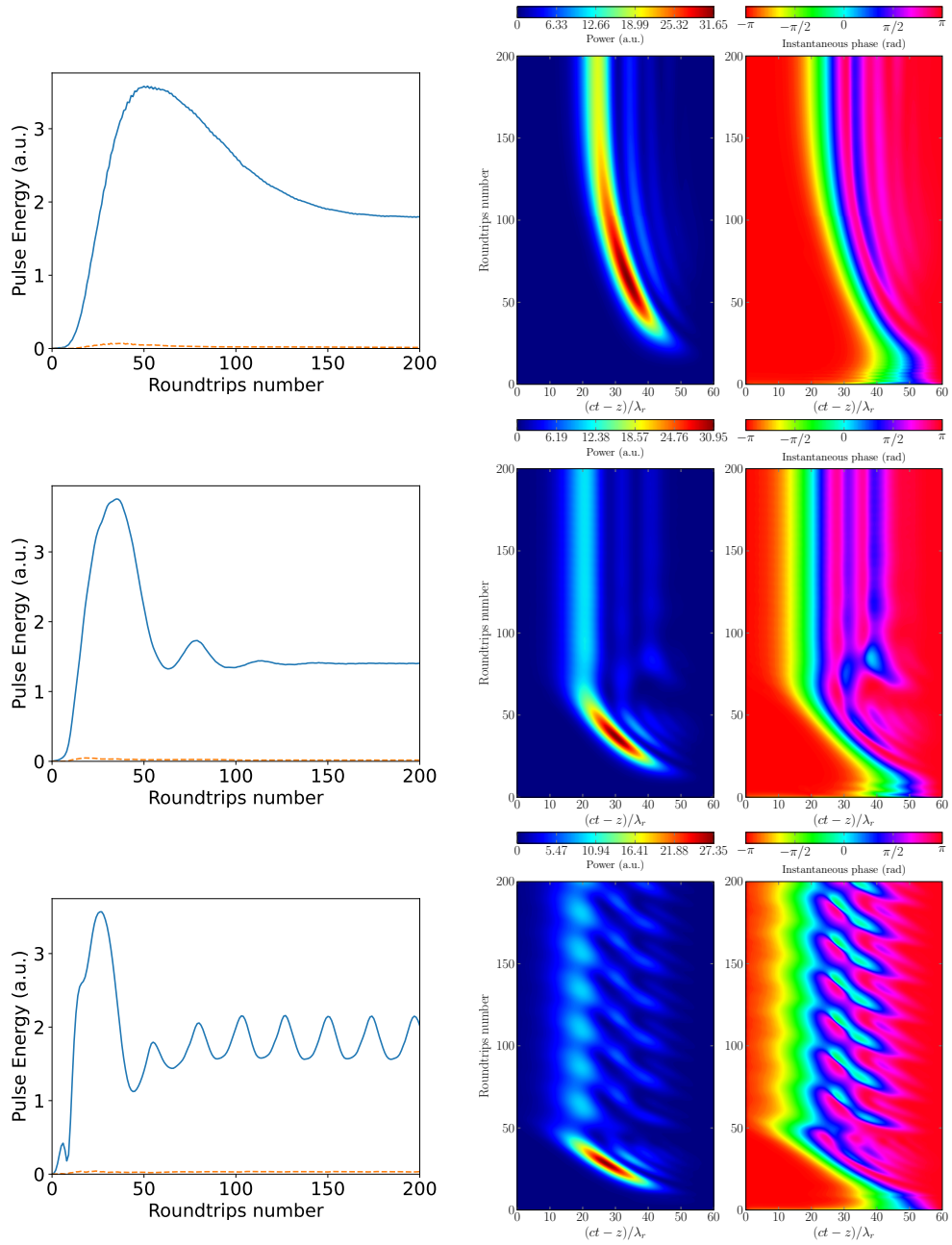


Figure 4.10: (Left) The fundamental (solid blue) and third harmonic (dashed orange) spectral pulse energy evolution as the function of cavity roundtrip number for cavity detunings of (top to bottom)  $2\delta L = 0.6\lambda_r$ ,  $2\delta L = 0.9\lambda_r$ , and  $2\delta L = 1.2\lambda_r$ . (Right) Contour plot of the FEL pulse power and phase evolution over multiple passes for the corresponding cavity detunings.

shot noise, simulations were also conducted using a ‘smooth’ Gaussian current profile where the spontaneous shot-noise emission overcomes over any CSE during start-up. Figure 4.11 displays the radiation-scaled power and the spectral component of the intracavity FEL output for a detuning scenario of  $2\delta L/\lambda_r = 0.4$ . A noisier initial power output is noticed after the first pass through the FEL oscillator, aligning with spontaneous shot-noise emission rather than the CSE from the rectangular beam current shown in Figure 4.8. Although the fundamental frequency  $\omega/\omega_r = 1$  is initially dominant, the power growth of the third harmonic becomes more evident with increased pass numbers, particularly in the steady-state.

The effects similar to using a rectangular beam can be observed with a Gaussian electron beam in Figure 4.12, which depicts the scaled spectral pulse energy (Figure 4.12a) for  $2\delta L/\lambda_r = 0.4$ . The fundamental (solid line) shows a higher initial gain starting from electron shot noise. The fundamental pulse energy peaks at pass numbers around 190 and then decays, while the third harmonic (dashed line) continues to amplify. The fundamental gain here is lower compared to the rectangular beam cases (Figures 4.9 and 4.10), where the FEL initiates from coherent spontaneous emission (CSE). Additionally, the contour plot of the instantaneous pulse power and phase (Figure 4.12b) reveals that the third harmonic starts to dominate for pass numbers greater than 200. This third harmonic pulse continues to amplify until it reaches steady-state saturation at pass numbers exceeding 350.

Similar to the rectangular electron beam current profile, simulations with a smooth Gaussian current profile indicate that the significant development of the third harmonic into a steady state is limited to cavity detunings smaller than the fundamental wavelength scale  $2\delta L < \lambda_r$ . It can be inferred that the increased pulse energies for the sub-wavelength cavity detuning shown in Figure 4.5c result from harmonic lasing effects. This highlights sub-wavelength cavity detuning as the key mechanism causing the harmonic lasing effect, regardless of whether CSE or spontaneous shot-noise serves as the dominant initial field in the cavity.

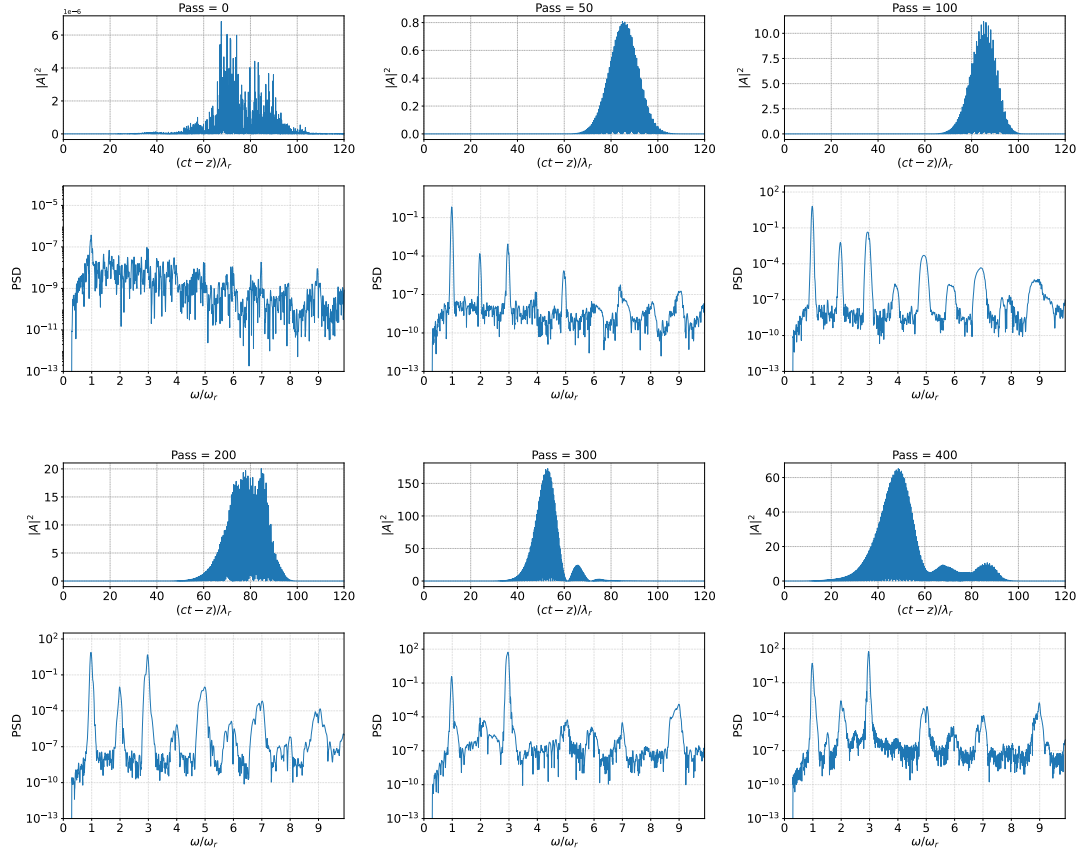


Figure 4.11: The temporal, scaled power profiles,  $|A|^2$ , at the undulator exit for the central transverse node of the Puffin output field, corresponding to the midpoint of the 2D transverse grid along the temporal axis, and its corresponding power spectral density (PSD), for different pass numbers through the cavity for a cavity detuning of  $2\delta L = 0.4\lambda_r$ . It can be seen that, while there is initial growth of the fundamental  $\omega/\omega_r \approx 1$  from spontaneous shot-noise, the third harmonic  $\omega/\omega_r \approx 3$  evolves to dominate at larger pass numbers into the steady state.

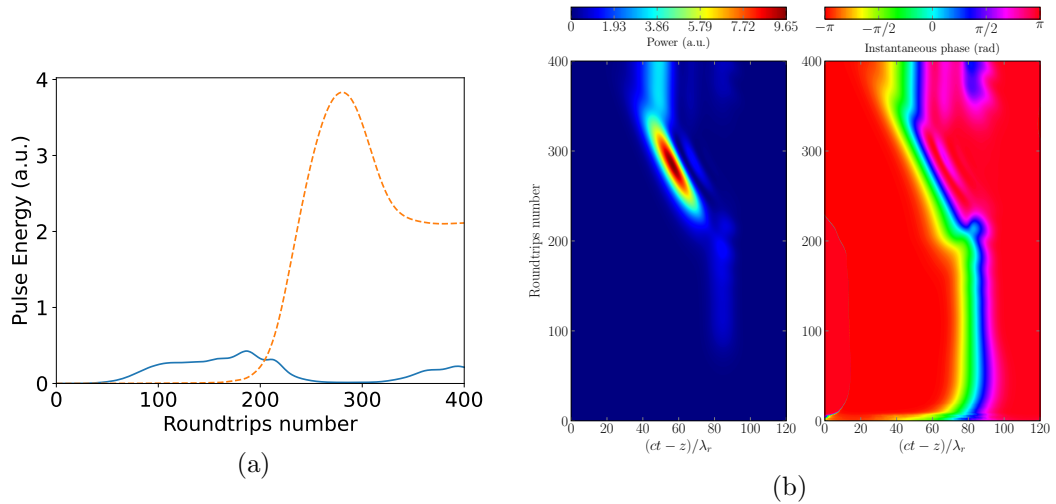


Figure 4.12: (a) The fundamental (solid blue) and third harmonic (dashed red) spectral pulse energy evolution as the function of cavity roundtrip number for a cavity detuning of  $2\delta L = 0.4\lambda_r$ . The process starts from Gaussian electron beam current. (b) Contour plot of the FEL pulse power and phase evolution over multiple passes for the corresponding cavity detuning.

## 4.4 Conclusion

The combined application of the Puffin and OPC FEL simulation codes offers a novel method for modelling cavity-based FELs at sub-wavelength scales, taking into account Coherent Spontaneous Emission and cavity detuning. The simulations conducted in this study are the first to address the impacts of sub-wavelength cavity detuning, revealing an unanticipated steady-state lasing at the third harmonic.

The generation of CSE, as modelled here with a rectangular electron beam current profile, has been shown to produce higher radiation powers compared to electron beam shot-noise [43]. This CSE could potentially be used to improve or replace external lasers in seeded cavity FELs, as studied by [27]. Additionally, when combined with sub-wavelength cavity detuning, CSE may help stabilise, or further enhance, the output properties of FELs. These effects are generally observed in longer wavelength sources where electron pulse current variations happen more swiftly than in shorter VUV to X-ray wavelength FELs.

An electron bunch with a Gaussian current profile, in which shot-noise spontaneous emission was the primary factor in the CSE, highlighted the importance of sub-

wavelength cavity detuning in the harmonic lasing observed and confirmed this effect with various beam current shapes. These results open up new paths for further research into the wider impacts and applications of FEL technology and development.

One area not explored in this work is the behaviour of sub-wavelength cavity detuning, such as from vibrations affecting the cavity length or from active tuning to improve output. Another area is the implementation of crystal optics, which are employed in shorter wavelength FEL designs and are predicted to yield different outcomes compared to the sub-wavelength cavity size alterations discussed here. Investigating these phenomena, their practicality, and other related studies could reveal new possibilities and will be the focus of future research.

## Chapter 5

# Saturation of Superradiant Pulses in Free-Electron Lasers

An investigation is conducted on the saturation mechanism of a single superradiant ‘spike’ of radiation in a Free Electron Laser. A one-dimensional (1D) computational model is created using the unaveraged FEL simulation code, Puffin, which enables the sub-radiation wavelength evolution of both the spike radiation field and the electron dynamics to be simulated until the highly nonlinear saturation phase of the spike is reached. Animations showing the entire interaction process from beginning to end are available. The resulting saturated spike duration is at the sub-wavelength scale and exhibits a broad spectrum. Electrons traversing the spike can experience energy losses and gains that significantly exceed those in a ‘normal’ non-pulsed FEL interaction. A saturation mechanism is proposed and evaluated through a straightforward analysis of the 1D FEL equations. The scaling results of this analysis align well with the numerical results. A simple model to account for the three-dimensional (3D) diffraction effects of the radiation is applied to the 1D simulation results. This model greatly diminishes the longer wavelengths of the power spectrum, which are predominantly emitted after the electrons have passed through the spike, and is qualitatively consistent with recent experimental findings [80].

## 5.1 Introduction

Research on analytical study of FEL amplifiers has found two distinct solutions to the equations governing the simultaneous propagation of electrons and radiation within the FEL undulator: the Steady-State and Superradiant regimes [9,10,12,42,53]. When averaging the equations describing the electron-radiation interaction of FEL on at least one resonant radiation wavelength, the resultant pulsed superradiant emission, accounting for pulse effects, has been shown to exhibit a hyperbolic secant solution for the emitted radiation field in this regime [52]. Additionally, a recent experiment explored superradiant pulses produced by an FEL oscillator [80].

As a superradiant radiation pulse, or ‘spike’, propagates within an electron beam, the averaged analytical and numerical predictions indicate that an increase in the spike’s peak power corresponds to a decrease in its temporal length. It is evident that both the analysis and simulations begin to fail when the spike durations approach the radiation’s wavelength. Consequently, the evolution of ultra-short spikes in FELs remains not fully explained or comprehended. Neither analytical methods nor numerical simulations can ascertain whether superradiant spikes eventually reach a saturation point, leading to a breakdown of the self-similar solution. Initial research has demonstrated that discrepancies arise between the averaged and unaveraged numerical simulations when sub-period effects emerge during the evolution of ultra-short superradiant FEL spikes [13,39].

To improve our knowledge of spike evolution, the unaveraged numerical simulation tool Puffin [14,16] was utilised to examine the growth and evolution of highly nonlinear FEL radiation spikes as they move through a uniform, effectively infinitely long, electron beam. These simulations, performed under the 1D, cold beam conditions, have revealed a new regime where the superradiant spike reaches saturation. This study offers an idealised reference point and provides new insights into the behaviour of FEL superradiant spikes and electron dynamics at sub-wavelength scales.

## 5.2 Simulation model

Presented here are unaveraged numerical simulations of FEL pulse evolution using the Puffin model in the 1D scenario. The simulation parameters are chosen not to replicate any specific existing or proposed FEL experiment but rather to explore the fundamental FEL interaction as it transitions into a highly nonlinear regime characterised by intense radiation pulse evolution at sub-wavelength resolution. Previous research has shown that Puffin simulations are in good agreement with experimental data and averaged 3D FEL simulation codes when the FEL parameters remain relatively constant over a radiation wavelength [13].

The FEL parameter  $\rho$ , utilised to scale the parameters here, is defined as [11]:

$$\rho = \frac{1}{\gamma_r} \left( \frac{a_w \omega_p}{4ck_w} \right)^{2/3}, \quad (5.1)$$

where  $\gamma_r$  represents the resonant electron beam's Lorentz factor,  $a_w$  denotes the undulator parameter,  $k_w = 2\pi/\lambda_w$  describes the undulator wavenumber,  $\omega_p = \sqrt{e^2 n_p / \epsilon_0 m_e}$  is the non-relativistic electron plasma frequency, and  $n_p$  indicates the electron beam's peak number density.

Other significant scaling parameters derived from this primary scaling parameter are [40]: the cooperation length,  $l_c = \lambda_r / 4\pi\rho$ , where  $\lambda_r$  represents the resonant radiation wavelength; the gain length,  $l_g = \lambda_w / 4\pi\rho$ , with  $\lambda_w$  being the undulator period; the scaled distance through the undulator,  $\bar{z} = z/l_g = 4\pi\rho N_w$ , where  $N_w$  denotes the number of undulator periods, and  $\bar{z}_2 = (ct - z)/l_c$ , signifying the scaled length in the radiation frame of reference.

In the Puffin simulation code, the electron beam is represented using a collection of macroparticles. This beam is considered to be a continuous wave (CW) cold beam with zero-energy spread, and all initial parameters are uniformly distributed. The coupled radiation and electron equations are computed within a simulation window that moves at the speed of light, resulting in a fixed width in  $\bar{z}_2$ . Since the electrons move at slower speeds, macroparticles consistently move to larger values of  $\bar{z}_2$  within this window, and a resonant macroparticle has a propagation speed of  $d\bar{z}_2/d\bar{z} = 1$ . The condition that

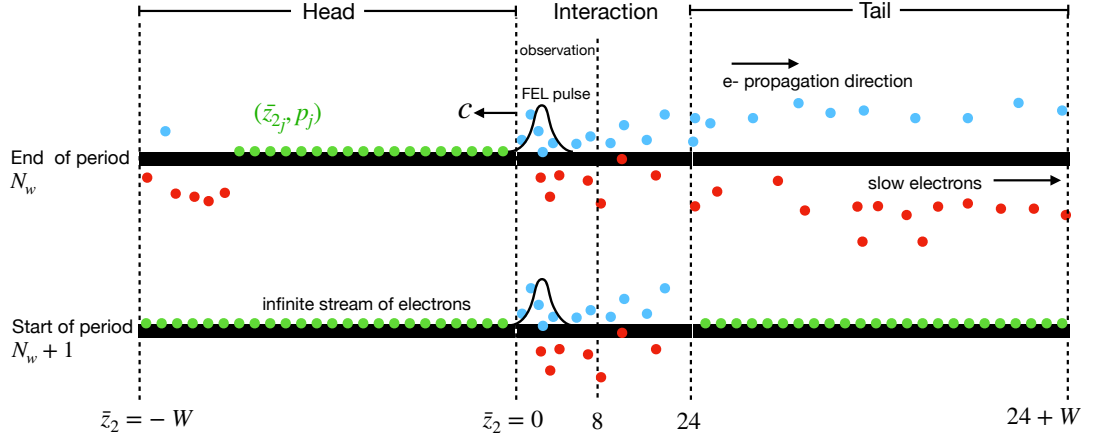


Figure 5.1: Schematic of the simulation window in the scaled radiation frame of reference  $\bar{z}_2 = (ct - z)/l_c$ . It consists of three main regions, Head, Interaction and Tail. All macroparticles propagate left-to-right as their speed is less than that of light. Top: The macroparticles representing the electron beam have propagated one undulator period (left-to-right) through an intense radiation pulse. The ‘slow’ macroparticles (red) have lost energy to the radiation pulse and some have propagated into the tail window  $24 < \bar{z}_2 < 24 + W$ , as have some that have gained energy from the pulse (blue). Those that propagate further than the Tail window,  $\bar{z}_2 > 24 + W$ , are re-assigned into the Head window by application of periodic boundary conditions over  $-W < \bar{z}_2 < 24 + W$ . Bottom: All macroparticles in both the Head and Tail windows are then re-initialised as shown, with equal spacing in  $\bar{z}_2$  and a resonant, monoenergetic distribution. Here  $W$  represents the range of the windows in  $\bar{z}_2$  for simulating different values of  $\rho$ , e.g.  $W = 238$  for  $1 \leq 4\pi\rho \leq 1.25$ , and  $W = 488$  for  $0.5 \leq 4\pi\rho < 1$ .

$d\bar{z}_2/d\bar{z} > 0$  for all macroparticles supports the simulation of an infinite electron beam. The simulation window is divided into three specific regions: the head, interaction, and tail windows. The interaction window holds the initial radiation pulse field, where the radiation spike develops. At the end of each undulator period, the positions of the macroparticles in  $\bar{z}_2$  are checked, and those exiting the interaction window into the tail window are reset in both position and energy to refill the head window, thus maintaining a CW electron beam. The initial number of macroparticles per radiation wavelength is set to 800. A diagram illustrating the simulation windows and the initialisation process of the macroparticles from the end of  $N_w$  to the beginning of  $N_w + 1$  undulator periods is presented in Figure 5.1.

The initial phases of the electrons in the  $j$ th macroparticle,  $\bar{z}_{2j}$ , are evenly distributed throughout the simulation window. All Lorentz factors are set to the resonant energy  $\gamma_r = 100$ , ensuring that  $p_j = (\gamma_j - \gamma_r)/\rho\gamma_r = 0$  for all  $j$ . The undulator has a period of  $\lambda_w = 4$  cm and an undulator parameter of  $a_w = 1.0$ .

### 5.3 Simulation Example

The behaviour of superradiant pulses in the highly non-linear regime and with sub-wavelength resolution is now examined using the above simulation method and parameters in a helical undulator setup. The evolution of the radiation-electron system is initially modelled starting from a low-power input seed pulse to a very short, high-power superradiant spike. It is shown that, for the relatively large value of  $\rho = 1/4\pi$  considered, the interaction of the superradiant spike reaches saturation after a long propagation distance of approximately 400 gain lengths ( $\bar{z} \approx 400$ ), with a peak scaled intensity around 4000 times the usual steady-state saturation intensity of  $|A_{sat}|^2 \sim 1.4$  [11]. Although this type of evolution may not be feasible with current FEL systems, studying the saturation process of the radiation spike is of general interest.

The scaling of the saturated peak spike energy values, among other parameters, is subsequently examined for different values of  $\rho$ , and an approximation is provided on how 3D diffraction effects could influence the characteristics of the radiation spike.

### 5.3.1 Simulation of Superradiant Pulses

Given the value of  $\rho = 1/4\pi$ , a single radiation period corresponds to a scaled length of  $\Delta\bar{z}_2 = 1$ , and similarly, one undulator period is  $\Delta\bar{z} = 1$ . A relatively small Gaussian seed radiation field with a scaled intensity of  $|A_0|^2 = 0.4$ , a width of  $\sigma(\bar{z}_2) = 2$ , and centred at  $\bar{z}_2 = 12$ , is introduced into the interaction window  $0 \leq \bar{z}_2 \leq 24$ , while it is set to zero elsewhere at the undulator entrance  $\bar{z} = 0$ . This seed field gives rise to a superradiant interaction which becomes essentially independent of the initial seed. The field is sampled uniformly at 201 points per radiation wavelength. After travelling a scaled distance of  $\bar{z} = 4\pi\rho N$  for  $N = 1, 2, 3, \dots, N_w$ , where  $N_w$  represents the number of undulator periods, the macroparticles and the radiation field outside the range  $0 \leq \bar{z}_2 \leq 24$  are reinitialised in the head and tail windows as previously described in Figure 5.1. The number of integration steps over one undulator period is 800, with the macroparticle and radiation data being saved every 20 steps. The sub-wavelength radiation and electron dynamics can thus be observed with a resolution of  $\lambda_r/20$ .

The simulation results leading to a typical FEL saturation in steady-state conditions are illustrated in Figure 5.2 at undulator positions  $\bar{z} = 9$  and 10 within the observation interval  $0 \leq \bar{z}_2 \leq 8$  in the interaction window, as depicted in Figure 5.1.

The electron phase-space  $(\bar{z}_{2j}, p_j)$ , the components of the scaled circularly polarised radiation fields  $A_x$  and  $A_y$ , the associated scaled intensity  $|A|^2$ , and the scaled power spectrum  $\tilde{P}$  are depicted. Additionally, the localised electron number density  $\bar{n}_e$ , which is initially  $\bar{n}_e = 1$  for a ‘fresh’ uniform electron beam at  $\bar{z} = 0$ , and the localised energy  $\Sigma p_j$  are also plotted.

As shown in Figure 5.2a, when  $\bar{z} = 9$ , the interaction approaches the ‘normal’, post-linear evolution FEL saturation phase, as outlined in [40]. The electrons are observed to be tightly bunched around the peak of the radiation pulse, with a spacing corresponding to the fundamental radiation wavelength ( $\Delta\bar{z}_2 \sim 1$ ). It should be noted that these bunched electrons locally drive the field at a sub-wavelength scale, differing from averaged simulations.

As shown in Figure 5.2b, the electron bunching reaches saturation and begins to de-bunch at  $\bar{z} = 10$ , approximately at the peak of the radiation power around  $\bar{z}_2 \sim 5.5$ .

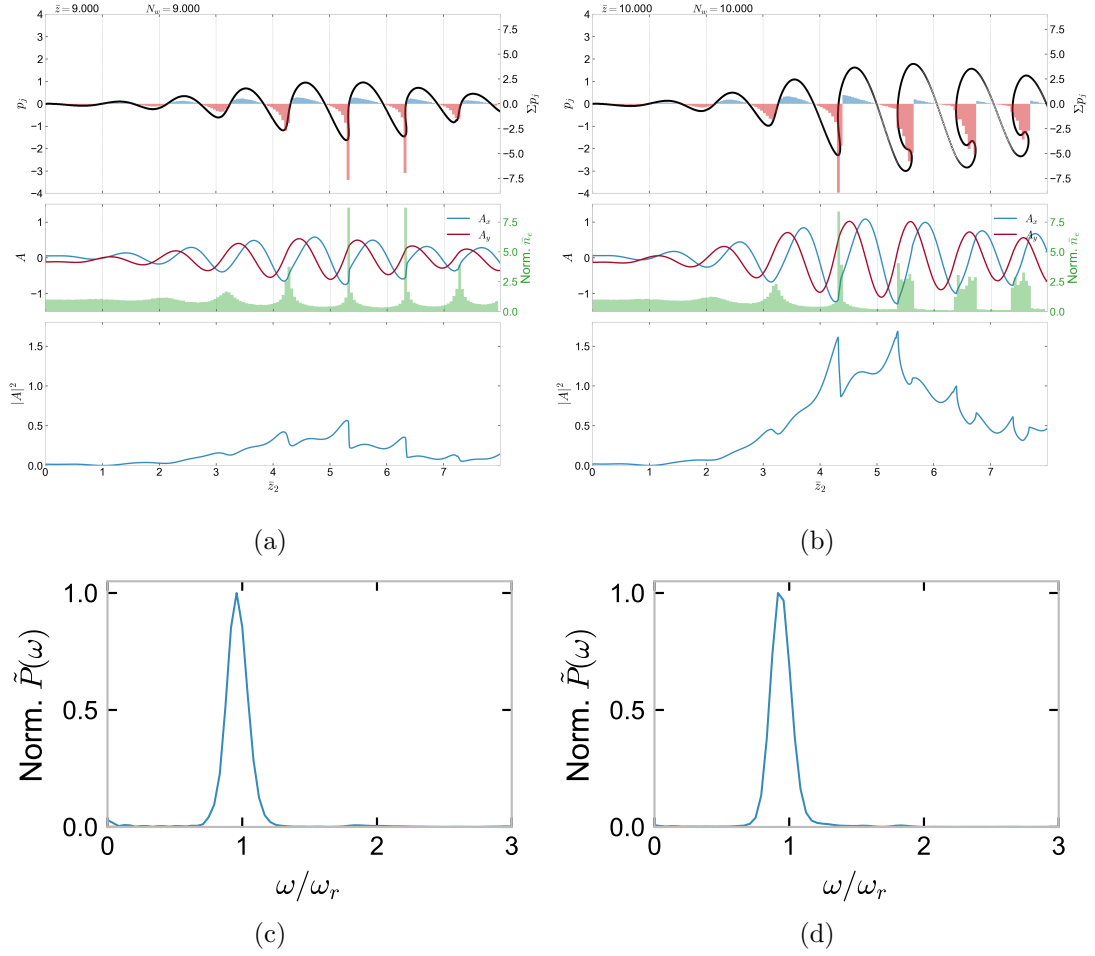


Figure 5.2: FEL electron phase-space and radiation evolution about post-linear evolution saturation of the radiation pulse. (a,c) are at  $\bar{z} = 9$ , and (b,d) are at  $\bar{z} = 10$ . Top (a,b): The electron phase-space ( $\bar{z}_{2j}, p_j$ ) (black dotted) and localised net energy  $\Sigma p_j$ . Middle (a,b): The radiation field components  $A_x, A_y$  (blue and red solid lines) and localised electron number density  $\bar{n}_e$  (green bars) as normalised to 1 for a ‘fresh’ unbunched beam. The bar plots for the localised electron parameters  $\Sigma p_j$  and  $\bar{n}_e$  are within the bins of width  $\lambda_r/20$ . Bottom (a,b): The scaled radiation power  $|A(\bar{z}_2)|^2$ . Plots (c,d) are of the scaled spectral power  $\tilde{P}(\omega)$  as a function of frequency scaled with respect to the resonant frequency  $\omega_r$ . Note that as  $4\pi\rho = 1$  in this simulation, a resonant electron propagates one undulator period for a change of  $\Delta\bar{z} = 1$ , and one radiation period corresponds to a change of  $\Delta\bar{z}_2 = 1$ . **Electronic version:** An animation depicting the interaction across 2 undulator periods can be found at [63], while a complete animation showing the evolution from the beginning of the undulator to full saturation is accessible at [56].

For  $\bar{z}_2 > 5.5$ , the electrons that are de-bunching start to re-absorb energy from the radiation, leading to a reduction in pulse duration post-saturation. At both values of  $\bar{z}$ , the power spectrum is centred around the resonance  $\omega/\omega_r = 1$ .

As interaction proceeds to higher values of  $\bar{z} > 10$ , it is anticipated that this process will continue with each successive undulator period. Maximum electron bunching and coherent emission are expected to occur just prior to the radiation power peak, followed by de-bunching and re-absorption. This sequence then drives the increase of the scaled radiation peak power, while shortening its pulse duration. This behaviour is depicted in Figure 5.3, where a breakdown of the averaged theory model is observed. Electron bunching deviates from being aligned at the resonant wavelength, and radiation powers remain approximately constant over a radiation wavelength.

As illustrated in Figure 5.3a, at a scaled undulator distance of  $\bar{z} = 40$ , the electron pulse is seen to enter the leading ‘edge’ of the radiation pulse at approximately  $\bar{z}_2 \sim 1$ , initiating the bunching process, which is evident from the phase-space and the normalised electron density,  $\bar{n}_e$  (middle). It is important to note that the variations in the electron density for  $\bar{z}_2 > 2$  are primarily resulting from interactions during earlier undulator periods. The electron bunching process is observed to occur within one radiation period over one undulator period, centred around the peak power of the main radiation pulse at approximately  $\bar{z}_2 \sim 2$ .

Throughout one undulator period ( $\Delta\bar{z} = 1$ ), the electrons significantly bunch within the short radiation pulse, which is centred at  $\bar{z}_2 \sim 2$  and has a Full Width at Half Maximum (FWHM) in  $\bar{z}_2$  of  $\tau_p \approx 1$ . These electrons lose energy and then move out of the main pulse, observed within the interval  $2.5 < \bar{z}_2 < 3.5$  for  $p_j < 0$ . Conversely, some electrons gain energy to  $p_j > 0$ . These higher energy electrons do not propagate to larger  $\bar{z}_2$  values as rapidly as those that have lost energy with  $p_j < 0$ . They also tend to maintain their higher energy across many undulator periods. The energy gains are considerably higher than during a typical FEL process, where the maximum gains are about  $p_j \sim 1$ —refer to Figures 5.2a and 5.2b. As may be expected and subsequently shown, the energy gain of these electrons increases with an increase in the spike power.

Observe that certain electrons within the range  $2.7 < \bar{z}_2 < 3.5$  experience a cycle of

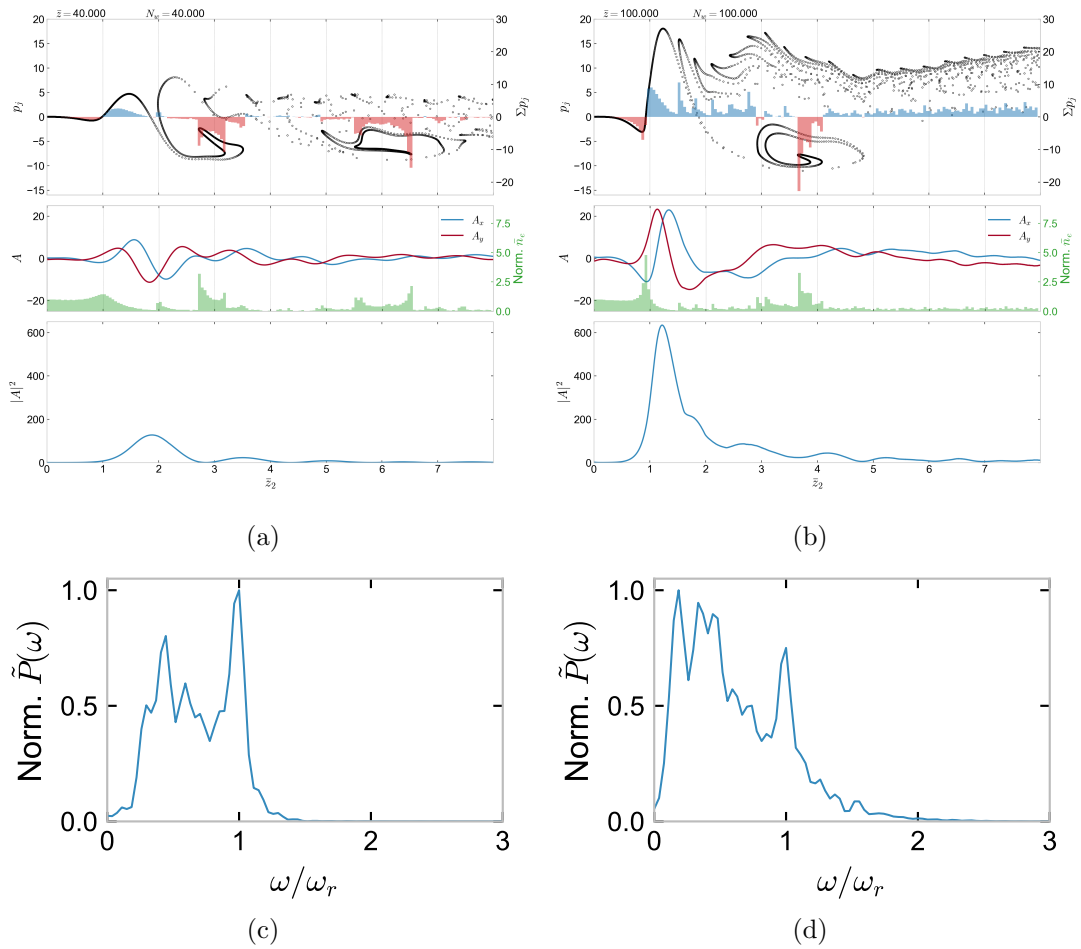


Figure 5.3: As Figure 5.2, but for scaled undulator distances of  $\bar{z} = 40$  (left) and  $\bar{z} = 100$  (right). **Electronic version:** An animation depicting the interaction across 2 undulator periods can be found at [57, 60], while a complete animation showing the evolution from the beginning of the undulator to full saturation is accessible at [56].

energy loss and subsequent recovery during their interaction with the radiation pulse. This phenomenon arises from their large initial energy loss from  $p_j = 0$  to  $p_j \sim -8$ , occurring in a time frame shorter than a single undulator period ( $\bar{z} < 1$ ), as they enter the radiation pulse and are exposed to its rapidly increasing power. This loss of energy results in their rapid movement in  $\bar{z}_2$  within the high-power pulse during one undulator period, transitioning from a radiation emission phase, where they lose energy, to a radiation absorption phase, where they regain energy.

As the electrons travel away from the initial radiation pulse, they continually emit and absorb radiation. This occurs with less bunching, resulting in a secondary pulse at approximately  $\bar{z}_2 \sim 3$ , followed by additional pulses, each with decreasing intensity.

The electrons passing through this pulse structure for  $\bar{z}_2 > 3$  exhibit bunching patterns exceeding one radiation wavelength for those with lower energies, and less than one radiation wavelength for those with higher energies. Electrons at lower energies radiate at longer wavelengths, whereas those at higher energies emit at shorter wavelengths. This phenomenon is depicted in the corresponding scaled radiation power spectrum in Figure 5.3c, showing a significant lower frequency peak ( $\omega/\omega_r \sim 0.5$ ). Electrons that gain energy, featuring a smaller sub-wavelength bunching structure, contribute to an increased emission at frequencies just above resonance ( $\omega/\omega_r \sim 1$ ). This non-linear radiation pulse emission retains similarities to the superradiant structures as described in [52, 54, 80].

As illustrated in Figure 5.3b, at a scaled undulator distance of  $\bar{z} = 100$ , it is observable that the process described in Figure 5.3a has progressed. The peak radiation power of the pulse has increased and its duration has shortened. This combination of increased power and shortened duration decreases the time electrons spend within an undulator period that electrons experience within the first peak, now centred at  $\bar{z}_2 \sim 1.2$ . Consequently, electrons proceed into the subsequent radiation pulse(s), centred at higher  $\bar{z}_2$  values, during one undulator period, resulting in a more complex interaction between the main pulse and sub-pulses with the electrons. The main peak's pulse width has now reduced to slightly more than half of the radiation wavelength,  $\tau_p \sim 0.5$ .

For both the cases where  $\bar{z} = 40$  and 100, the separation between the lower energy electron bunches that have interacted with the radiation pulse (and subsequently moved out of the observation window as shown in Figure 5.3d) is more than two fundamental wavelengths. This leads to a significant increase in emission at lower frequencies,  $\omega/\omega_r < 0.5$ , as observed in the spectral power in Figures (5.3c, 5.3d).

In Figure 5.3d, another feature in this regime is the rapid energy variation of electrons that initially lose energy upon entering the pulse. This is partly attributed to the rapid inter-wavelength scale motion of the electrons within one undulator period. Electrons that initially gain energy from the radiation pulse can reach a relatively high energy value of  $p_j \sim 10$  during the first peak. These accelerated electrons form a more stable, shorter period, electron bunching band after the first peak at  $\bar{z}_2 > 2$ . This behaviour is apparent in the  $\Sigma p_j$  and  $\bar{n}_e$  plots in Figure 5.3b (top and middle). These smaller, higher-energy electron bunches, located within the interval of  $1 < \bar{z}_2 < 3$ , have spacings less than the fundamental radiation wavelength, resulting in a noticeable bandwidth broadening in the higher frequency range, as shown in Figure 5.3d, for  $\omega/\omega_r > 1$ .

Note that electrons accelerated by the pulse and therefore increased in energy tend to remain within the simulation window, travelling at the speed of light for a considerably longer duration than those that have lost energy due to the pulse. The electrons with reduced energy quickly move to higher  $\bar{z}_2$  values, as shown in the animations, and eventually exit the simulation window. Consequently, there are more electrons at higher energy within the simulation window because most electrons that have significantly lost energy to the pulse are no longer visible within the window.

In Figure 5.4, the progression of the interaction is shown in  $\bar{z} = 200$  (left) and  $\bar{z} = 400$  (right). The first radiation peak around  $\bar{z}_2 \approx 1$  has increased in power, while its width has decreased to significantly less than one radiation wavelength. Electrons that gain energy achieve higher levels, whereas those that lose energy reach levels similar to those in the Figure 5.3. The increased power and decreased width of the radiation pulse cause significant energy fluctuations in the electrons over a short propagation interval. In this scenario, electrons can travel through a pulse width  $\tau_p < 0.25$  in less

than a quarter of an undulator period, experiencing both energy loss and gain during the process. This is illustrated by the increased spiraling in the phase space of the lower-energy electrons that have passed through the initial pulse, compared to those in Figure 5.3.

As  $\bar{z}$  increases and the peak pulse narrows, the field's higher frequency components with  $\omega/\omega_r > 1$  grow further. Electrons that have moved past the radiation peak form bunches with a larger spacing in  $\bar{z}_2 > 1$ , leading to lower-frequency emissions. This effect is observed in the lower frequency radiation fields at the pulse's trailing edge, where a noticeable correlation exists between the electron bunches and the scaled field phase. This correlation persists to larger  $\bar{z}$  as the interaction continues.

In Figure 5.5, the short and intense pulse seems to have reached a highly nonlinear saturation state. The increase in both the peak power and the width of the pulse is almost identical at  $\bar{z} = 800$  (left) and  $\bar{z} = 1100$  (right). This pulse saturation process and its scaling based on the FEL parameter  $\rho$  are now being examined.

### 5.3.2 Pulse saturation

As the interaction progresses to larger values of  $\bar{z}$ , the increase of the first radiation spike in the scaled radiation power is observed to have saturated with  $|A_p|^2 \approx 7000$  around  $\bar{z}_2 \approx 0.8$ , as depicted in Figure 5.5. In Figure 5.2(a), it is evident that the average energy loss by the electrons immediately after traversing the first spike is substantial, causing the electron bunches to quickly travel in  $\bar{z}_2$  and thus increase the spacing between bunches after the spike. In contrast, in Figure 5.5(a), it can be seen that the average energy loss decreases after saturation, resulting in slower propagation of electrons in  $\bar{z}_2$ . Consequently, the electron bunches that have passed through the first spike exhibit a smaller separation in  $\bar{z}_2$ . Where the separation between bunched electrons is greater, it is noted that this leads to longer wavelength emissions. Additionally, as saturation occurs, there are more electrons that gain energy from the spike. The relative energy gain for the  $j$ -th electron can be estimated from the definition of its  $p_j$  as  $(\gamma_j - \gamma_r)/\gamma_r = \rho p_j$ , which in Figure 5.5 shows a considerable maximum relative energy gain of  $(\gamma_j - \gamma_r)/\gamma_r \sim 5.2$ .

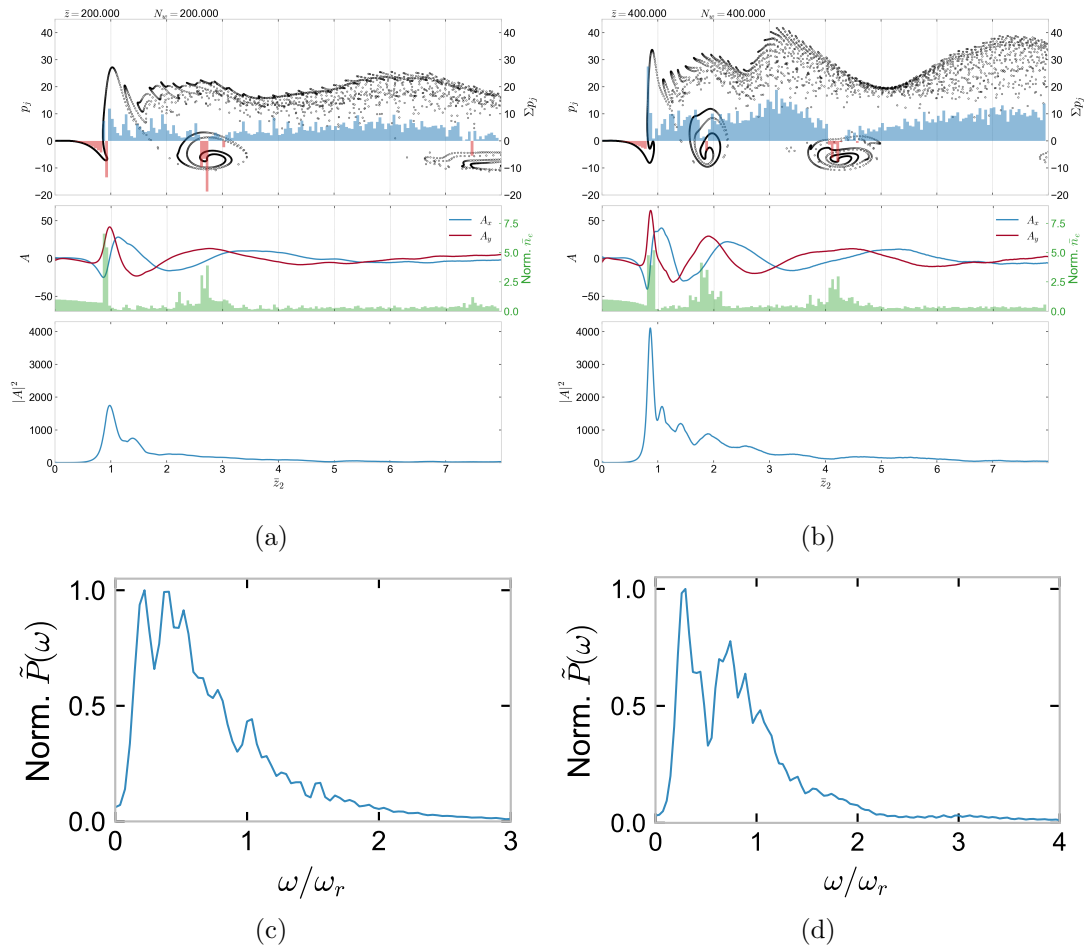


Figure 5.4: As Figure 5.2, but for scaled undulator distances of  $\bar{z} = 200$  (left) and  $\bar{z} = 400$  (right). **Electronic version:** An animation depicting the interaction across 2 undulator periods can be found at [59,61], while a complete animation showing the evolution from the beginning of the undulator to full saturation is accessible at [56].

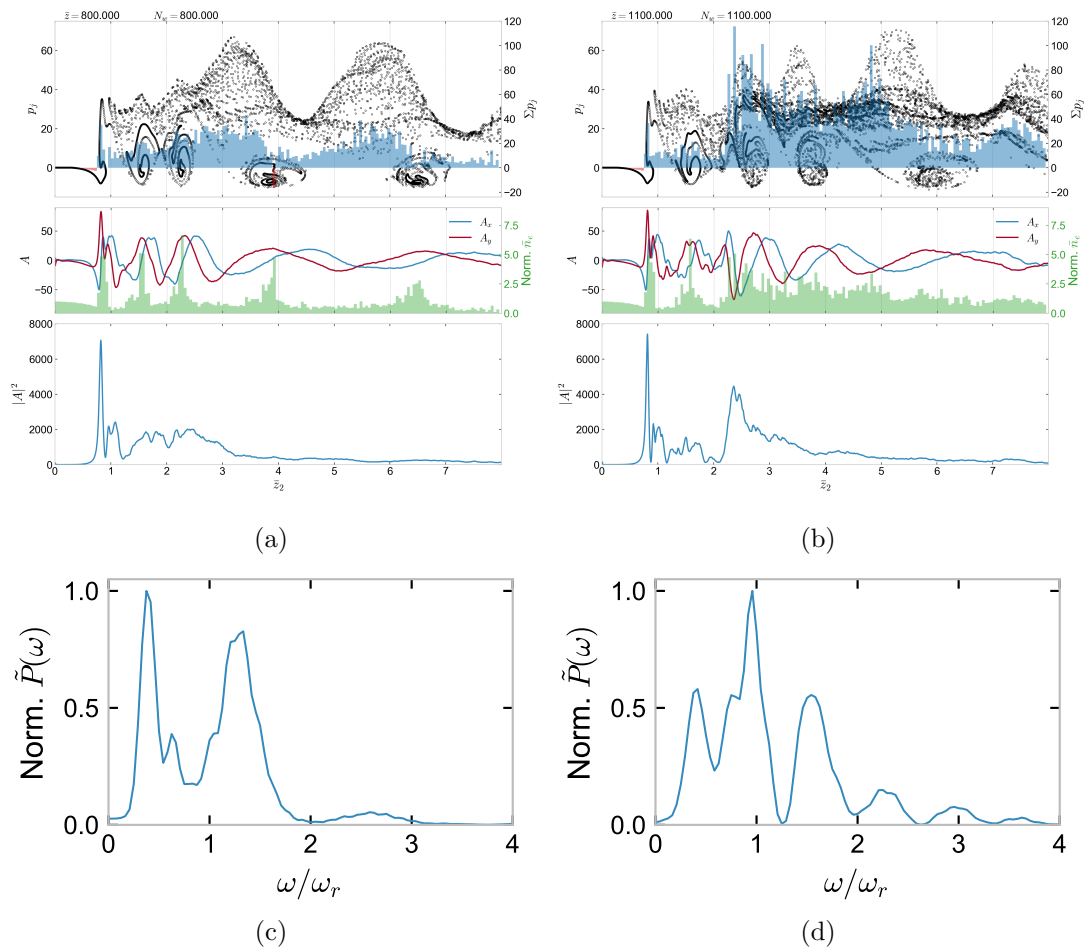


Figure 5.5: As Figure 5.2, but for scaled undulator distances of  $\bar{z} = 800$  (left) and  $\bar{z} = 1100$  (right). **Electronic version:** An animation depicting the interaction across 2 undulator periods can be found at [58, 62], while a complete animation showing the evolution from the beginning of the undulator to full saturation is accessible at [56].

In simple terms, it is proposed that the first radiation spike reaches saturation when the energy loss of electrons traveling through it allows them to cover a considerable distance relative to the radiation wavelength during one undulator period. In terms of scaling, saturation is defined as the point when an electron loses sufficient energy within one-half of an undulator period to travel an additional one-half of a resonant radiation wavelength  $\Delta\bar{z}_{2j}$  beyond its resonant slippage rate in the radiation reference frame of  $d\bar{z}_{2j}/d\bar{z} = 1$ , i.e.,  $\Delta\bar{z}_{2j} = \Delta\bar{z} = 2\pi\rho$ . An estimate of the scaling following this definition is provided in A.1. According to this, the scaled peak power of the spike is  $|A_p|^2 \approx 1/\pi^2\rho^4$ , and its scaled energy is  $\varepsilon_p \approx \tau_p|A_p|^2 \approx 4f/\pi\rho^3$ . Here,  $\tau_p = f \times 4\pi\rho$  represents the width of the spike in  $\bar{z}_2$ , with  $f$  being the spike width as a fraction of a single radiation wavelength.

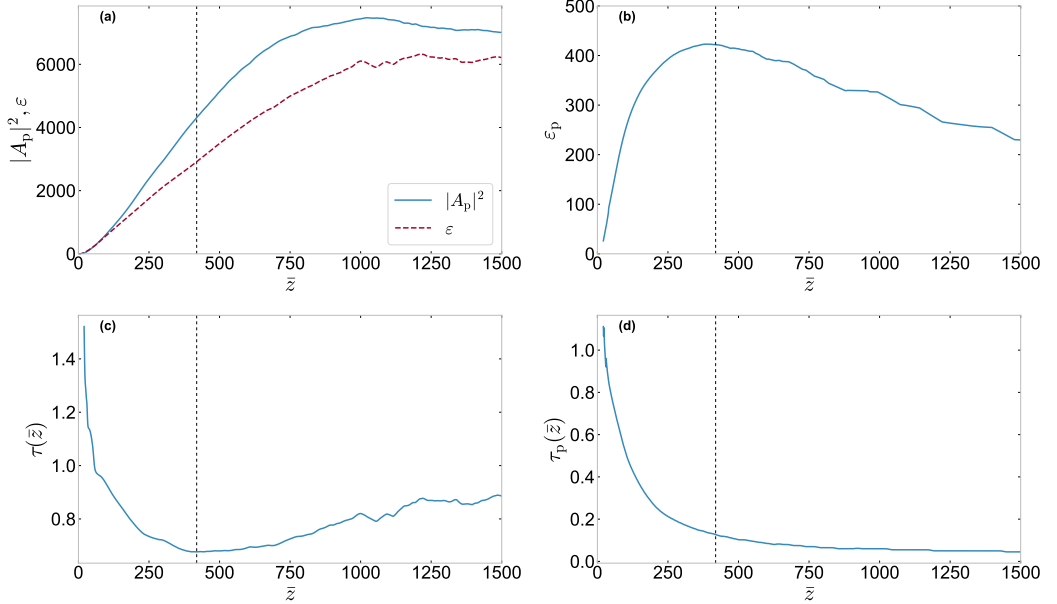


Figure 5.6: The FEL evolution as measured in the interval  $0 \leq \bar{z}_2 \leq 9$  as a function of  $\bar{z}$  for the case of  $4\pi\rho = 1$ . (a) scaled peak power  $|A_p|^2$  and pulse energy  $\varepsilon$ ; (b) scaled energy within the first peak (spike)  $\varepsilon_p$ ; (c) the scaled pulse duration  $\tau$  - the vertical dashed line shows the minimum defined as the point of saturation; and (d) the first radiation pulse (spike) duration  $\tau_p$ .

Through computer simulations, the term saturation is characterised by the minimum value of the full duration of the pulse  $\tau(\bar{z})$  within the simulation range  $0 < \bar{z}_2 < 8$ .

This can be determined using the formula  $\tau(\bar{z}) = \varepsilon(\bar{z})/|A_p(\bar{z})|^2$ , where the scaled pulse energy across the simulation interval is given by  $\varepsilon(\bar{z}) = \int |A(\bar{z}, \bar{z}_2)|^2 d\bar{z}_2$ , and the peak scaled power in this interval is  $|A_p(\bar{z})|^2$ , as previously described. The simulation results in relation to  $\bar{z}$  for  $4\pi\rho = 1$  are shown in Figure 5.6, showing an occurrence of saturation at  $\bar{z} \approx 419$ , as marked by the vertical dashed line in Figure 5.6(c). Although the peak power  $|A_p(\bar{z})|^2$  and the pulse energy  $\varepsilon(\bar{z})$  continue to rise after saturation, as depicted in Figure 5.6(a), the energy in the initial peak  $\varepsilon_p(\bar{z})$  (representing the radiation spike) also saturates at  $\bar{z} \approx 419$  before decreasing with further increase in  $\bar{z}$ , as illustrated in Figure 5.6(b). At the saturation point, the pulse duration  $\tau(\bar{z})$  reaches its minimum and subsequently starts to rise with  $\bar{z}$  (Figure 5.6(c)). In contrast, the width of the initial radiation spike,  $\tau_p(\bar{z}) = \varepsilon_p(\bar{z})/|A_p(\bar{z})|^2$ , continues to decrease as illustrated in Figure 5.6(d).

The above simulation was also performed in a range of  $4\pi\rho$  values from 0.5 to 1.25. For  $\gamma_r = 100$ , these  $\rho$  values typically correspond to FEL operational wavelengths that span from the far-infrared to the THz region. This facilitates a comparison of the saturated values, when  $\tau(\bar{z})$  reaches its minimum, with a straightforward scaling analysis presented in A.1. These saturated values and their optimal scalings are shown in Figure 5.7 for the peak radiation power  $|A_p|^2$  and the saturation undulator length  $\bar{z}_{\text{sat}}$ ; in Figure 5.8, for the radiation pulse energy  $\varepsilon$  and pulse duration  $\tau$  over the simulation period; and in Figure 5.9, for the pulse energy  $\varepsilon_p$  and duration  $\tau_p$  of the first radiation spike.

Based on the above saturation definition and the straightforward scaling analysis in A.1, the scaled estimates for the peak radiation power and the energy of the radiation spike were derived from A.5 and A.6, respectively. For instance, in the above simulations where  $4\pi\rho = 1$ , the predicted saturation values are  $|A_p|^2 \approx 2500$  and  $\varepsilon_p \approx 300$  for a fractional factor  $f = 0.12$ , as shown in Figure 5.9(b). Despite the significant approximations made in A.1, the relatively good correlation with the highly non-linear computational results from Figure 5.7(a) for  $|A_p|^2$  and Figure 5.9(a) for  $\varepsilon_p$  supports the hypothesis regarding the radiation spike saturation process. Additionally, this is evidenced by the strong agreement between the analysis and the best-fit scaling ob-

tained from the simulations for both  $|A_p|^2 \propto \rho^{-4}$  (Figure 5.7(a) and A.5) and  $\varepsilon_p \propto \rho^{-3}$  (Figure 5.9(a) and A.6).

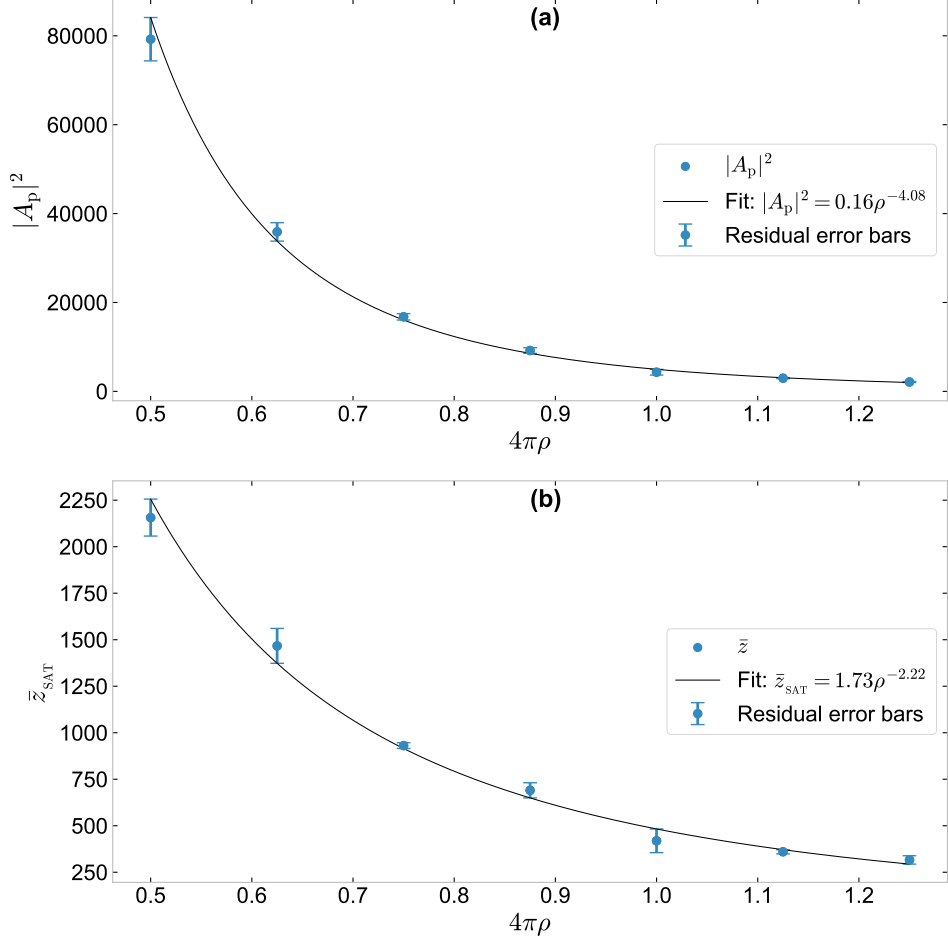


Figure 5.7: The saturated values of the simulations (dots) for (a) scaled peak power  $|A_p|^2$ , and (b) scaled saturation undulator length  $\bar{z}_{\text{sat}}$ , as a function of  $4\pi\rho$ . The solid lines are the fitting functions as given in the box.

Figures 5.7(a), 5.8(a), and 5.9(a) clearly show that as  $\rho$  decreases, higher radiation peak powers and pulse energies are needed to reach saturation. This occurs because lower  $\rho$  values result in a weaker interaction between electrons and the radiation field, necessitating increased radiation power to achieve the same energy transfer essential for saturation. Moreover, a shorter scaled pulse duration is necessary, as depicted in Figure 5.8(b). The first peak duration  $\tau_p$ , in terms of the radiation wavelength  $\lambda_r$ ,

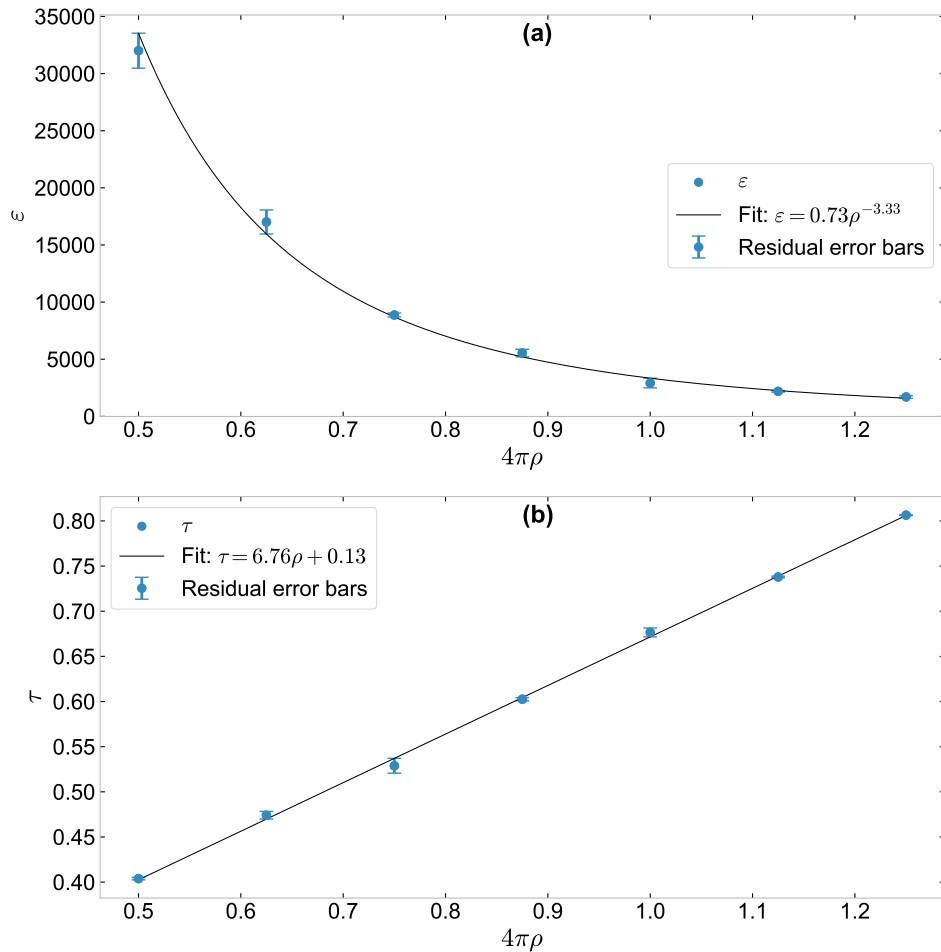


Figure 5.8: The saturated values of the simulations (dots) for (a) scaled pulse energy  $\varepsilon$ , and (b) pulse duration  $\tau$ , as a function of  $4\pi\rho$ . The solid lines are the fitting functions as given in the box.

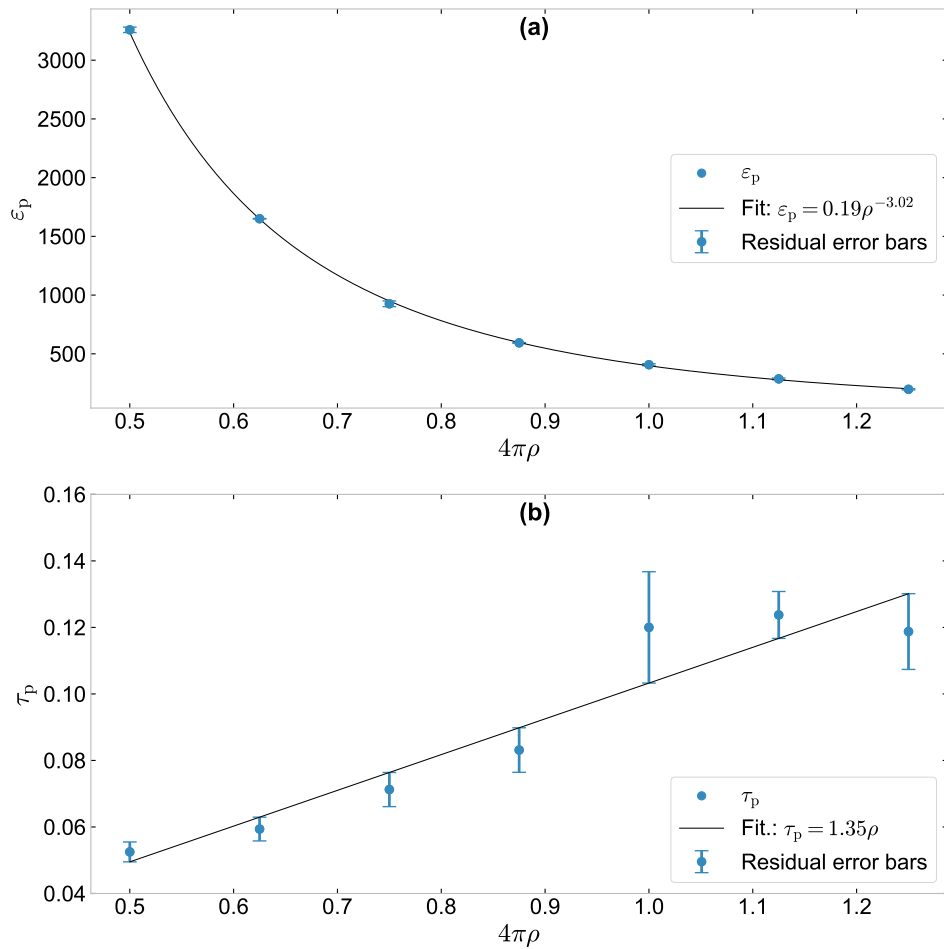


Figure 5.9: The saturated values of the simulations (dots) for (a) scaled energy of the first radiation pulse (spike)  $\varepsilon_p$ , and (b) its width  $\tau_p$ , as a function of  $4\pi\rho$ . The solid lines are the fitting functions as given in the box.

remains approximately constant for all values of  $4\pi\rho$ , as illustrated in Figure 5.9(b). This strongly indicates a single-cycle type limit where the radiation field reaches its minimal feasible duration. The requirement for a longer undulator to achieve saturation can also be observed in Figure 5.7(b). Therefore, modelling such saturation behaviour at lower values of  $\rho$  becomes increasingly computationally intensive.

A complete video showing the evolution of the superradiant spike from the beginning of the undulator to its saturated state can be found in [56].

### 5.3.3 Estimation of diffractive effects

The simulation and scaling results detailed above are conducted in one dimension (1D), thereby neglecting any three-dimensional (3D) effects such as radiation diffraction. It can be expected that the longer wavelengths of the radiation in the above simulations would diffract away from the electron beam, which is assumed to maintain a constant radius  $w_0$ . Provided there are no optical or gain ‘guiding’ effects [40] influencing the radiation through the electron beam, the radiation will diffract according to its Rayleigh range,  $z_R = \pi w_0^2/\lambda \propto \omega$ . Consequently, this leads to a greater separation between the electron beam and its radiation output at longer wavelengths/lower frequencies as the interaction progresses through the undulator.

Assumed a transverse Gaussian radiation profile, the intensity  $I$  can be described in terms of its peak power,  $P_0$ , as it travels a distance  $z$  through the undulator as:

$$I(z) = \frac{2P_0}{\pi w^2(z)}, \quad (5.2)$$

where  $w(z)$  is the transverse radiation beam size along the  $z$  axis:

$$w(z) = w_0 \sqrt{1 + \left(\frac{z}{z_R}\right)^2}. \quad (5.3)$$

As the distance  $z$  increases beyond  $Z_R$ ,  $w(z)$  tends to be inversely proportional to  $z_R$ , and consequently to  $\omega$ . Therefore, the radiation intensity  $I(z)$  described in (5.2) and the power  $P(z)$ , which is emitted and then travels a distance  $z$  with the electron beam, tend to be directly proportional to the frequency, such that  $I(z) \propto \omega^2$ .

The current approximation is used to assess the diffraction effects on the Power Spectral Density (PSD) of the radiation output and its impact on the temporal pulse. This approach is implemented after the 1D simulation has finished and is not applied during the simulation process. Although this technique is moderately basic and cannot be relied upon to accurately represent a comprehensive 3D simulation of the FEL interaction, it offers an initial prediction of the potential outcomes.

The frequency spectrum of the scaled electric field  $A(\bar{z}_2)$  at a specific point in the undulator is described as  $\tilde{A}(\bar{\omega}) = |\mathcal{F}[A(\bar{z}_2)]|$ , where  $\mathcal{F}$  denotes the Fourier transform in  $\bar{z}_2$  with respect to  $\bar{\omega} = \omega/\omega_r$ . The scaled power spectral density (PSD) is defined as  $\tilde{P}(\bar{\omega}) = |\tilde{A}(\bar{\omega})|^2$ . The scaled PSD of the radiation, taking into account the diffractive effects during propagation, scales with  $\bar{\omega}^2$  as mentioned in equation (5.2). The spectrum, including 3D diffraction effects, is estimated as  $\tilde{P}_{3D}(\bar{\omega}) = |\tilde{A}_{3D}(\bar{\omega})|^2 = |\bar{\omega}\tilde{A}(\bar{\omega})|^2$ . The scaled intensity is then obtained using the inverse Fourier transform  $|A_{3D}(\bar{z}_2)|^2 = |\mathcal{F}^{-1}[\tilde{A}_{3D}(\bar{\omega})]|^2$ .

The 3D approximations are now shown as the radiation spike progresses through saturation in Figure 5.10 ( $\bar{z} = 200$  and 750) and Figure 5.11 ( $\bar{z} = 1200.5$  and 2156.5), for the scenario where  $4\pi\rho = 0.5$ . Due to the use of approximations, these plots cannot be expected to provide precise numerical estimates. Therefore, they have been scaled according to their peak values to facilitate a comparison of their temporal and spectral characteristics.

As shown in Figure 5.10a, at  $\bar{z} = 200$ , the system has entered the superradiant pulse regime, exhibiting similarities between the 3D approximation and the 1D result. The emission of lower frequencies appears to occur after the electrons pass through the first spike, approximately  $\bar{z}_2 \sim 1.5$ . This can also be deduced from the PSDs of  $\tilde{P}$  and  $\tilde{P}_{3D}$ , as well as from the electron behaviour shown in Figure 5.4a, where electron bunches are separated by distances greater than one radiation wavelength. Radiation emitted following the first spike therefore has a lower frequency, which, when reduced due to diffraction, is observed to be reduced  $\tilde{P}_{3D}$ , compared to the 1D case. The features of this superradiant pulse emission regime, as observed from the 3D spectrum, resemble the experimental findings of [80], suggesting that the approach to incorporate

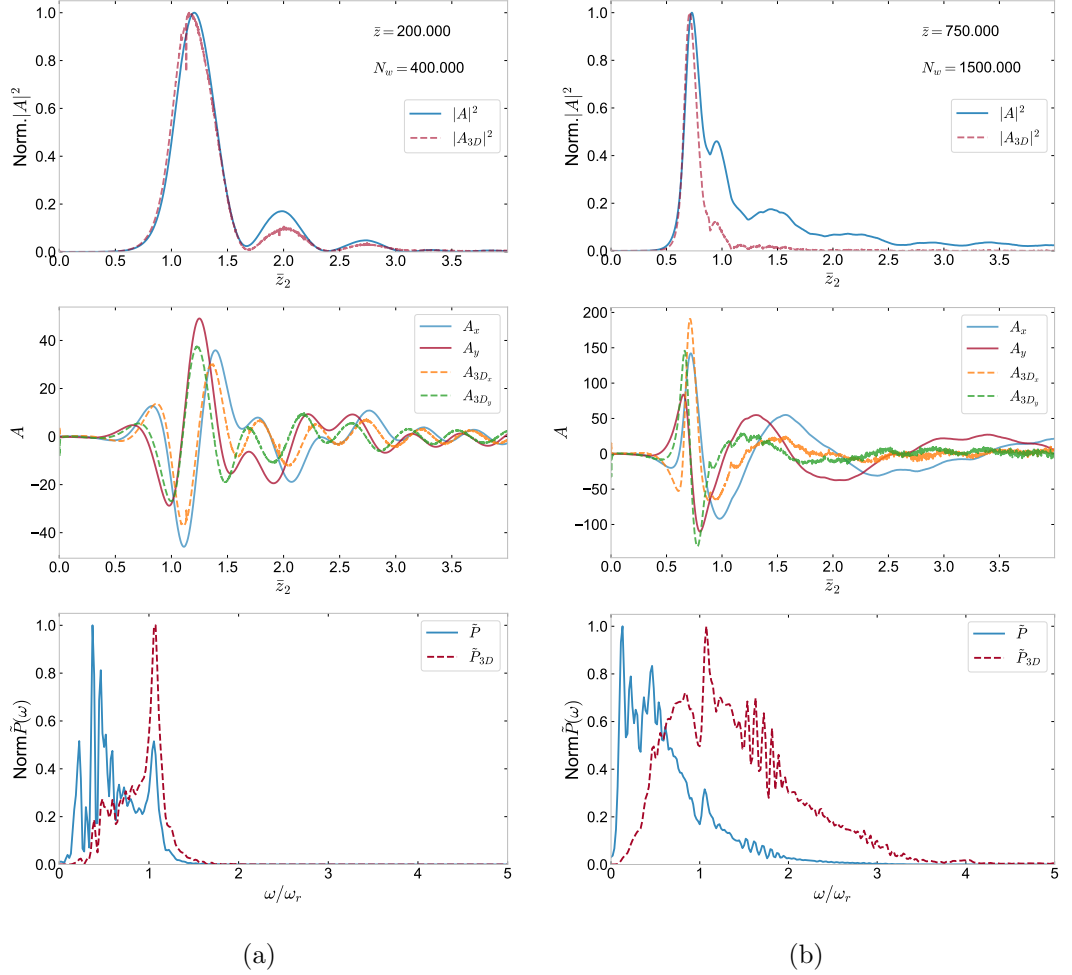


Figure 5.10: Comparison of 1D simulations with the 3D approximation for diffractive effects in the post-saturated superradiant regime for (a)  $\bar{z} = 200$  and (b)  $\bar{z} = 750$ . (Top) Normalised 1D scaled power  $|A|^2$  (solid blue line) and the 3D diffraction approximation  $|A_{3D}|^2$  (dashed red line). (Middle) Scaled 1D electric field components  $A_{x,y}$  (solid line) and the 3D approximation  $A_{3D_{x,y}}$  (dashed line). (Bottom) The 1D scaled Power Spectral Density  $\tilde{P}$  (solid line) and the 3D diffraction approximation  $\tilde{P}_{3D}$  (dashed line).

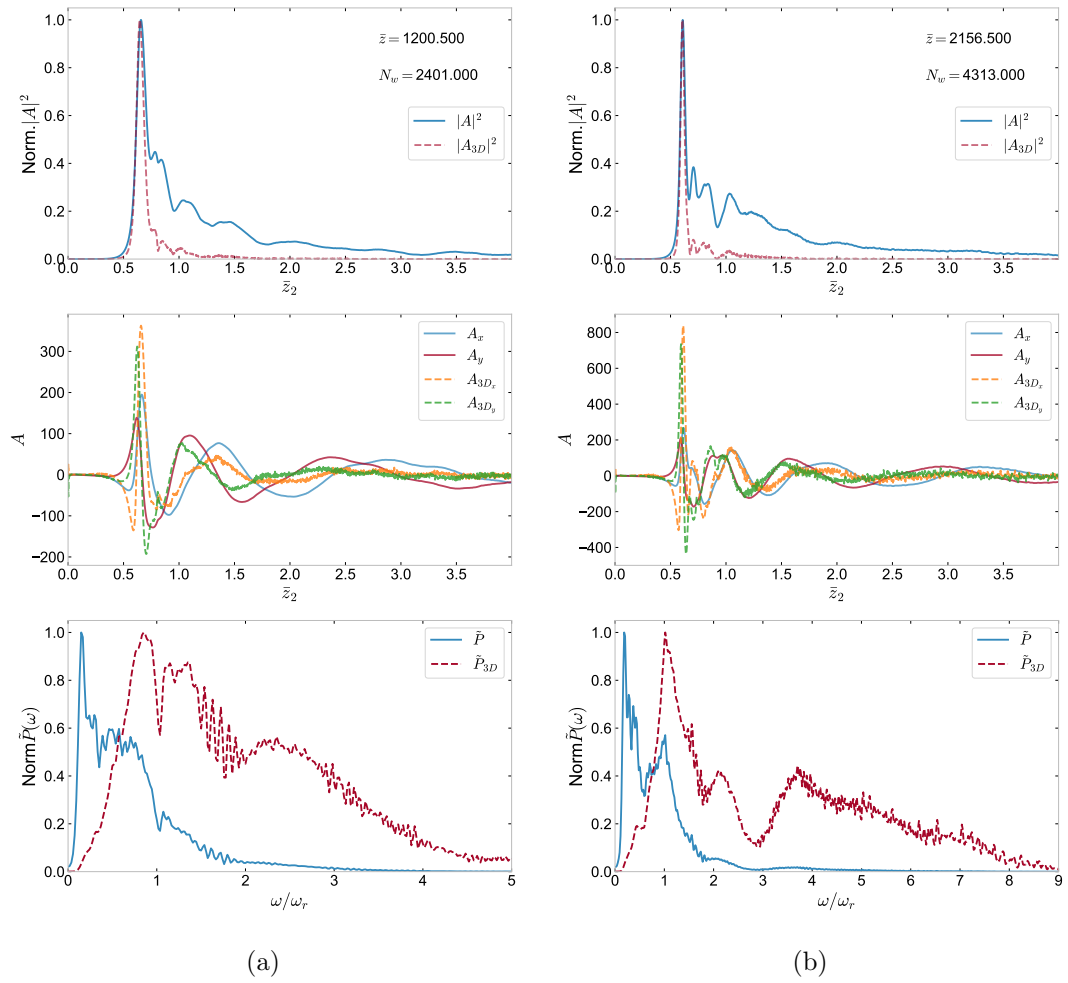


Figure 5.11: As figure 5.10 but for (a)  $\bar{z} = 1200.5$  and (b)  $\bar{z} = 2156.5$ .

3D diffractive effects discussed earlier is reasonable.

This behaviour is also demonstrated further in Figure 5.10b for  $\bar{z} = 750$  which shows that in the 3D approximation, the radiation pulse power following the first spike is reduced, as the lower frequencies emitted by the electrons following the spike diffract away. With a decrease in the radiation spike duration, there is an expansion of the spectrum towards higher frequencies. Consequently, the radiation field is seen to approach that of a single-cycle pulse.

The above diffraction behaviour extends significantly into the saturated phase of spike evolution, as illustrated in Figure 5.11, for  $\bar{z} = 1200.5$  and  $2156.5$ . Although there are minor variances in sub-pulse structure, the FWHM of the initial peak keeps its sub-resonant wavelength duration, supported by the broad spectral content at higher frequencies.

## 5.4 Conclusion

The simulations presented in this paper have provided the first detailed study of how high-power radiation spikes saturate in a FEL. While the simulations are in 1D, and the radiation spikes only interact with a beam of cold electrons, they have revealed at a fundamental level how a superradiant spike saturates, with peak powers orders of magnitude above the normal steady-state value. The saturation process involves the rapid loss of electron energy to the radiation field and their subsequent transit through the spike within one undulator period. The electrons therefore lose their energy to the spike at the sub-wavelength scale. This involves the emission of radiation across a broad range of frequencies well above that of the fundamental. It was also seen from the simulations that electrons that enter the spike with an absorptive phase may be rapidly accelerated to much higher energies of  $\sim 5$  times their initial energy. An examination of the simple scaling of the saturation process agreed well with the numerical results.

By applying a simplified scaling of radiation diffraction to the 1D radiation field, an estimate of the 3D spectral power of the field was made. This showed, and as observed from the field simulations, that the lower frequency radiation components were emitted after the electrons had passed through the spike and lost energy to it. The spectrum

was also similar to that observed in experiment [80].

Clearly, further research is required to model 3D effects in the unaveraged simulations. This can be expected to alter the detail of how the superradiant spiking develops. The 1D results presented, however, give a reasoned, consistent insight, analogous to the 1D description of the basic FEL interaction itself, into how the spiking saturation process develops.

While the above research will probably not be able to be applied at any FEL facilities in the near future, it does provide further understanding of the fundamental FEL process and may open up new areas of research.

## Chapter 6

# Conclusion and Future work

Several conclusions can be drawn from this work, and there are multiple steps for potential future development.

### **Conclusion:**

The convergence of FEL Puffin and OPC optical simulation codes marks a significant advancement in the field of FEL simulations, particularly for designs requiring optical components like cavity-based FEL oscillators. The development of conversion scripts has facilitated the radiation field transfer between these codes, enabling complex modelling of periodic modes in VUV-RAFEL designs. This innovation lays the basis for future ultra-short pulse, broadband simulations in cavity-based FELs, and opens the door to previously unexplored methodologies requiring unaveraged FEL and optics simulations.

The integration of Puffin and OPC simulation codes introduces a robust tool for examining cavity-based FELs at the sub-wavelength scale, inclusive of Coherent Spontaneous Emission (CSE) and cavity detuning effects. Our simulations, pioneering in their focus on sub-wavelength cavity detuning, revealed an unexpected steady-state lasing at the third harmonic. This finding highlights the potential of CSE, which has been shown to generate higher radiation powers than electron beam shot-noise, to enhance or substitute external lasers in seeded cavity FELs. The interchange of CSE

with sub-wavelength cavity detuning might stabilise or further enhance FEL output, particularly in longer wavelength sources where electron pulse current variations are more rapid.

Simulations using a Gaussian current profile electron bunch, dominated by shot-noise spontaneous emission, highlighted the role of sub-wavelength cavity detuning in harmonic lasing and validated its occurrence across different beam current shapes. These results suggest numbers of future investigation, including dynamic sub-wavelength cavity detuning via noise or adjustments, and the impact of crystal optics in shorter wavelength FEL designs. These potential studies suggest to reveal new opportunities and will be the focus of following research.

Our detailed study on high-power radiation spike saturation in FELs, despite being in 1D and involving a cold electron beam, offers fundamental insights into superradiant spike saturation. The simulations demonstrated that the saturation process involves rapid energy loss from electrons to the radiation field within one undulator period, leading to emission across a broad frequency range. Electrons entering the spike in an absorptive phase were accelerated to significantly higher energies, supporting our simplified scaling predictions of the saturation process.

By approximating radiation diffraction effects in a 1D field, we estimated the 3D spectral power, observing that lower frequency radiation components were emitted post energy transfer to the spike. This spectrum closely matched experimental observations, providing a foundational understanding of superradiant spike dynamics.

Future research must extend these 1D simulations to 3D to capture the detailed development of superradiant spiking. While instant practical applications at FEL facilities may be limited, the insights gained enhance our comprehension of the fundamental FEL process and pave the way for new research directions.

In summary, the combined utilisation of FEL Puffin and OPC codes has not only facilitated advanced FEL simulations but also revealed significant phenomena at sub-wavelength scales and in superradiant spike saturation. These findings contribute significantly to the field of FEL research, suggesting new methodologies and potential applications, and setting the stage for further explorations into the complex dynamics

of FEL systems.

## Future Development Plan

The conjunction of the FEL Puffin and OPC optical simulation codes presents several opportunities for advancing FEL simulation methodologies. The next steps in this development plan include:

- **Ultra short-pulse simulations:** Developing on the success of modelling periodic modes in VUV-RAFEL designs, future work will focus on developing ultra-short pulse (few-wavelength) broadband simulations in cavity-based FELs. This will involve enhancing the conversion scripts and optimising the interaction between the FEL Puffin and OPC codes for these specific simulations.
- **Exploring unaveraged FEL and optics simulations:** With the capability to transfer radiation fields between the simulation codes, future research should explore other methods that require the use of unaveraged FEL and optics simulations. This could involve investigating new designs and configurations for FEL oscillators and other related systems.
- **Validation and benchmarking:** To ensure the accuracy and reliability of these simulations, extensive validation and benchmarking against experimental data and other simulation codes will be necessary. This will help in refining the models and identifying any inconsistencies that need to be addressed.

The coupled Puffin and OPC FEL simulation codes offer a novel approach to simulating cavity-based FELs at the sub-wavelength scale. Future development plans in this area include:

- **Dynamic cavity detuning studies:** Developing on the initial findings, future research will focus on the dynamics of sub-wavelength cavity detuning. This includes investigating the effects of cavity length noise due to vibrations and exploring dynamic adjustments to enhance FEL output.

- **Utilisation of Coherent Spontaneous Emission (CSE):** Further studies will examine the potential of CSE to enhance or replace external lasers in seeded cavity FELs. This will involve detailed simulations of different electron beam current shapes and the effects of CSE in various configurations.
- **Crystal optics in shorter wavelength FEL designs:** Research will extend to the use of crystal optics in shorter wavelength FEL designs, comparing the results with those obtained from sub-wavelength changes in cavity dimensions. This will provide insights into the feasibility and advantages of using crystal optics in these systems.
- **Experimental collaboration:** Collaborating with experimentalists to test these simulation predictions in practical settings will be crucial. This will help in validating the theoretical models and understanding the practical challenges and benefits of sub-wavelength cavity detuning and CSE in FELs.

The detailed study of high-power radiation spike saturation in FELs has opened up several opportunities for future research. The development plan includes:

- **3D Simulations of superradiant spiking:** Extending the current 1D simulations to 3D will be a primary focus. This will involve developing and implementing 3D models that can accurately capture the detailed dynamics of superradiant spike saturation.
- **Advanced scaling techniques:** Further refining the scaling techniques used to estimate 3D spectral power from 1D simulations will be necessary. This will involve integrating more complex diffraction effects and validating these models against experimental data.
- **Exploration of broader frequency emission:** Investigating the emission of radiation across a broader range of frequencies, especially those well above the fundamental, will be crucial. This will include studying the conditions under which these emissions occur and their potential applications.

- **Collaboration and application:** Collaborating with experimentalists and applying these insights to practical FEL systems will help in understanding the feasibility and impact of these findings. This will also involve exploring potential new areas of research that these fundamental insights might open up.
- **Integration with other FEL technologies:** Integrating the insights gained from superradiant spike saturation studies with other FEL technologies and designs will be important. This could lead to the development of new FEL configurations that influence the unique properties of superradiant spiking for improved performance.

# Appendix A

## Pulse saturation scaling

### A.1 Pulse saturation scaling

The equations governing the  $j$ th electron's motion in the scaled radiation frame of reference  $\bar{z}_2$  may be written as [10]:

$$\begin{aligned}\frac{d\bar{z}_{2j}}{d\bar{z}} &= 1 - 2\rho p_j \\ \frac{dp_j}{d\bar{z}} &= -2A(\bar{z}_2) \cos\left(\frac{\bar{z} - \bar{z}_{2j}}{2\rho}\right)\end{aligned}$$

where the field  $A(\bar{z}_2)$  is assumed constant in  $\bar{z}$  and describes a short, high power radiation pulse (spike) of peak power  $A_p$  into which the electron will propagate. Assume that the electron starts its interaction with the pulse at resonance,  $p_j = 0$ , and at the phase of maximum rate of energy loss where  $\cos((\bar{z} - \bar{z}_{2j})/2\rho) = 1$ , then the incremental change in  $p_j$  for a propagation distance  $\Delta\bar{z}$  may be written as:

$$\Delta p_j \approx -\frac{A_p}{2} \Delta\bar{z}, \tag{A.1}$$

where it is assumed  $A \approx A_p/2$  over  $\Delta\bar{z}$ .

Similarly, the change in electron position  $\Delta\bar{z}_{2j}$  due to its interaction with the radiation field (i.e. not including the resonant drift of  $\Delta\bar{z}$  in the radiation frame of reference) may be approximated as:

$$\Delta\bar{z}_{2j} = -2\rho p_j \Delta\bar{z}, \tag{A.2}$$

## Appendix A. Pulse saturation scaling

and assuming  $p_j \approx \Delta p_j/2 = -A_p \Delta \bar{z}/4$ , then:

$$\Delta \bar{z}_{2j} = \frac{\rho A_p}{2} \Delta \bar{z}^2 \quad (\text{A.3})$$

Saturation of the electron motion in the radiation pulse is now defined as when the electron propagates an extra half a radiation wavelength through the radiation field, in addition to its drift in the radiation frame of  $\bar{z}_2$ , in half of a wiggler period. This may be written as  $\Delta \bar{z}_{2j} = \Delta \bar{z} = 2\pi\rho$ , so that for saturation:

$$2\pi\rho \approx \frac{\rho A_p}{2} (2\pi\rho)^2 \quad (\text{A.4})$$

$$\Rightarrow |A_p|^2 \approx \frac{1}{\pi^2 \rho^4} \quad (\text{A.5})$$

The pulse duration of the first peak  $\tau_p$ , is assumed to scale as the radiation wavelength, which in units of  $\bar{z}_2$  is  $\tau_p = f \times 4\pi\rho$  where  $f$  is a fractional factor. The scaled energy in the first peak at saturation  $\varepsilon_p$  is then:

$$\varepsilon_p \approx \tau_p |A_p|^2 \approx \frac{4f}{\pi \rho^3} \quad (\text{A.6})$$

# Appendix B

## Conference papers

- P. Pongchalee and B.W.J. McNeil, “Unaveraged Simulation of a Regenerative Amplifier Free Electron Laser”, in Proc. FEL’19, Hamburg, Germany, Aug. 2019, pp. 106-109. doi:10.18429/JACoW-FEL2019-TUP026
- P. Pongchalee and B.W.J. McNeil, “Modelling of Sub-Wavelength Effects in a FEL Oscillator”, in Proc. FEL2022, Trieste, Aug. 2022, pp. 68-71. doi:10.18429/JACoW-FEL2022-MOP32

# Appendix C

## Peer-review papers

- P. Pongchalee and B.W.J. McNeil, “Sub-wavelength effects in a free electron laser oscillator,” *Opt. Express* 31, 26673 (2023)
- P. Pongchalee and B.W.J. McNeil, “Unaveraged simulations of a cavity based free electron laser,” *Results in Physics* 57, 107390 (2024)
- P. Pongchalee and B.W.J. McNeil, “Superradiant pulse saturation in a Free Electron Laser,” *Results in Physics* 60, 107673 (2024)

# Appendix D

## Code snippets

### D.1 Puffin to OPC

```
1 # -*- coding: utf-8 -*-
2 """
3 Created first version on Wed May 15 10:38:37 2019
4
5 @author: Racha Pongchalee
6 """
7 # noted only x polarization of the Aperp field will be converted
8   to OPC format
9
10 import numpy as np
11 import time
12 import tables, gc
13 from scipy.signal import hilbert
14 from scipy.fftpack import next_fast_len
15 import sys
16
17 filename = sys.argv[1] # retrieve the base name
18 # filename = "D://Puffin_results//New_RAFEL//rafel_aperp_150"
19 h5name = filename + ".h5"
20 binname_x = filename + "_x.dfl"
21 paramname_x = filename + "_x.param"
22 binname_y = filename + "_y.dfl"
```

## Appendix D. Code snippets

```
21 paramname_y = filename + "_y.param"
22
23 print ("Reading aperp file ..." + h5name + "\n")
24 h5f = tables.open_file(h5name, mode='r')
25
26 # Read the HDF5 file (Puffin_aperp file)
27 aperps = h5f.root.aperp.read()
28 Aperp_x = np.array(aperps[0]) # x-polarised field
29 Aperp_y = np.array(aperps[1]) # y-polarised field
30 print ("Getting file attributes ... \n")
31 # Dictionary to store the attributes
32 runInfo_dict = {}
33
34 # Loop through attributes and store them in the dictionary
35 for attr in h5f.root.runInfo._v_attrs._f_list():
36     runInfo_dict[attr] = getattr(h5f.root.runInfo._v_attrs, attr)
37
38 wavelength = runInfo_dict.get('lambda_r', None)
39 nx = runInfo_dict.get('nX', None)
40 ny = runInfo_dict.get('nY', None)
41 nz = runInfo_dict.get('nZ2', None)
42 Lc = runInfo_dict.get('Lc', None)
43 Lg = runInfo_dict.get('Lg', None)
44 rho = runInfo_dict.get('rho', None)
45 meshsizeX = runInfo_dict.get('sLengthOfElmX', None)
46 meshsizeY = runInfo_dict.get('sLengthOfElmY', None)
47 meshsizeZ2 = runInfo_dict.get('sLengthOfElmZ2', None)
48 meshsizeXSI = meshsizeX*np.sqrt(Lc*Lg)
49 meshsizeYSI = meshsizeY*np.sqrt(Lc*Lg)
50 meshsizeZSI = meshsizeZ2*Lc
51 zsep = meshsizeZSI/wavelength
52
53 print("Getting the complex envelope from x-field ...")
54 print("Processing the Hilbert transform ..")
```

## Appendix D. Code snippets

```
55 start = time.time()
56 fast_len = next_fast_len(len(Aperp_x))
57 Aperp_x_complex = hilbert(Aperp_x, fast_len,
    0)[:len(Aperp_x),:,:]
58 # Aperp_x_complex = np.real(Aperp_x_complex) -
    1j*np.imag(Aperp_x_complex)
59 end = time.time()
60
61 # Aperp_x_hilbert = Hilbertfromfft(Aperp_x)
62 print("Hilbert transform x ... DONE ... " + str(end - start) +
    " seconds" + "\n")
63 del(Aperp_x)
64
65 start = time.time()
66 fast_len = next_fast_len(len(Aperp_y))
67 Aperp_y_complex = hilbert(Aperp_y, fast_len,
    0)[:len(Aperp_y),:,:]
68 # Aperp_y_complex = np.real(Aperp_y_complex) -
    1j*np.imag(Aperp_y_complex)
69 end = time.time()
70
71 # Aperp_x_hilbert = Hilbertfromfft(Aperp_x)
72 print("Hilbert transform y ... DONE ... " + str(end - start) +
    " seconds" + "\n")
73 del(Aperp_y)
74 h5f.close()
75 gc.collect()
76
77 def interleave_real_imag(complex_array):
78     stacked = np.dstack((complex_array.real,
        complex_array.imag)) # note the "negative" on imaginary
        part
79     return stacked.flatten()
80
```

## Appendix D. Code snippets

```
81 def interArray(A, B):
82     C = np.empty((A.size + B.size,), dtype=np.float64)
83     C[0::2] = A
84     C[1::2] = B
85     return C
86
87 print("Re-ordering/correcting the phase of the complex field
      into the OPC format")
88 start = time.time()
89 bin_x = np.reshape(Aperp_x_complex, nx*ny*nz)
90 bin_x = interArray(np.real(bin_x), -np.imag(bin_x)) # note: the
      "negative" sign must be assigned to the imaginary part !!!
91 # bin_x = interleave_real_imag(Aperp_x_complex)
92 del(Aperp_x_complex)
93 end = time.time()
94
95 print("Re-order the complex field x ... DONE ... " + str(end -
      start) + " seconds" + "\n")
96
97 start = time.time()
98 bin_y = np.reshape(Aperp_y_complex, nx*ny*nz)
99 bin_y = interArray(np.real(bin_y), -np.imag(bin_y)) # note: the
      "negative" sign must be assigned to the imaginary part !!!
100 # bin_y = interleave_real_imag(Aperp_y_complex)
101 del(Aperp_y_complex)
102 end = time.time()
103 print("Re-order the complex field y ... DONE ... " + str(end -
      start) + " seconds" + "\n")
104 gc.collect()
105
106 print("Saving x-field to binary file ..." + " binary data length
      = " + str(len(bin_x)))
107 start = time.time()
108 with open(binname_x, "wb") as f:
```

## Appendix D. Code snippets

```
109         bin_x.tofile(f)
110 del(bin_x)
111 f.close()
112 end = time.time()
113 print("Save file x ... DONE ... " + str(end - start) + "
      seconds" + "\n")
114
115 gc.collect()
116
117 print("Saving y-field to binary file ..." + " binary data length
      = " + str(len(bin_y)))
118 start = time.time()
119 with open(binname_y, "wb") as f:
120     bin_y.tofile(f)
121 del(bin_y)
122 f.close()
123 end = time.time()
124 print("Save file y ... DONE ... " + str(end - start) + "
      seconds" + "\n")
125
126 # save binary file
127 # write the parameter file for physical interpretation
128
129 optics_params = {
130     'nslices': nz,
131     'zsep': zsep,
132     'mesh_x': 1 if nx-1 == 0 else meshsizeXSI,
133     'mesh_y': 1 if nx-1 == 0 else meshsizeYSI,
134     'npoints_x': nx,
135     'npoints_y': ny,
136     'Mx': 1,
137     'My': 1,
138     'lambda': wavelength,
139     'field_next': 'none'
```

## Appendix D. Code snippets

```
140 }
141
142 def write_namelist_to_file(file_obj, namelist_name, params_dict):
143     file_obj.write(" $" + namelist_name + "\n")
144     for key, value in params_dict.items():
145         # Check and decode bytes to string
146         if isinstance(value, bytes):
147             value = value.decode('utf-8')
148
149         file_obj.write(" " + key + " = " + str(value) + "\n")
150         # print(f" {key} = {value}")
151     file_obj.write(" /\n")
152
153 print("writing OPC parameter file x ... ")
154 with open(paramname_x, 'w') as param_x:
155     write_namelist_to_file(param_x, 'optics', optics_params)
156     write_namelist_to_file(param_x, 'runInfo', runInfo_dict)
157
158 print("writing OPC parameter file y ... ")
159 with open(paramname_y, 'w') as param_y:
160     write_namelist_to_file(param_y, 'optics', optics_params)
161     write_namelist_to_file(param_y, 'runInfo', runInfo_dict)
162
163 print("DONE\n")
```

Listing D.1: Python code for Puffin to OPC field conversion.

## D.2 OPC to Puffin

```
1 # -*- coding: utf-8 -*-
2 """
3 Latest update on: 12/09/2024
4
5 @author: P. Pongchalee
6 """
7
8 import numpy as np
9 import sys, tables, gc
10
11 # usage: python /code-directory/OPC-to-Puffin_xy.py "fileprefix"
12
13 fx = sys.argv[1] + "_x.dfl"
14 px = sys.argv[1] + "_x.param"
15 fy = sys.argv[1] + "_y.dfl"
16 py = sys.argv[1] + "_y.param"
17 h5name = sys.argv[1] + ".h5"
18
19 def read_namelist_from_file(file_obj):
20     result = {}
21     current_section = None
22     for line in file_obj:
23         line = line.strip()
24         if line.startswith("$"):
25             current_section = line[1:]
26             result[current_section] = {}
27         elif line == "/":
28             current_section = None
29         elif current_section:
30             key, value = line.split("=", 1)
31             key = key.strip()
32             value = value.strip()
```

## Appendix D. Code snippets

```
33         if value.startswith("'") and value.endswith("'"):
34             value = value[1:-1]
35         else:
36             try:
37                 # First, try to convert the value to a float
38                 value_float = float(value)
39                 # If the float value is an integer, convert
40                 # it to int
41                 if value_float.is_integer():
42                     value = int(value_float)
43                 else:
44                     value = value_float
45             except ValueError:
46                 pass
47             result[current_section][key] = value
48         return result
49
50 print ("Reading parameter from .param file ..." + px + "\n")
51 with open(px, "r") as file:
52     dictionaries = read_namelist_from_file(file)
53     optics_dict = dictionaries['optics']
54     runInfo_dict = dictionaries['runInfo']
55
56     Mx = optics_dict.get('Mx', None)
57     My = optics_dict.get('My', None)
58
59     mesh_x = optics_dict.get('mesh_x', None)
60     mesh_y = optics_dict.get('mesh_y', None)
61
62     nslices = optics_dict.get('nslices', None)
63     npoints_x = optics_dict.get('npoints_x', None)
64     npoints_y = optics_dict.get('npoints_y', None)
```

## Appendix D. Code snippets

```
65     # scaling the grid size of puffin field when running with
        OPC magnification factor in Modified Fresnel Integral
66     # runInfo_dict['sLengthOfElmX'] = Mx *
        runInfo_dict.get('sLengthOfElmX', None)
67     # runInfo_dict['sLengthOfElmY'] = My *
        runInfo_dict.get('sLengthOfElmY', None)
68     SUScale = 1/np.sqrt(runInfo_dict.get('Lg', None) *
        runInfo_dict.get('Lc', None))
69     runInfo_dict['sLengthOfElmX'] = mesh_x * SUScale
70     runInfo_dict['sLengthOfElmY'] = mesh_y * SUScale
71
72     print ("Reading binary file_x ..." + fx + "\n")
73     field_x = (1/np.sqrt(Mx*My))*np.fromfile(fx, dtype='f8') # don't
        need to open the binary file numpy will haddle this
74     print ("Reading binary file_y ..." + fy + "\n")
75     field_y = np.fromfile(fy, dtype='f8') # don't need to open the
        binary file numpy will haddle this
76
77     print ("Converting to Puffin format xy ...\n")
78     Aperp_x = (1/np.sqrt(Mx*My))*field_x[0:][::2] # even index
        represents real number in OPC format
79     Aperp_y = (1/np.sqrt(Mx*My))*field_y[0:][::2] # even index
        represents real number in OPC format
80     aperp = np.concatenate((Aperp_x,Aperp_y))
81     aperp = np.reshape(aperp, (2, int(nslices), int(npoints_y),
        int(npoints_x)))
82
83     del(Aperp_x,Aperp_y)
84     gc.collect()
85
86     print ("Saving to h5 file ...\n")
87     a = tables.Float64Atom()
88     shape = (2, nslices, npoints_y, npoints_x)
89     with tables.open_file(h5name, 'w') as hf:
```

## Appendix D. Code snippets

```
90     saperp = hf.create_array('/', 'aperp', obj = aperp)
91     saperp.attrs['iCsteps'] = 0
92     # Create a group for runInfo
93     runInfo_group = hf.create_group('/', 'runInfo', 'Run
          Information')
94
95     # Add each key-value pair from the runInfo dictionary as an
          attribute to the runInfo group
96     for key, value in runInfo_dict.items():
97         runInfo_group._v_attrs[key] = value
98
99     print ("Saving done ...." + h5name + "\n" )
```

Listing D.2: Python code for OPC to Puffin field conversion.

# Bibliography

- [1] Hazim Al-Abawi, Frederic A. Hoff, Gerard T. Moore, and Marlan O. Scully. Coherent transients in the free-electron laser: Laser lethargy and coherence brightening. *Optics Communications*, 30(2):235–238, 1979.
- [2] E Allaria, D Castronovo, P Cinquegrana, P Craievich, Massimo Dal Forno, MB Danailov, G D’Auria, A Demidovich, G De Ninno, S Di Mitri, et al. Two-stage seeded soft-x-ray free-electron laser. *Nature Photonics*, 7(11):913–918, 2013.
- [3] Massimo Altarelli, Reinhard Brinkmann, and Majed Chergui. The european x-ray free-electron laser. technical design report, Jul 2007.
- [4] A. Aquila, A. Barty, C. Bostedt, S. Boutet, G. Carini, D. dePonte, P. Drell, S. Doniach, K. H. Downing, T. Earnest, H. Elmlund, V. Elser, M. Gühr, J. Hajdu, J. Hastings, S. P. Hau-Riege, Z. Huang, E. E. Lattman, F. R. N. C. Maia, S. Marchesini, A. Ourmazd, C. Pellegrini, R. Santra, I. Schlichting, C. Schroer, J. C. H. Spence, I. A. Vartanyants, S. Wakatsuki, W. I. Weis, and G. J. Williams. The linac coherent light source single particle imaging road map. *Structural Dynamics*, 2(4):041701, 04 2015.
- [5] R.J. Bakker, D.A. Jaroszynski, A.F.G. van der Meer, D. Oepts, and P.W. van Amersfoort. Short-pulse effects in a free-electron laser. *IEEE Journal of Quantum Electronics*, 30(7):1635–1644, 1994.
- [6] George C Baldwin and Donald W Kerst. Origin of synchrotron radiation. *Physics Today*, 28(1):9–11, 1975.

## Bibliography

- [7] Anton Barty. Single molecule imaging using x-ray free electron lasers. *Current opinion in structural biology*, 40:186–194, 2016.
- [8] Stephen V Benson and John MJ Madey. Demonstration of harmonic lasing in a free-electron laser. *Physical Review A*, 39(3):1579, 1989.
- [9] R. Bonifacio and F. Casagrande. The superradiant regime of a free electron laser. *Nuclear Instruments and Methods in Physics Research Section A: Accelerators, Spectrometers, Detectors and Associated Equipment*, 239(1):36–42, 1985.
- [10] R. Bonifacio, B. W. J. McNeil, and P. Pierini. Superradiance in the high-gain free-electron laser. *Phys. Rev. A*, 40:4467–4475, Oct 1989.
- [11] R. Bonifacio, C. Pellegrini, and L.M. Narducci. Collective instabilities and high-gain regime in a free electron laser. *Optics Communications*, 50(6):373–378, 1984.
- [12] Rodolfo Bonifacio, Cesare Maroli, and Nicola Piovella. Slippage and superradiance in the high-gain fel: Linear theory. *Optics communications*, 68(5):369–374, 1988.
- [13] L.T. Campbell, H.P. Freund, J.R. Henderson, B.W.J. McNeil, P. Traczykowski, and P.J.M. van der Slot. Analysis of ultra-short bunches in free-electron lasers. *New Journal of Physics*, 22, 2020.
- [14] LT Campbell and BWJ McNeil. Puffin: A three dimensional, unaveraged free electron laser simulation code. *Physics of Plasmas*, 19(9):093119, 2012.
- [15] LT Campbell and BWJ McNeil. Puffin: Parallel unaveraged fel integrator. <https://github.com/UKFELs/Puffin>, 2012.
- [16] L.T. Campbell, B.W.J. McNeil, J.D.A. Smith, and P.T. Traczykowski. An Updated Description of the FEL Simulation Code Puffin. In *Proc. 9th International Particle Accelerator Conference (IPAC'18), Vancouver, BC, Canada, April 29-May 4, 2018*, pages 4579–4582. JACoW Publishing, 2018.
- [17] Alexander Wu Chao, Maury Tigner, Hans Weise, and Frank Zimmermann. *Handbook of accelerator physics and engineering*. World scientific, 2023.

## Bibliography

- [18] Henry N Chapman. X-ray imaging beyond the limits. *Nature materials*, 8(4):299–301, 2009.
- [19] JA Clarke and EA Seddon. The conceptual design of 4gls at daresbury laboratory. In *Proc. EPAC*, page 181, 2006.
- [20] Jacques-Philippe Colletier, Michael R Sawaya, Mari Gingery, Jose A Rodriguez, Duilio Cascio, Aaron S Brewster, Tara Michels-Clark, Robert H Hice, Nicolas Coquelle, Sébastien Boutet, et al. De novo phasing with x-ray laser reveals mosquito larvicide binab structure. *Nature*, 539(7627):43–47, 2016.
- [21] William B. Colson and Alberto Renieri. Pulse propagation in free electron lasers. *Le Journal De Physique Colloques*, 44, 1983.
- [22] D. A. G. Deacon, L. R. Elias, J. M. J. Madey, G. J. Ramian, H. A. Schwettman, and T. I. Smith. First operation of a free-electron laser. *Phys. Rev. Lett.*, 38:892–894, Apr 1977.
- [23] Winfried Decking, S Abeghyan, P Abramian, A Abramsky, A Aguirre, C Albrecht, P Alou, M Altarelli, P Altmann, K Amyan, et al. A mhz-repetition-rate hard x-ray free-electron laser driven by a superconducting linear accelerator. *Nature photonics*, 14(6):391–397, 2020.
- [24] D.J. Dunning, B.W.J. McNeil, and N.R. Thompson. Short wavelength regenerative amplifier free electron lasers. *Nuclear Instruments and Methods in Physics Research Section A: Accelerators, Spectrometers, Detectors and Associated Equipment*, 593(1):116–119, 2008. FEL Frontiers 2007.
- [25] Paul Emma, R Akre, J Arthur, R Bionta, C Bostedt, J Bozek, A Brachmann, P Bucksbaum, Ryan Coffee, F-J Decker, et al. First lasing and operation of an ångstrom-wavelength free-electron laser. *nature photonics*, 4(9):641–647, 2010.
- [26] William M. Fawley. A user manual for ginger and its post-processor xplotgin. Technical report, Lawrence Berkeley National Lab. (LBNL), Berkeley, CA (United States), 2002.

## Bibliography

- [27] Ryoichi Hajima and Ryoji Nagai. Generating carrier-envelope-phase stabilized few-cycle pulses from a free-electron laser oscillator. *Physical Review Letters*, 119(20):204802, 2017.
- [28] Max F Hantke, Dirk Hasse, Filipe RNC Maia, Tomas Ekeberg, Katja John, Martin Svenda, N Duane Loh, Andrew V Martin, Nicusor Timneanu, Daniel SD Larsson, et al. High-throughput imaging of heterogeneous cell organelles with an x-ray laser. *Nature Photonics*, 8(12):943–949, 2014.
- [29] Mark A Heald and Jerry B Marion. *Classical electromagnetic radiation*. Courier Corporation, 2012.
- [30] James Robert Henderson, Brian McNeil, and Lawrence Campbell. The implementation of 3d undulator fields in the unaveraged fel simulation code puffin. In *36th International Free Electron Laser Conference: FEL 2014*, page 416, 2015.
- [31] JG Karssenbergh, Petrus JM van der Slot, and IV Volokhine. Opc: Optical propagation code. <https://gitlab.utwente.nl/tnw/ap/lpno/public-projects/Physics-OPC>, 2006.
- [32] JG Karssenbergh, Petrus JM van der Slot, IV Volokhine, Jeroen WJ Verschuur, and K-J Boller. Modeling paraxial wave propagation in free-electron laser oscillators. *Journal of applied physics*, 100(9):093106, 2006.
- [33] Stephan Kassemeyer, Jan Steinbrener, Lukas Lomb, Elisabeth Hartmann, Andrew Aquila, Anton Barty, Andrew V Martin, Christina Y Hampton, Saša Bajt, Miriam Barthelmess, et al. Femtosecond free-electron laser x-ray diffraction data sets for algorithm development. *Optics Express*, 20(4):4149–4158, 2012.
- [34] R. Kiessling, W. B. Colson, S. Gewinner, W. Schöllkopf, M. Wolf, and A. Paarmann. Femtosecond single-shot timing and direct observation of subpulse formation in an infrared free-electron laser. *Phys. Rev. Accel. Beams*, 21:080702, Aug 2018.

## Bibliography

- [35] Matteo Levantino, Briony A Yorke, Diana CF Monteiro, Marco Cammarata, and Arwen R Pearson. Using synchrotrons and xfels for time-resolved x-ray crystallography and solution scattering experiments on biomolecules. *Current opinion in structural biology*, 35:41–48, 2015.
- [36] Yi-Wen Liu. Hilbert transform and applications. In Salih Mohammed Salih, editor, *Fourier Transform*, chapter 12, pages 291–300. IntechOpen, Rijeka, 2012.
- [37] Artem Y Lyubimov, Monarin Uervirojnangkoorn, Oliver B Zeldin, Qiangjun Zhou, Minglei Zhao, Aaron S Brewster, Tara Michels-Clark, James M Holton, Nicholas K Sauter, William I Weis, et al. Advances in x-ray free electron laser (xfel) diffraction data processing applied to the crystal structure of the synaptotagmin-1/snare complex. *Elife*, 5:e18740, 2016.
- [38] B. W. J. McNeil, M. W. Poole, and G. R. M. Robb. Unified model of electron beam shot noise and coherent spontaneous emission in the helical wiggler free electron laser. *Phys. Rev. ST Accel. Beams*, 6:070701, Jul 2003.
- [39] Brian WJ McNeil, GRM Robb, and MW Poole. An improved 1-d model for ultra high power radiation pulse propagation in the helical wiggler free electron laser. In *Proceedings of the 2003 Particle Accelerator Conference*, volume 2, pages 953–955. IEEE, 2003.
- [40] Brian WJ McNeil and Neil R Thompson. X-ray free-electron lasers. *Nature photonics*, 4(12):814–821, 2010.
- [41] B.W.J. McNeil. A simple model of the free-electron-laser oscillator from low into high gain. *Nuclear Instruments and Methods in Physics Research Section A: Accelerators, Spectrometers, Detectors and Associated Equipment*, 296(1):388–393, 1990.
- [42] BWJ McNeil and R Bonifacio. Slippage and superradiance in the high-gain fel. *Nucl. Inst. Meth. Phys. Res.*, A272(1-2):280–288, 1988.

## Bibliography

- [43] BWJ McNeil, GRM Robb, and DA Jaroszynski. Self-amplification of coherent spontaneous emission in the free electron laser. *Optics communications*, 165(1-3):65–70, 1999.
- [44] B.W.J. McNeil, N.R. Thompson, D.J. Dunning, JG Karssenbergh, Petrus JM van der Slot, and K-J Boller. A design for the generation of temporally-coherent radiation pulses in the vuv and beyond by a self-seeding high-gain free electron laser amplifier. *New Journal of Physics*, 9(7):239, jul 2007.
- [45] Stephen Val Milton, E Gluskin, ND Arnold, C Benson, W Berg, SG Biedron, M Borland, Y-C Chae, RJ Dejus, PK Den Hartog, et al. Exponential gain and saturation of a self-amplified spontaneous emission free-electron laser. *Science*, 292(5524):2037–2041, 2001.
- [46] George R Neil. Fel oscillators. In *Proceedings of the 2003 Particle Accelerator Conference*, volume 1, pages 181–185. IEEE, 2003.
- [47] Richard Neutze, Remco Wouts, David Van der Spoel, Edgar Weckert, and Janos Hajdu. Potential for biomolecular imaging with femtosecond x-ray pulses. *Nature*, 406(6797):752–757, 2000.
- [48] Dinh C. Nguyen, Richard L. Sheffield, Clifford M. Fortgang, John C. Goldstein, John M. Kinross-Wright, and Nizar A. Ebrahim. First lasing of the regenerative amplifier fel. *Nuclear Instruments and Methods in Physics Research Section A: Accelerators, Spectrometers, Detectors and Associated Equipment*, 429(1):125–130, 1999.
- [49] Dinh C Nguyen, RL Sheffield, CM Fortgang, JM Kinross-Wright, NA Ebrahim, and John C Goldstein. A high-power compact regenerative amplifier fel. In *Proceedings of the 1997 Particle Accelerator Conference (Cat. No. 97CH36167)*, volume 1, pages 897–899. IEEE, 1997.
- [50] Hideo Onuki and Pascal Elleaume. *Undulators, wigglers and their applications*. CRC Press, 2002.

## Bibliography

- [51] N. Piovella, P. Chaix, G. Shvets, and D. A. Jaroszynski. Analytical theory of short-pulse free-electron laser oscillators. *Phys. Rev. E*, 52:5470–5486, Nov 1995.
- [52] Nicola Piovella. A hyperbolic secant solution for the superradiance in free electron lasers. *Optics communications*, 83(1-2):92–96, 1991.
- [53] Nicola Piovella and Luca Volpe. A review of high-gain free-electron laser theory. *Atoms*, 9(2), 2021.
- [54] Nicola Piovella and Luca Volpe. A review of high-gain free-electron laser theory. *Atoms*, 9(2):28, 2021.
- [55] P Pongchalee. Conversion scripts between puffin and opc field formats. <https://github.com/UKFELs/Puffin-OPC>, 2023.
- [56] P. Pongchalee and B.W.J. McNeil. A video of the full superradiant spike evolution for  $4\pi\rho = 1$ . <https://doi.org/10.15129/60af5807-790e-4a97-9a4b-b0861d8c5fe8>, 2024.
- [57] P. Pongchalee and B.W.J. McNeil. A video of the spike evolution for  $\bar{z} = 100$  and  $4\pi\rho = 1$ . <https://ars.els-cdn.com/content/image/1-s2.0-S2211379724003565-mm3.mp4>, 2024.
- [58] P. Pongchalee and B.W.J. McNeil. A video of the spike evolution for  $\bar{z} = 1100$  and  $4\pi\rho = 1$ . <https://ars.els-cdn.com/content/image/1-s2.0-S2211379724003565-mm7.mp4>, 2024.
- [59] P. Pongchalee and B.W.J. McNeil. A video of the spike evolution for  $\bar{z} = 200$  and  $4\pi\rho = 1$ . <https://ars.els-cdn.com/content/image/1-s2.0-S2211379724003565-mm4.mp4>, 2024.
- [60] P. Pongchalee and B.W.J. McNeil. A video of the spike evolution for  $\bar{z} = 40$  and  $4\pi\rho = 1$ . <https://ars.els-cdn.com/content/image/1-s2.0-S2211379724003565-mm2.mp4>, 2024.

## Bibliography

- [61] P. Pongchalee and B.W.J. McNeil. A video of the spike evolution for  $\bar{z} = 400$  and  $4\pi\rho = 1$ . <https://ars.els-cdn.com/content/image/1-s2.0-S2211379724003565-mmc5.mp4>, 2024.
- [62] P. Pongchalee and B.W.J. McNeil. A video of the spike evolution for  $\bar{z} = 800$  and  $4\pi\rho = 10$ . <https://ars.els-cdn.com/content/image/1-s2.0-S2211379724003565-mmc6.mp4>, 2024.
- [63] P. Pongchalee and B.W.J. McNeil. A video of the spike evolution for  $\bar{z} = 9 - 10$  and  $4\pi\rho = 1$ . <https://ars.els-cdn.com/content/image/1-s2.0-S2211379724003565-mmcl.mp4>, 2024.
- [64] Pornthep Pongchalee and Brian McNeil. Unaveraged simulation of a regenerative amplifier free electron laser. In *39th Free Electron Laser Conference (FEL'19), Hamburg, Germany, 26-30 August 2019*, pages 106–109. JACOW Publishing, 2019.
- [65] Pornthep Pongchalee and BWJ McNeil. Sub-wavelength effects in a free electron laser oscillator. *Optics Express*, 31(16):26673–26684, 2023.
- [66] D. Ratner, J. P. Cryan, T. J. Lane, S. Li, and G. Stupakov. Pump-probe ghost imaging with sase fels. *Phys. Rev. X*, 9:011045, Mar 2019.
- [67] S. Reiche. Genesis 1.3: a fully 3d time-dependent fel simulation code. *Nuclear Instruments and Methods in Physics Research Section A: Accelerators, Spectrometers, Detectors and Associated Equipment*, 429(1):243–248, 1999.
- [68] Arthur L Robinson. History of synchrotron radiation. *Synchrotron Radiation News*, 28(4):4–9, 2015.
- [69] Bahaa EA Saleh and Malvin Carl Teich. *Fundamentals of photonics*. John Wiley & sons, 2019.
- [70] E.T. Scharlemann. Wiggle plane focusing in linear wigglers. *Journal of Applied Physics*, 58(6):2154–2161, 1985.

## Bibliography

- [71] M Marvin Seibert, Tomas Ekeberg, Filipe RNC Maia, Martin Svenda, Jakob Andreasson, Olof Jönsson, Duško Odić, Bianca Iwan, Andrea Rocker, Daniel Westphal, et al. Single mimivirus particles intercepted and imaged with an x-ray laser. *Nature*, 470(7332):78–81, 2011.
- [72] Madison Singleton, James Rosenzweig, Jingyi Tang, and Zhirong Huang. An ultra-compact x-ray regenerative amplifier free-electron laser. *Instruments*, 8(1), 2024.
- [73] Y. Socol, A. Gover, A. Eliran, M. Volshonok, Y. Pinhasi, B. Kapilevich, A. Yahalom, Y. Lurie, M. Kanter, M. Einat, and B. Litvak. Coherence limits and chirp control in long pulse free electron laser oscillator. *Phys. Rev. ST Accel. Beams*, 8:080701, Aug 2005.
- [74] Hitoshi Tanaka. The spring-8 angstrom compact free electron laser (sacra). *Proceedings of IPAC2012, New Orleans, Louisiana, USA*, pages 2006–2010, 2012.
- [75] Gijs Van Der Schot, Martin Svenda, Filipe RNC Maia, Max Hantke, Daniel P DePonte, M Marvin Seibert, Andrew Aquila, Joachim Schulz, Richard Kirian, Mengning Liang, et al. Imaging single cells in a beam of live cyanobacteria with an x-ray laser. *Nature communications*, 6(1):5704, 2015.
- [76] Petrus JM van der Slot and K-J Boller. Recent updates to the optical propagation code opc. In *Proceedings of FEL*, 2014.
- [77] Hans Weise, Winfried Decking, et al. Commissioning and first lasing of the european xfel. *Proc. FEL'17*, pages 9–13, 2017.
- [78] Iris D Young, Mohamed Ibrahim, Ruchira Chatterjee, Sheraz Gul, Franklin D Fuller, Sergey Koroidov, Aaron S Brewster, Rosalie Tran, Roberto Alonso-Mori, Thomas Kroll, et al. Structure of photosystem ii and substrate binding at room temperature. *Nature*, 540(7633):453–457, 2016.
- [79] L. H. Yu et al. High-gain harmonic-generation free-electron laser. *Science*, 289(5481):932–934, 2000.

## Bibliography

- [80] Heishun Zen, Ryoichi Hajima, and Hideaki Ohgaki. Full characterization of super-radiant pulses generated from a free-electron laser oscillator. *Scientific Reports*, 13(1):6350, 2023.
- [81] Heishun Zen, Hideaki Ohgaki, and Ryoichi Hajima. High-extraction-efficiency operation of a midinfrared free electron laser enabled by dynamic cavity desynchronization. *Phys. Rev. Accel. Beams*, 23:070701, Jul 2020.